UNIVERSITY OF BERGEN

MASTER THESIS

Fundamental aspects of water methane separation in zeolites

Author:
Kim Nes LEIRVIK

Supervisors:
Bjørn KVAMME
Tatiana KUZNETSOVA

A thesis submitted in fulfilment of the requirements
for the degree of Master of Science

in

Process Technology
Department of Physics and Technology

June 2013

“The more I learn, the more I learn how little I know”

Socrates

Abstract

The main objective of this thesis was to use molecular dynamics to investigate the methane interactions with zeolite, specifically the Linde Type A-3A, alongside with an investigation into the use of polynomial path integration for water in zeolite. This thesis is a part of a larger collaboration between the separation group at the University of Bergen and Statoil, with the main goal of explaining the reduced lifetime of zeolites.

This thesis continued from the work done by the separation group at the University of Bergen. The then used model was suspect to wrongly describe the methane zeolite interactions. Consequently, a new model was tried in order to correctly describe the interactions. The obtained diffusion coefficients for the old and new model, have been compared to reported literature values for a counter-ion free zeolite A. The new model shows an excellent agreement with these values, for a loading of 8 molecules/cavity or more. A simulation using the new model in Linde Type A-3A zeolite, shows that potassium blocks all methane motion in the structure. Furthermore, it was observed that potassium motion, at 500 K under the influence of methane, can lead to unblocking of the 8T-window. This leads us to formulate a hypothesis for the reduced lifetime of LTA-3A zeolite.

Polynomial path integration was performed for water in zeolite. This was computational difficult, due to the different forces in the multi-specie system. The results revealed that different paths from ideal gas towards real gas gave large differences in the estimated excess Helmholtz energy. Other methods can thus be better suited for this purpose, for example the particle insertion method.

Acknowledgements

First and foremost I offer my sincerest gratitude to my supervisors, Professor Bjørn Kvamme and Professor Tatiana Kuznetsova, who have guided me through this master degree. Professor Bjørn Kvamme has with his great knowledge of the field given me tasks and projects that have gradually matured my knowledge in order to complete this thesis. The way he always found time to answer my questions in an occupied time schedule is truly amazing. Professor Tatiana Kuznetsova has with her passion for the field been an inspiration throughout this thesis. She has guided me through many problems that I today can look back at as simple. I am also out most thankful for the guidance that Bjørnar Jensen have given me throughout this work. In spite of writing a doctoral thesis and working on several different projects, he always found time to help me. Without the many advices, and computational tips and trick from Professor Bjørn Kvamme, Professor Tatiana Kuznetsova and Bjørnar Jensen this thesis would never have been completed.

I also would like to thank my fellow students for some well appreciated breaks, vine tastings and discussions. Furthermore, I will like to thank the students at room 363 for sharing there refrigerator and couch with a less privileged student.

Last but not least, I would like to thank my parents for their understanding, moral support and a warm childhood home to come back to. I also will like to thank my brother and sister, with family, for giving me some well needed breaks. A special thank goes to my girlfriend who, beyond my understanding, has kept up with me through these last intensive months.

Contents

List of Figures

List of Tables

Abbreviations

CBU	**C**omposite **B**uilding **U**nit
LNG	**L**iquefied **N**atural **Gas**
LTA	**L**inde **T**ype **A**
NG	**N**atural **G**as
MC	**M**onte **C**arlo
MFC	**M**ixed-**F**luid **C**ascade
MD	**M**olecular **D**ynamics
MSD	**M**ean **S**quare **D**isplacement
OPLS	**O**ptimize **P**otentials for **L**iquid **S**imulations
PBC	**P**eriodic **B**oundary **C**ondition
PBU	**P**rimary **B**uilding **U**nit
PCHIP	**P**iecewise **C**ubic **H**ermite **I**nterpolating **P**olynomial
RMSD	**R**oot **M**ean **S**quare **D**isplacement
RDF	**R**adial **D**istribution **F**unction
SBU	**S**econdary **B**uilding **U**nit
TEG	**Tri****E**thylene **G**lycol
VMD	**V**isual **M**olecular **D**ynamics

Chapter 1

Introduction

This chapter briefly gives the background for this master thesis, the scientific method and the objectives.

1.1 Background

The world is in a constant energy demand, a demand which until better solutions are discovered, is largely covered by fossil fuel. Fossil fuel is a non-renewable energy source which means that the energy sources, as they are spent, are moving farther away from the consumer into new and challenging climates. One important fossil fuel is natural gas, primarily consisting of methane with impurities depending on the properties of the reservoir. Norway is a large producer of natural gas from the natural gas reservoirs on the continental shelf. The natural gas from the fields in the North Sea and Norwegian Sea is compressed at terminals and sent to the continent through different pipelines. The fields in the Barents Sea are located outside this network and the gas is transported by boat. To do the transport in an efficient and environmental friendly way, the natural gas is liquefied to LNG reducing the volume 600 times. This process takes place at the LNG terminal located at Melkøya outside Hammerfest. Water removal is crucial in the production of LNG in order to prevent hydrate or ice from clogging the equipment. The dehydration at Melkøya uses adsorption with zeolites to process the gas from the Snøhvit field and two other fields. The zeolite pellets are designed to have a lifetime of ~ 5 years, but under operating conditions the pellets have to be replaced every 2-3 years. This is costly due to process down time. Analysis of the adsorbent indicate high amount of liquid and thermally degraded triethylene glycol(TEG)[1].

A collaboration between the group for thermodynamic modeling (THEMOD) at the University of Bergen and Statoil, the operator of the plant, has been established. The joint effort aims on investigating the reduced lifetime of zeolites. The THEMOD group, lead by Professor Bjørn Kvamme, is dedicated the task of providing the microscopic insight that can shed light on the macroscopic observation. Results from a preliminary part of this ongoing work have been presented at InMoTher 2012[1, 2], and at the EIGHTEENTH SYMPOSIUM ON THERMOPHYSICAL PROPERTIES. Some of the results indicate that the methane model does not give the true picture of the methane zeolite interaction, in contrast the water model performs well. A Ph.D study on TEG and zeolites is also in progress.

1.2 Scientific method

Of well-established theoretical methods suitable for addressing the nano-scale behavior of these zeolite systems molecular dynamics (MD) and Monte Carlo (MC) are the only ones based on atomistic interactions, which is a necessity for understanding how the different basic elements of the zeolite structure contributes in the separation. The scientific method used in the work mention above is molecular dynamics, a method well suited to obtain knowledge into how a microscopic system evolves through time. This evolution is connected to thermodynamics and the macroscopic observations through statistical mechanics. Monte Carlo techniques have been applied frequently to similar systems, but is not designed for process kinetics. The essence of Monte Carlo is random sampling. Thus, important configuration for the microscopic understanding can be missed. The pure size of the system rules out Ab initio methods, but it can be used to characterize individual species in the system. Molecular dynamics have the advantage of giving both dynamics properties and observable averages at the same time, it is thus well suited for this thesis. Furthermore it also gives the possible to continue on the work done by Jensen et al. [1, 2].

1.3 Objectives

The main objective of this thesis is to investigate the methane interactions with zeolite, specifically the Linde Type A-3Å, alongside with an investigation into the use of polynomial path integration for water in zeolite.

Chapter 2

Natural gas processing

This chapter gives a short introduction into natural gas processing, emphasizing the technology used at Snøhvit while other possible technologies are discussed briefly. The discussion is superficial with the goal of giving a process overview, before moving into zeolites in the next chapter

2.1 Snøhvit

Snøhvit uses a fluid cascade process(MFC)[3] to liquefy natural gas. The dry gas enters the process at pressure and temperature of about 61.5 bar and 284 K, respectively. Two precooling steps separates out the natural gas liquids (NGL), before liquefaction, subcooling and expansion results in the final LNG product. The LNG product keeps a temperature of ∼110 K and a pressure of ∼55.1 bar[4]. Upstream there are several processes taking place to ensure that LNG can be produced and shipped to the marked. Offshore the natural gas is injected with a hydrate inhibitor, for this process monoethylene glycol(MEG)[3]. The gas is then received by an onshore slug catcher before it is flashed in an inlet separator to remove condensate. The MEG is recovered from these two steps and sent back offshore for re-injection. The toxic mercury is removed before the sour gases, carbon dioxide and hydrogen sulfide, are removed to prevent corrosion in equipment, meet health and environmental requirements and prevent crystallization in the cryogenic step, [5, Chapter 7]. The CO_2 is subsequently stored beneath the reservoir to prevent global warming. The last step before the natural gas moves into the MFC process is to reduce the water content to a concentration where ice and hydrate formation do not represent a problem in the following treatment and transport. Typically the water content in the natural gas pre-liquefaction needs to be $\sim$ 0.5 ppmv[6]. To achieve this the dehydration process at Snøhvit use adsorption in a column packed with the potassium form of zeolite A.

2.2 Natural gas dehydration

Natural gas dehydration by adsorption is generally an expensive process applied when a high purity product is required, for example production of LNG. Adsorption using zeolites can achieve water contents down to $\sim$ 0.03 ppmv. The adsorption can also be performed using activated alumina or silica gel. Activated alumina can reach water contents of $\sim$1ppmv, but is more difficult to regenerate. Silica gel can be regenerated but is less effective with a water content in the dry gas of $\sim$10ppmv. The most used dehydration method in the industry is absorption using different glycols, usually triethylene glycol (TEG). The absorption method is cheaper than using adsorption, and usually used when pipeline transportation is possible. With a high solvent circulation, absorption can achieve water contents down to $\sim$ 20 ppmv. Using a Drizo process or injecting dry gas into the glycol reboiler will further improve the solvent purity, leading to more efficient dehydration. Nevertheless, using a glycol solution of 99.97% purity will result in a dewpoint around 200K, which is still too high for LNG production [5, Chapter 7]. Another drawback with absorption is the freezing point of TEG, in its pure form, at 266 K[7]. Continued circulation is then needed to prevent clogging when operating in cold climates.

2.3 Gas adsorption

The adsorption process is performed with two fixed beds packed with the adsorbent, see Figure 2.1. One bed is responsible for dehydrating the wet gas, while the other is regenerating. Wet gas enters the operating column on top to prevent fluidization of the bed. After a given time interval, governed by the break through time, the adsorbent approaches saturation. The wet gas is then switched towards the regenerated bed. Under the regeneration process the bed is purged with hot inert or purified gas. This provides thermal energy for desorption and also transports the adsorbate out of the bed. The purge gas can be reused by flashing or cooling. This process is known as temperature swing adsorption and at Snøhvit conducted at $T_{adsorption}$=∼298 K and $T_{desorption}$=∼503 K using purging with dry gas. Another alternative would be to use pressure swing adsorption, reducing the pressure when regeneration takes place, but this process is not suited when the adsorbate has large affinity for the adsorbent.

The bed is packed with zeolite pellets that usually come in cylindrical or spherical forms with a common diameter of 0.5-0.6 mm, other shapes are also possible. The size and shapes of the pellets are used to reduce the pressure drop over the bed, while the actual zeolite crystal, responsible for the adsorption, is only 1-5 μm [8].

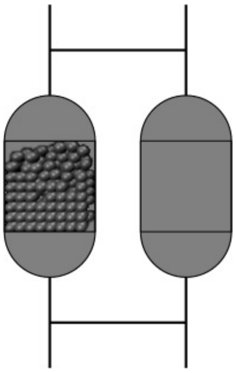

FIGURE 2.1: Two adsorbers, one used for dehydration while the other is regenerated. The columns are filled with spherical zeolite pellets.

2.4 Zeolite pellet

The zeolite pellet consists of a binder material that holds the zeolite crystals. The materials used in the zeolite binder reported by Sircar and Myers [8] is clay, alumina or polymers. Other materials are also used and this is often a well-kept secret of the producer. The binder should be optimized for the specific process. I.e. the adsorption of molecules in the binder should be weak compared to the zeolite crystal. If this is not done the binder can retain some of the components, leading to reduced capacity. For example the use of alumina in the binder could trap heavy hydrocarbons[5, Chapter 7].

Large meso- and macropores are often produced in the zeolite pellet by including organic substances that is combusted in the baking of the pellet. The purpose of these large pores is to improve the transport of adsorbate to the zeolite crystals. An illustration of a zeolite pellet is shown in Figure 2.2 [8].

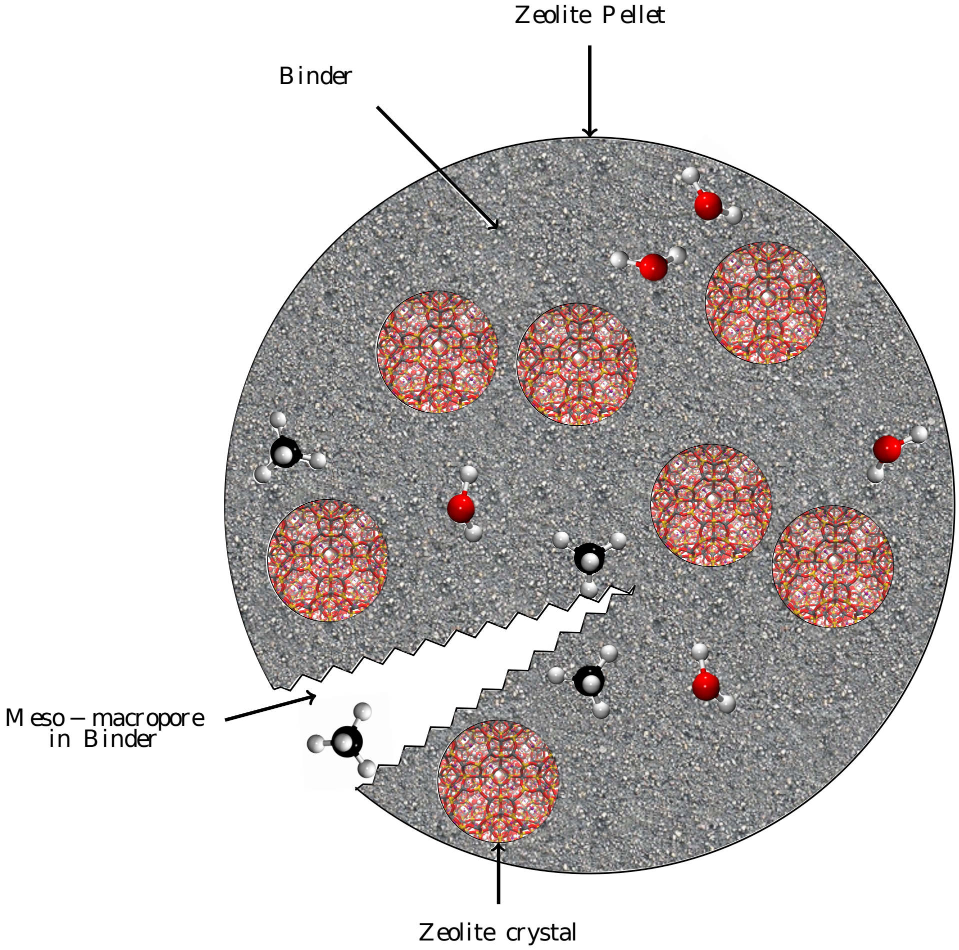

Figure 2.2: Illustration of a zeolite pellet, scales are out of proportions and some molecules are also included. By zooming into the zeolite crystal the water molecules trapped in a zeolite KA crystal can be observed.

Chapter 3

Zeolites

An introduction to zeolites follows below, underlining the zeolite A form.

3.1 History

Zeolites are natural occurring minerals, first discovered by the Swedish mineralogist A.F Cronstedt in 1756. The name zeolite is Greek and means boiling stone, from the immense water loss observed when heating zeolites. The practical use of zeolites was first recognized in the early 20th century, earlier the zeolites were mostly used in jewelry. Alongside with the desiccant properties of zeolites, reversible ion-exchange was discovered as an important property to exploit. The industrial use was kicked off when the Union Carbide Corporation discovered how to synthesize zeolites from a low-temperature hydrothermal process. This made it possible to create zeolites of different forms depending on the area of use. The Linde Corporation developed one of the most known zeolites, the synthetic zeolite A[9].

3.2 Structure

Zeolites are microporous crystalline aluminosilicates, consisting of $[\mathrm{Si}O_4]^{-4}$ and $[\mathrm{Al}O_4]^{-5}$ tetrahedra usually written $\mathrm{T}O_4$ (T=Si, Al) [10]. The $\mathrm{T}O_4$'s form the zeolite host structure, that different types of guest molecules can inhabit, that will change the zeolite characteristics. The number of guest molecules are determined by the number of $[\mathrm{Al}O_4]^{-5}$ included in the framework. Due to the substitution of Si^{4+} with Al^{3+}, a residual negative charge is left on the oxygen framework. This is compensated by guest ions balancing the negative charge[9, Chapter 3].

3.2.1 Host

$\mathrm{T}O_4$ tetrahedrons are the primary building unit (PBUs) in the zeolite , forming secondary building units (SBUs) [11]. The SBUs build together then makes up a composite building unit (CBU) [12] and CBUs put together forms a zeolite unit cell. Zeolite A follows the Loewensteins[13] rule with alternating Al-O-Si linkage, unit-cell sides of ≈24.55[14] and chemical formula $M^{n+}_{\frac{96}{n}}Si_{96}Al_{96}O_{384}$, M indicates a counter-ion. One unit-cell is composed of 8 α-cavities [15], see figure 3.1, connected through the 8T-rings. The α-cavity is formed by twelve 4T-rings, eight 6T-rings and six 8T-rings ($[4^{12}6^{8}8^{6}]$), see figure 3.2. The α-cavity has a diameter of 11.4 Å[9, p.36] and is also known as LTA CBU. The cubic arrangement of the α-cavities makes one β-cage($[4^{6}6^{8}]$) in the middle of the α-cavities, connected to the α-cavity through 6T-rings. The 4T-rings on a β-cage are connected to a 4T-ring of an inverted β-cage. Altogether there are 8 β-cages in one unit-cell [16]. The double 4T-ring(d4r CBU) connecting the β-cages also connects the α-cavities diagonally. The word cage is used when no guest-molecule larger than water can enter, and is based on the largest ring size being a 6T-ring. While cavity is used when larger guest molecules can enter, for a more complete description see [9, 17, 18]. The chemical formula for the host structure in zeolite A gives a residual negative charge of -96 e, which needs to be balanced by counter-ions.

3.2.2 Guest-ions

The mostly used counter-ions in LTA zeolite are potassium, sodium and a mixture of calcium and sodium. The potassium form is known as LTA-3A, the sodium form is known as LTA-4A, and the calcium sodium mixture known as LTA-5A. These zeolites are also known under the names zeolite KA, zeolite NaA and zeolite NaCaA. There are also other forms with magnesium, silver etc. but only the forms mention above is discussed. In a LTA unit-cell there are three main sites preferred by the counter-ions. Site I is at the 6T-ring displaced into the α-cavity, site II is in the middle of the 8T-ring near the plane of the ring, and site III is in the 4T-ring displaced into the α-cavity [19], see Figure 3.2. The size of the counter-ion and the placement at site II will consequently determine the size of the largest open window in the zeolite. The largest window is given by the calcium/sodium exchanged LTA, as indicated by the name ∼5 Å. This is caused by the divalent calcium filling site I before site II, leaving some of the 8T-rings open. The site at the 4T-ring is the least favorable and filled last [20, 21]. For the monovalent cations all the II sites are taken and the sodium form leaves a largest opening of ∼4 Å, while LTA-3A has an opening of ∼3 Å due to the larger potassium ion.

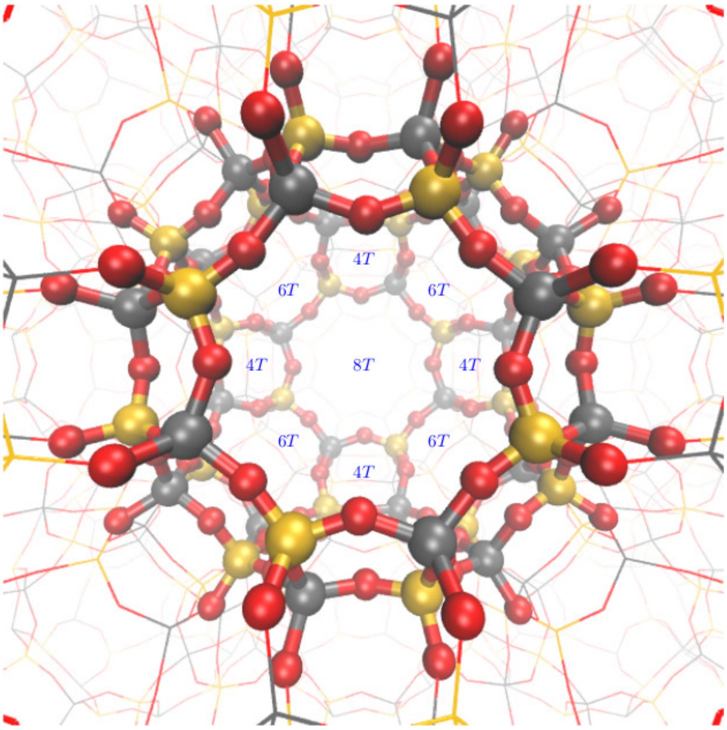

Figure 3.1: α-cavity in zeolite A, with windows marked on the inside and TO_4 linkage sticking out.

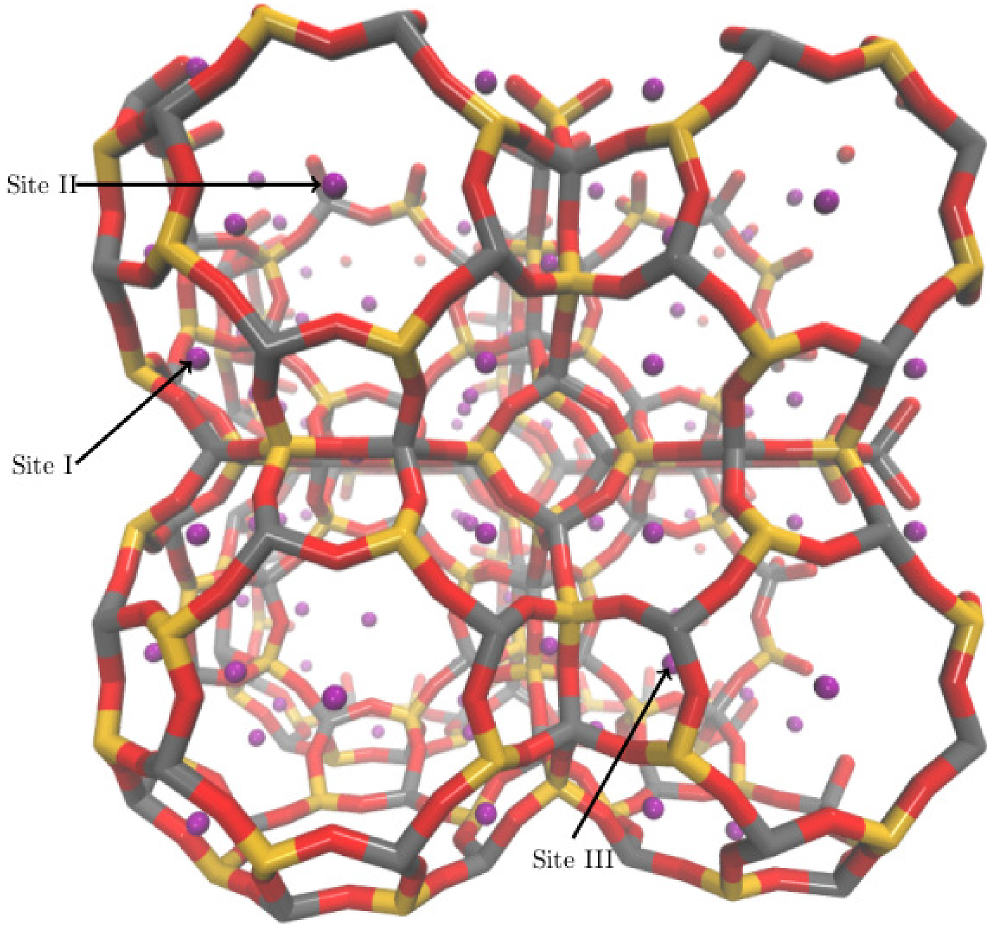

FIGURE 3.2: One unit-cell of LTA-3A zeolite, composed of $K_{96}Si_{96}Al_{96}O_{384}$. The figure is showing 8 α-cavities, 1 β-cage in the middle behind the double 4T-ring. The double 4T-ring is diagonally connecting the α-cavities, while 7 inverted β-cages are partially shown.

3.3 Stability

Zeolites are metastable species, meaning they can exist in less stable states than the most stable state for long periods of time. This can be used to explain why zeolite A does not occur in nature. Some zeolites can be extremely sensitive to heat, and change structure even at room temperature. Zeolites can also be sensitive to critical water loss, which can occur over a large temperature range. This can cause the zeolite to change form, structurally collapse, or recrystallize into a non-zeolite material. The counter-ions in zeolites can easily be exchanged with other ions, because of this ability zeolites are widely used in detergent. The sodium ions in zeolite are then exchanged with calcium ions in water to soften the water. The framework atoms can also be exchanged by exposing the structure to acid or bases containing the wanted ion, for example aluminium hydroxide. This is how the Si:Al ratio is changed in order to facilitate counter-ions.

Zeolite A is stable up to at least 973 K, but readily dissolves in acids as the amorphous aluminium reacts. This increases the Si:Al ratio and the counter ions escapes the structure. In contact with, even a dilute, alkaline solutions zeolite A can transform and if the exposure lasts for months it can dissolve[9, Chapter 8].

3.4 Production

Zeolite A is usually produced by first creating the zeolite NaA. This can be done from mixing sodium hydroxide with different silicate minerals containing aluminium, for example kaolinites[22]. Another option is to use sodium silicate, aluminium trihydrate and sodium hydroxide. This forms a gel which is crystallized and filtered, followed by exchanging the sodium ions with the wanted ions need to produce a given zeolite characteristic. When the wanted zeolite crystals are formed they are bound together using a binder material.

The other forms of zeolite A are formed from the zeolite NaA, thus they can often contain traces of sodium. As stated by Dyer [9] the zeolite KA is often a partially exchanged NaKA zeolite.

3.5 Physical principles of the method

Zeolites are called molecular sieves because of the size or steric exclusion of some molecules, referred to as mode I. Small molecules will see the whole volume of the zeolite pellet, while larger molecules is restricted to a moving through the binder. In practice most gas separation is performed using thermodynamic selectivity. This is the difference in attraction two molecules feels towards the zeolite structure, referred to as mode II. As an example, equally sized polar and non-polar molecules entering the zeolite structure, will lead to the polar molecules interacting strongly with the high charge densities found at the cationic sites, while the non-polar molecules are not hindered by the electric field. The adsorption to the zeolite framework is weak in comparison to the cationic sites because of lower charge density. The thermodynamic selectivity is governed by the difference between bulk gas state and the adsorbed state, through the thermodynamic strive towards equilibrium. The result of these two modes combined, is a kinetic selectivity given by the individual flux of each component divided by the total flux. This gives dynamic local mole-fractions at every position in the structure.

Dehydration of natural gas performed by LTA-3A is an example of exclusion of the larger methane molecule from the zeolite structure, while the smaller water molecule can enter the pores and adsorb[8, 9]. The LTA-4A zeolite uses both modes, as the methane molecules can enter through the 8T-ring, while water can use both the 8T-ring and the 6T-ring. When the molecules have entered, water feels a strong attraction to the zeolite, while the non-polar methane is less hindered.

Table 3.1: Different modes for gas separation.

I	Size or steric exclusion of a certain component caused by the largest open windows in the zeolite being smaller than the size of the component.
II	Thermodynamic selectivity when all components can enter the zeolite structure, but some components have stronger affinity for adsorption, and hence lower diffusion through the zeolite, until all adsorption sites are taken.

Chapter 4

Thermodynamics and statistical mechanics

This chapter starts with a short introduction to the science of thermodynamics, before it moves into the microscopic world of statistical mechanics used to describe the macroscopic world of thermodynamics.

4.1 Thermodynamics

Thermodynamics is a set of laws concerning everyday observations. If a bottle of cold beverage is given sufficient time in a room it takes the same temperature as the room, which can be observed by a thermometer. Thus, if two systems are in thermal equilibrium, and one of the systems is in thermal equilibrium with a third system, then all three systems are in thermal equilibrium. This is known as the first statement of thermodynamics called the 0^{th} law. While driving a steam engine it is observed that internal energy is converted to heat, and heat converted to work, this is the 1^{st} Law of thermodynamics, stating that energy is conserved. A third observation, the 2^{nd} Law of thermodynamics, is that heat is flows spontaneously from a hot system in thermal contact with a colder system. The 2^{nd} Law puts a constrain on the 1^{st} Law, saying that heat cannot be completely converted to work. The development of thermodynamics was started in the 1700's to explain the steam engines. The modern formulation came with J.W.Gibbs and gives the macroscopic explanation of energy, work and heat. The last law of thermodynamics, the third, gives the definition of absolute temperature at 0 K in a perfect crystal.

4.1.1 Thermodynamic potentials

The 1^{st} Law of thermodynamics gives the change in the internal energy in a system as the sum of the heat and work added or abstracted, see Eq. (4.1).

$$dU = \delta Q + \delta W \tag{4.1}$$

The internal energy is a state variable, meaning independent of the path between two states. Work and heat are path variables, dependent on the path between two states. The work term can include different terms, in this thesis focus is on mechanical and chemical work. The heat term is connected to the 2^{nd} Law of thermodynamics through the definition of entropy.

$$dS = \frac{\delta Q_{rev}}{T} > \frac{\delta Q_{irrev}}{T} \tag{4.2}$$

In Eq. (4.2) the terms reversible and irreversible appear. The reversible change is one that always stays in equilibrium with the surroundings. This means it follows a path of infinitesimal small changes between an initial state and a final state. An irreversible change is a spontaneous change where the system feels the influence of the surroundings instantaneously. A good example is a gas in a cylinder held under a piston with a weight on top. The system is in equilibrium at the initial state, if the whole weight is removed the gas instantaneously feels the external pressure and a spontaneous process takes place. In contrast, if one decreases the mass of the weight with an infinitesimal small change of mass over an infinite time, the system will always stay in equilibrium with the surroundings and the change is reversible. This means that one can also add an infinitesimal small mass and recover the old state. The reversible change serves as a reference state for a real spontaneous process.

The energy of the universe is constant. So if the definition of entropy is applied, it follows that the change in entropy always is larger than zero, and equal to zero in equilibrium. This is the 2^{nd} Law of thermodynamics, Eq. (4.3).

$$dS \geq 0 \tag{4.3}$$

Starting from the 1^{st} Law of thermodynamics, for a reversible change and a one component system, the internal energy is given as a function of the extensive variables entropy(S), volume(V) and number of particles(N), meaning we have a function U(S,V,N) given in Eq. (4.4). From Gibb's phase rule for extensive variables one also knows that only c+2 variables can be determined, with c equal to the number of components in the system, there is only one component in Eq. (4.4). An extensive variable is one that depends on the size of the system, in contrast to an intensive variable which is independent of the size of the system.

$$dU = \underbrace{T}_{\frac{\partial U}{\partial S}} dS \underbrace{-P}_{\frac{\partial U}{\partial V}} dV \underbrace{+\mu}_{\frac{\partial U}{\partial N}} dN \tag{4.4}$$

The 1^{st} Law give information on the internal energy of the system, but will not directly give information on the work possible to extract. From the 2^{nd} Law, Eq. (4.3), it is known that a spontaneous process will maximize its entropy and minimize its energy until equilibrium. Just as a ball falling to the ground minimizes it is energy, while giving of heat and increasing the entropy. It would therefore be favorable with a function that contains the same information as the 1^{st} Law, but in terms of other variables. Rearranging the 1^{st} Law gives S(U,V,N), see Eq. (4.5).

$$dS = \frac{1}{T}dU + \frac{P}{T}dV - \frac{\mu}{T}dN \tag{4.5}$$

The disadvantage with entropy, as a thermodynamic potential, is that it lacks practical applications, since few natural systems are held under constant energy. Nonetheless, it makes a good foundation for statistical mechanics, as entropy is the natural potential to the microcanonical ensemble. The microcanonical ensemble will be discussed more in subsection 4.2, furthermore it is also the natural ensemble in a molecular dynamic simulation[23, p. 454], to be discussed in Chapter 5.

Temperature is a variable that is easy to observe, furthermore many real processes occur under constant temperature (or at least close to constant). So expressing the 1^{st} Law in terms of temperature instead of entropy will through a Legendre transformation[24, p. 87-89] give the familiar Helmholtz-potential, or Helmholtz free energy.

$$A(N,V,T) = U(V,N,S(T)) - \frac{\partial U}{\partial S}S = U - TS$$

with the differential:

$$dA = d(U - TS) = \underbrace{-S}_{\frac{\partial A}{\partial T}} dT \underbrace{-P}_{\frac{\partial A}{\partial V}} dV \underbrace{+\mu}_{\frac{\partial A}{\partial N}} dN \tag{4.6}$$

From Eq. (4.6) one can see that the Helmholtz free energy is the energy potential minus the irreversible losses due to entropy generation. Thus, it represents the available energy in the system. The Helmholtz potential contains the same information as entropy, but more easily accessed. In similar ways one can continue deriving other potentials depending on the available variables. Legendre transformation of the Helmholtz-potential from V→P gives Gibb's free energy, G, and Legendre transformation of Helmholtz-potential from N→ μ gives the grand potential, ϕ. Knowing the potential makes it possible to calculate all equations of state from the partial derivative of the potential. As an example, pressure is the negative partial derivative of Helmholtz energy with regards to volume, which is shown in Eq. (4.6).

4.1.2 Equilibrium

A system moves towards equilibrium through maximizing entropy and correspondingly then minimizing energy. Hence the direction towards equilibrium is in the minimum of the free energy where the change in the potential is zero. In an isolated equilibrated system with two phases and one component the following case is true:

$$U^1 + U^2 = U_{tot} = constant \qquad S^1 + S^2 = S_{max} = constant$$

$$V^1 + V^2 = V_{tot} = constant \qquad N^1 + N^2 = N_{tot} = constant$$

Thus using Eq. (4.4)

$$d\left(U^1 + U^2\right) = \left(T^1 - T^2\right) dS^1 + \left(P^1 - P^2\right) dV^1 + \left(\mu^1 - \mu^2\right) dN^1 = 0$$

Because there are no constraints on each phase, only on the total system. It follows that the above can only be true when Eq. (4.7) is true, where c components, j=1,...,c, have been included. For a real system the pressure is replaced with the fugacity.

$$T^1 = T^2 = ... = T^p \qquad P^1 = P^2 = ... = P^p \qquad \mu_j^1 = \mu_j^2 = ... = \mu_j^p \tag{4.7}$$

In equilibrium it follows from Gibb's phase rule for intensive variables, that c+2-p intensive variables determines the system. When the system is not in equilibrium knowledge of the intensive properties of each phase shows the direction towards equilibrium[24, Chapter 2-3].

4.2 Statistical mechanics

The laws of thermodynamics are macroscopic laws and changes to thermodynamic variables can be measured by different methods. The origin of the macroscopically observable property changes, in thermodynamics, is related to a microscopic world of small particles. These particles are in this thesis limited to atoms building up molecules. The description of the microscopic world is given by statistical mechanics, without this description thermodynamics would only be a phenomenological theory. It was Ludwig Boltzmann and J. Willard Gibb's that established the foundation for classical statistical mechanics in the late 19th century, they used classical mechanics to describe the motion of particles. In light of the quantum mechanics developed in the early 20th century, the classical description of particles can only be considered an approximation when the particles are not competing to get into the same energy states. In this case the quantum statistics, Fermi-Dirac and Bose-Einstein distributions, can be approximated by the Boltzmann distribution from classical statistical mechanics [24, p.311].

Classical statistical mechanics are, as the name suggests, based on the formulations given by Sir Isaac Newton. Newton's Law says that the force F exerted by the object is equal to the acceleration of the object multiplied by the mass of the object, this can also be given by the time derivative of momentum. The use of momentum is practical when moving into phase space as energy is specified by the particles positions and momentums. An important characteristic of a classical system is that the space related to momentums (translational, rotational, intramolecular) is orthonormal to the volumetric space representing the interactions between atoms and molecules as function or relative positions.

The total energy of a microscopic system is written as the sum of kinetic and potential energy. It is practical to define the Hamiltonian as this sum Eq. (4.8), and use momentum and position as variables. One has to consider all the particles, so the sum in Eq. (4.8) runs over N particles, with the momentum vector $\boldsymbol{p}$ given by $\boldsymbol{p}_x, \boldsymbol{p}_y, \boldsymbol{p}_z$ and position vector $\boldsymbol{r}$ given by position q_x, q_y, q_z so a total of 6N variables are needed to determine the energy of the system. In Eq. (4.8) $\boldsymbol{r} \equiv \boldsymbol{r}_1, .., \boldsymbol{r}_N$ and $\boldsymbol{p} \equiv \boldsymbol{p}_1, .., \boldsymbol{p}_N$.

$$\mathscr{H}(\boldsymbol{p}, \boldsymbol{r}, t) = K + U = \sum_{i=1}^{N} \frac{\boldsymbol{p}_i^2(t)}{2m_i} + U(\boldsymbol{r}, t) \tag{4.8}$$

The equation of motion follows from the Hamiltonian as 6N first order ODE's

$$\begin{aligned} \dot{\boldsymbol{r}}_i &= \frac{\partial \mathscr{H}(\boldsymbol{p}, \boldsymbol{r}, t)}{\partial \boldsymbol{p_i}} = \frac{\boldsymbol{p_i(t)}}{m_i} \\ \dot{\boldsymbol{p}}_i &= -\frac{\partial \mathscr{H}(\boldsymbol{p}, \boldsymbol{r}, t)}{\partial \boldsymbol{r_i}} = -\frac{\partial U(\boldsymbol{r}, t)}{\partial \boldsymbol{r_i}} = \boldsymbol{F}_i \end{aligned} \tag{4.9}$$

The time derivative of the first line in Eq. (4.9) substituted in the second line recovers Newton's 2^{nd} Law. The second line in Eq. (4.9) follows from the forces being conservative and derivable from the gradient of a scalar potential energy function, see Eq. (4.10).

$$\boldsymbol{F}_i(\boldsymbol{r}, t) = -\nabla_i U(\boldsymbol{r}, t) \tag{4.10}$$

The energy space is a 6N dimensional space given by momentum and position. This space is known as phase space and each point in phase space is known as one energy state or microstate. If the system is not in equilibrium phase pace will also be time dependent. With 6N variables that can be time dependent, and often consisting of particle numbers in the range of 10^{23}, it would seem to be an impossible task to find an analytical solution to this problem. The statistical mechanic solution is to apply the ensemble theory, another solution is given by obtaining a numerical solution to a smaller, but representative part of the system. The last solution is the way of molecular dynamics, to be discussed in detail in Chapter 5.

4.2.1 Ensemble theory and ergodicity

Ensemble theory is based on the concept that a thermodynamic observed value is the average of the microscopic properties of the system. In the case of a given thermodynamic potential one can construct an ensemble of identical macroscopic systems, see Figure 4.1, described by different microscopic variables. The average of the ensemble is then connected to the time average through the ergodic hypothesis. It has not been possible to prove the ergodicity of a system but it is possible through the Liouville theorem and the Liouville equation. The Liouville theorem shows that a phase space volume at t=0 will be conserved at t=t, which is shown illustratively in Figure 4.2. The Liouville equation shows that the phase space distribution is conserved along a path in phase space. Thus, $f(\Gamma_0)d\Gamma_0=f(\Gamma_t)d\Gamma_t$ with $f(\Gamma_0)$ being the distribution function, see Eq. (4.24), and $d\Gamma$ a phase space element. In an equilibrium system the observables are static, the time dependence in the Hamiltonian is removed leading to $\frac{\partial f}{\partial t} = 0$. The ensemble average can then be performed at any point in time[25, Chapter 2.4].

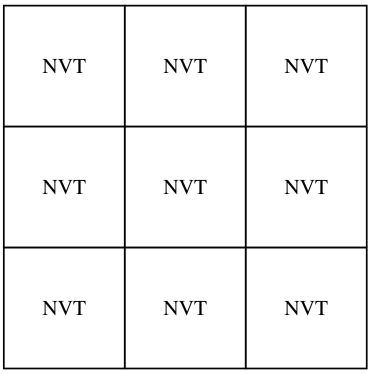

Figure 4.1: Canonical ensemble, each subsystem is described by its own arrangement of microscopic variables corresponding to the same observed macroscopic variables

A Hamiltonian independent of time, $\mathscr{H}(\boldsymbol{p}, \boldsymbol{r})$, following an ergodic trajectory will sample all microstates in the ensemble when time goes to infinity, see Eq. (4.11). For a large system this integral cannot be solved, thus the best solution is a numerical approach. This is done in molecular dynamics, representing a method to obtain both ensemble averages and dynamic properties, see Chapter 5. Furthermore, it is not necessary for the Hamiltonian to be independent of time. This is the way of non-equilibrium molecular dynamics, but this is beyond the scope of this thesis[25, Chapter 13]. All simulations have been done using equilibrium molecular dynamics.

$$\langle A\rangle_{time} = \frac{1}{t}\int_0^t dt A\left(\boldsymbol{p}(t)\boldsymbol{r}(t)\right)$$

$$\langle A \rangle_{ensemble} = \lim_{t \to \infty} \langle A \rangle_{time} \tag{4.11}$$

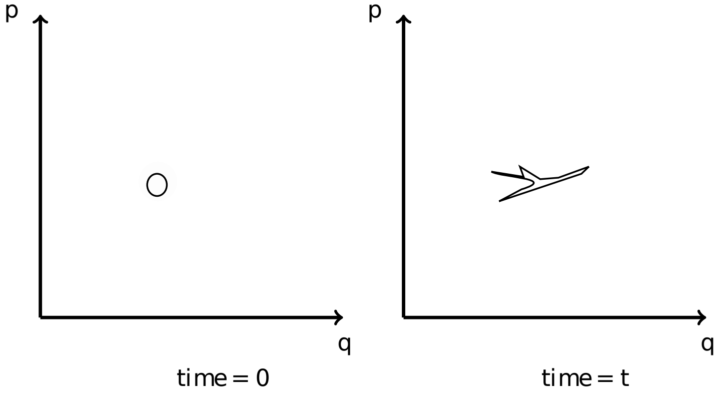

FIGURE 4.2: Luiville's theorem, the volume element at t=0 can spread out in phase space but has to contract in other dimensions to preserve the volume. The right hand side phase space volume is distorted due to the chaotic nature of a dynamical system.

4.2.2 Macroscopic microscopic connection

Ludwig Boltzmann made a postulate that in an equilibrium ensemble of constant E,V,N, known as a microcanonical ensemble, entropy is proportional to the logarithm of the total number of microstates, Ω, in the system. This is the basic connection between the macroscopic and microscopic world. The proportionality constant is known as Boltzmann's constant, and Ω is the microcanonical partition function, see Eq. (4.12).

$$S\left(E,V,N\right) = k_b ln\left(\Omega\left(E,V,N\right)\right) \tag{4.12}$$

The connection between the microscopic and macroscopic world gives a fundamental insight into the concept of heat and work. The microcanonical partition function is derived by putting one constrain on the ensemble. This is the constrain that the number of systems in phase space must sum up to the number of system in the ensemble, which is the same as saying that the probability must sum up to one. The canonical ensemble is a constrained microcanonical ensemble, where the average energy must be the sum of the weighted energy of all microstates, see Eq. (4.13). $\mathcal{N}$ is the number of systems in the ensemble, n_i is the number of systems in one microstate, the sum runs over all microstates and E_i is the energy in microstate i.

$$U = \langle E \rangle = \sum_i \underbrace{\frac{n_i}{\mathcal{N}}}_{p_i} E_i \tag{4.13}$$

Eq. (4.13) shows the basic idea of statistical mechanics. The most probable distribution of systems over phase space is found by maximizing the distribution function while applying the constrains through Lagrange multipliers. This gives the phase space density, and the denominator, the total number of microstates, is known as the partition function which can be connected to the potential corresponding to the given ensemble, see Table 4.1. Eq. (4.13) can be compared to Eq. (4.4) to give a microscopic understanding of heat and work, taking the differential of Eq. (4.13) gives.

$$dU = \underbrace{\sum_i E_i dp_i}_{\delta Q} + \underbrace{\sum_i p_i dE_i}_{\delta W}$$

This shows that that adding or removing heat changes the probability of finding a system within a given energy level, meaning that the distribution of systems over phase space changes while the energy levels stays constant. Work can then be seen as an ordered change where the distribution of systems over phase space stays constant, but the energy levels changes[26].

As mentioned in the thermodynamic part, Chapter 4.1, all the thermodynamic potentials contains the same information, thus it is possible to move from entropy to another potential. Another connection comes through the Laplace transformation of the partition functions [24, p.189-194]. For example the Laplace transformation of the microcanonical partition function gives the canonical partition function. It can then be shown that in the thermodynamic limit of $N \to \infty$ the observed values in one ensemble is the most probable in another ensemble. This is an advantage because the microcanonical partition function needs the solution of an N-dimensional sphere, in the other potentials the dimensions can be factorized, leading to a simpler solution. The partition functions are connected to the potential describing the ensemble, this connection is summarized in Table

4.1. The microcanonical ensemble serves as the foundation for the other ensembles, the canonical ensemble is the weighted ensemble of numerous microcanonical ensembles with different energies, corresponding to the same temperature. The grand canonical ensemble is again the weighted ensemble of many different canonical ensembles with different particle numbers, but same chemical potential. The open system, grand canonical potential, depends on a single extensive variable, V, in combination with the Euler relation it directly leads to the equation of state $\phi = -PV$. It must be mentioned that this is just a short introduction to thermodynamics and statistical mechanics, more details on the thermodynamic potentials, phase space and the partition functions can be found in any text book on thermodynamic and statistical mechanics, two such books are Greiner et al. [24] and Tuckerman [25].

TABLE 4.1: The macroscopic microscopic connection for different ensembles.

Potential	Observed variables	Partition function	Connection
S	EVN	Ω	S = $k_b ln\Omega$
A	NVT	Z	A = -$k_b TlnZ$
G	NPT	Δ	G = -$k_b Tln\Delta$
ϕ	μVT	$\mathcal{Z}$	ϕ = -$k_b Tln\mathcal{Z}$

4.3 Energy in a microscopic system

The Hamiltonian in Eq. (4.8) is as mentioned earlier, the sum of the kinetic and potential energy. The average kinetic energy is through statistical mechanics connected to the temperature of the system. To be more specific, the equipartition theorem states that the average kinetic energy will distribute evenly between each degree of freedom in the system. The number of degrees of freedom depends on how the molecules are built up. Monoatomic molecules have only translational degrees of freedom. For di-atomic and larger molecules the degrees of freedom are summarized in Table 4.2. The average of each degree of freedom will through the equipartition theorem have a thermal energy of $\frac{1}{2}\mathrm{k}_b\mathrm{T}$ [27, Chapter 2.5.3].

Table 4.2: Internal degrees of freedom for linear and non-linear molecules, n is the number of atoms in the molecule.

	Linear molecule	non-linear molecule
Translation	3	3
Rotation	2	3
Vibration	3n-5	3n-6

The potential energy can be divided into bonded intramolecular interaction between atoms in molecules, and non-bonded intermolecular interactions. The non-bonded interactions can be simplified by using a united-atom model. This assigns one site to the whole molecule or functional groups in the molecule. This will reduce the internal degrees of freedom, but is faster to calculate. The total potential energy can be written as a sum of all the interaction as done in Eq. (4.14).

$$U = U_{bonded} + U_{non-bonded} \tag{4.14}$$

From Eq. (4.10) it is clear that the ability to describe a real system depends on selecting a potential energy function describing the interactions correctly. There are many different potentials to choose from, and alongside with the ability to describe reality one must consider how easy it computes.

4.3.1 Bonded interactions

The bonded interactions can be divided into bond-stretching, angular-bending and dihedral-twisting. The stretching of a covalent bond is most realistic describe by the Morse potential, consisting of an exponential term and two fitting constants. Another solution is to do a Taylor expansion around the equilibrium bond length, truncating the expansion after the third term and setting the constant to zero. This leads to Hook's law given in Eq. (4.15), and illustrated in Figure 4.3. In Eq. (4.15) K_a is the bonded force constant and r_{eq} is the equilibrium distance between the two atoms.

$$U_b = \frac{1}{2} K_b(\boldsymbol{r} - \boldsymbol{r}_e) \tag{4.15}$$

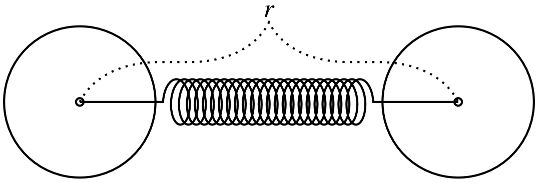

FIGURE 4.3: Harmonic spring to describe the covalent bond between two atoms.

As long as the bond length does not deviate too much from the equilibrium length it is sufficient with the first non-zero term in the Taylor expansion. The Harmonic potential is then usually chosen over the Morse-potential because it is faster to compute[28, p.20].

Hook's law can also be used to model the angular bending between three atoms. A spring is then attached to the covalent bonds two atoms form with a third atom, as illustrated in Figure 4.4.
The energy is then given by Eq. (4.16), where K_a is the angular force constant and θ_{eq} is the equilibrium angle between the two atoms.

$$U_a = \frac{1}{2} K_a(\boldsymbol{\theta} - \boldsymbol{\theta}_e) \tag{4.16}$$

The harmonic potential is used to model the bonded interactions in this Thesis. The functional form of dihedral bending is not mentioned because there are no dihedral angels modelled in this thesis. The zeolite structure is considered to be fixed in space, and only modelled with non-bonded interactions.

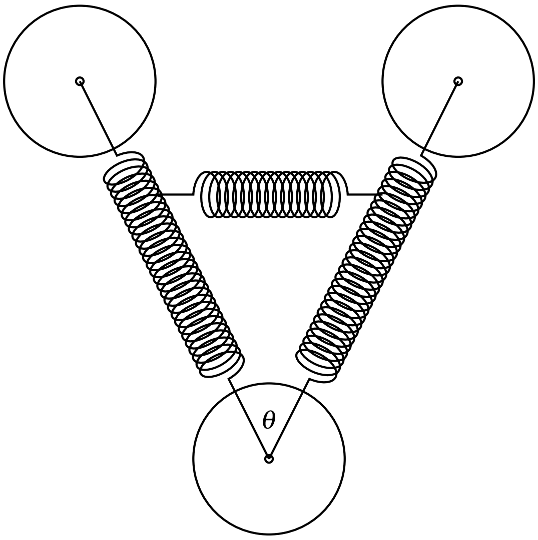

FIGURE 4.4: Angular bending modelled with a harmonic spring.

4.3.2 Non-bonded interactions

The non-bonded interactions are forces between atoms that are not connected by covalent bonds. The type of interactions depends on the species interacting. Figure 4.5 shows repulsion between two atoms with a collision diameter of σ separated by a distance $\boldsymbol{r}_{ij}$. The force $\boldsymbol{F}_{ji}$ is equal in magnitude but opposite in direction to the force $\boldsymbol{F}_{ij}$, from Newton's 3^{rd} law.

A common approximation is to consider only two-body interactions, because of the tremendous task of evaluating the influence of 2,3,4,...,N-1 atoms onto atom $A_{1,2,...,N}$. This can give some error, especially for polar species, so often the average of the third-order terms and higher are incorporated into the two-body interactions by experimental fitting, or including a correction to the calculations. The non-bonded interaction can then be written as a $U_i = \sum_{j\neq i}^{N} U_{ij}$.

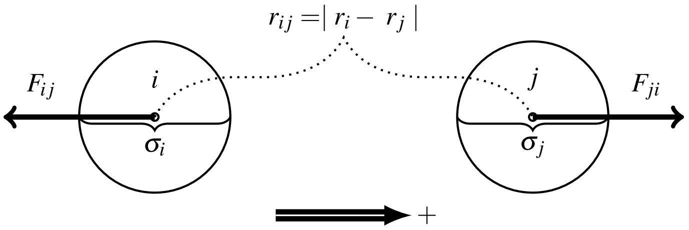

FIGURE 4.5: Intermolecular repulsion between two non-bonded particles separated by a distance $\boldsymbol{r}$.

The non-bonded interactions depend primarily on the distance between the species. At small distances the Pauli repulsion from overlapping electron orbitals will dominate. Its not possible to derive a dependency on the distance for the Pauli repulsion, although it can be justified. The exact wave function for the hydrogen atom is an exponential function, so the electron density will approximately fall off exponentially with distance. As the distance increases, other forces becomes important, of course depending on the properties of the atoms [29, p.23-29].

Interactions between two permanent dipoles gives a temperature dependent ($\pm 1/\boldsymbol{r}^3$) term, which will depend on the orientation of the two molecules. The most probable alignment is found by Boltzmann averaging all energies from the different orientations. The energy distance dependency is then ($-1/\boldsymbol{r}^6$). The dipole-dipole interaction is also known as Keesom force.

Forces from a dipole interacting with a polarizable specie is known as Debye force, and comes from a dipole inducing a dipole in the polarizable specie. The interaction will be attractive, since the polarizability is positive and the average orientation is obtained using the Boltzmann distribution, giving the same distance dependency as the Keesom force.

As electrons moves around they can cause an instantaneous uneven charge distribution around the nucleus. These differences in electron density create an induced dipole, which can induce a dipole in a neighboring specie. The induced dipole - induced dipole interaction is just the leading term in which the energy is approximated to, the quadrupole and multipole terms follow behind. This force is known as London dispersion and together with the Keesom and Debye forces commonly summarized as van der Waals forces which decays proportional to ($1/\boldsymbol{r}^6$).

This is also the basis for the attractive parts of typical efficient pair potentials. As mentioned in the start of the section, in the real world more than the two atoms in consideration will determine the interactions energy. This type of multi-particle dependency will be accounted for in quantum mechanics ab initio modeling. But these types of calculations are extremely computationally demanding and not suitable for realistic scales of systems which may contain everything from a few molecules up to several thousand. In this context it is therefore important to consider the potentials of interactions, Section 4.3.3, as 'efficient' average pair interaction energies which will contain some average contributions from higher order interactions due to surrounding particles. This will of course induce some reduction in applicability to other surroundings than what they were originally derived for this can be resolved by fitting to some experimental data for real systems.

The last force to be considered is the electrostatic force between charges, also called Coulomb force. This can be charges on ions or partial charges on molecules. For ions the charge comes from the quest to achieve octet, meaning filling of outer shell. In this case an atom with high electronegativity steals an electron from an atom with low electronegativity, and the charges appears as integers of e. Partial charges are used to account for an electron spending more time in a specific part of the molecule. This is governed by the difference in electronegativity between the bonded atoms. Charles Coulomb found in the late 18th century that the energy from charge-charge interactions falls off with $(1/\boldsymbol{r})$.

To summarize one can divide the non-bonded potential energy into two parts, energy falling off with $(1/\boldsymbol{r}^6)$ or faster, from short-range forces, and energy falling of slower from electrostatic forces, also called long range forces. In molecular dynamics the temperature of the system and the positions of the molecules follow from the simulation, so both the Keesom and Debye forces will be incorporated into the electrostatic forces since it is not necessary to perform the Boltzmann averaging. The non-bonded energy will then be given by Eq. (4.17).

$$U_{non-bonded} = \underbrace{U_{Pauli\ repulsion} - U_{London\ dispersion}}_{Short-range} + \underbrace{U_{Electrostatic}}_{Long-range} \tag{4.17}$$

The models for the short-range interactions and long-range interaction will now be investigated, but emphasis will be on the short-range interactions.

4.3.3 Models for short-range interactions

The most used potential to model short-range interaction is the Lennard-Jones potential, which was developed in 1924 by Jones [30]. He proposed to model the Van der Waals forces by a repulsive and an attractive part each given by the inverse of the distance raised in some exponent. The parameters are the collision diameter, σ, the well depth, ϵ, and a constant depending on the selected exponents. Because the attractive part depends on the $(1/\boldsymbol{r}^6)$ of distance, the most used form of the Lennard-Jones potential has the exponents 12-6, known as the Lennard-Jones 12-6 potential, see Eq. (4.18). The exponent of the repulsive part is put to twelve because of the simplicity of taking the square of the attractive part. The values of the two exponents give the constant value on the right hand-side in Eq. (4.18), which for the 12-6 LJ gives the constant 4.

$$U_{Short-range} = 4\epsilon \left[\left(\frac{\sigma}{\boldsymbol{r}_{ij}} \right)^{12} - \left(\frac{\sigma}{\boldsymbol{r}_{ij}} \right)^{6} \right] \tag{4.18}$$

The clear weakness of the Lennard-Jones potential is the repulsive part. Hill [31] stated that the Lennard-Jones form is not satisfactory when $U >> 0$. He then proposed that equation 1 in Hill [31] would give a better description for spherical non-polar molecules, the same form was also proposed by Buckingham [32]. The potential is therefore know as Hill or Buckingham potential, see Eq. (4.19). This is the form for the Buckingham potential used in the simulation part of this thesis, see Table 6.1 and Table 6.4.

$$U_{Short-range} = Ae^{-\frac{r_{ij}}{\rho}} - \frac{C}{\boldsymbol{r}_{ij}^{6}} \tag{4.19}$$

The Buckingham potential can also be written in a more informatory way, see Eq. (4.20) [23, p.36].

$$U_{Short-range} = \begin{cases} -\infty & when\ \boldsymbol{r}_{ij} \to 0 \\ \epsilon \left[\dfrac{6}{\alpha - 6} \cdot e^{\alpha\left(1 - \frac{r_{ij}}{r_m}\right)} - \dfrac{\alpha}{\alpha - 6} \left(\dfrac{r_m}{\boldsymbol{r}_{ij}} \right)^{6} \right] & when\ \boldsymbol{r}_{ij} > \lambda r_m \end{cases} \tag{4.20}$$

Where ϵ is the well depth, same as in Eq. (4.18), r_m is the distance where the potential energy takes a minimum at $-\epsilon$. This means that the repulsive and attractive forces are equal. λr_m is the distance where the Buckingham potential takes a non-physical maximum as the repulsive part goes towards a constant value.

The Lennard-Jones potential can also be written in terms of r_m because $r_m = \sqrt[6]{2}\sigma$. This form is often used, as done in equation 2, Hill [31]. The difference in the Lennard-Jones and Buckingham potential can then easily be visualized, see Figure 4.6. Except from difference in the functional form of the Buckingham and Lennard-Jones equations, the only difference is the parameter α controlling the steepness of the Buckingham potential. An α of 12 gives the same attractive force as the Lennard-Jones potential.

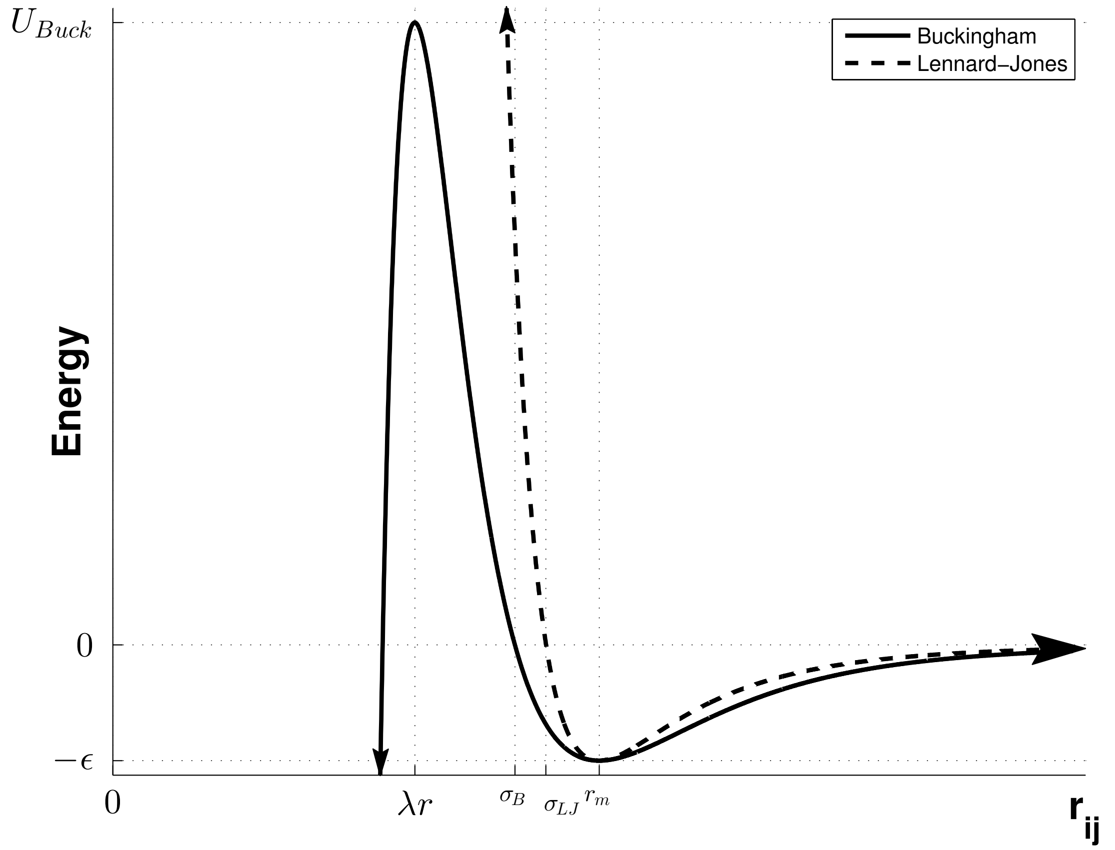

FIGURE 4.6: Plot of Buckingham potential and 12-6 Lennard-Jones potential, with same r_m and same well depth, see Appendix A for script.

As one can see from Figure 4.6 the Buckingham potential gives a softer repulsion at close distances. It has been shown that this is a more true description of the van der Waals forces, compared with the Lennard-Jones potential, Hart and Rappe [33].

The values of the parameters in the non-bonded interactions are usually obtained through empirical fitting to experimental data or fitting to quantum mechanical calculations. A force-field describing the energy of a system will not necessarily correctly describe the diffusion, so care must be taken in the selection process. Usually one considers the force field for pure species, although parameters for mixtures are also used. From the pure force field parameters the interactions between mixtures follows from the combining-rules or mixing-rules. The use of mixing-rules avoids the need to fit a specific set of parameters to all pair types in the simulation.

4.3.4 Mixing-rules

The most frequently used mixing-rule in literature is the Lorentz-Berthelot rule. The well-depth, ϵ_{ij}, of the type-type interaction is taken as the geometric mean, see first line Eq. (4.21), and the collision diameter, σ_{ij}, is obtained as the arithmetic mean, see second lineEq. (4.21).

$$\begin{aligned} \epsilon_{ij} &= \sqrt{\epsilon_{ii}\epsilon_{jj}} \\ \sigma_{ij} &= \frac{\sigma_{ii} + \sigma_{jj}}{2} \end{aligned} \tag{4.21}$$

The Lorentz-Berthelot mixing-rule is widely used because of the simplicity of the expressions. The geometric mean of the well-depth arises from behavior close to critical point. While the arithmetic mean is just the average of the collision distance between the two spheres, the later can only be considered valid for hard-spheres[34]. A number of different mixing-rules have been proposed, which can improve the results for a specific system. Good and Hope [35] proposed use the geometric mean for all parameters in the Lennard-Jones potential, and for the Buckingham potential as well. This is the mixing-rules used for the Buckingham potential in this thesis, summarized in Eq. (4.22). Because of the large amount of available mixing rules one should keep in mind that different mixing-rules can improve the calculations. The main objective must always be to build a model that describes reality in a correct manner.

$$\begin{aligned} A_{ij} &= \sqrt{A_{ii}A_{jj}} \\ \rho_{ij} &= \sqrt{\rho_{ii}\rho_{jj}} \\ C_{ij} &= \sqrt{C_{ii}C_{jj}} \end{aligned} \tag{4.22}$$

4.3.5 Long-range interactions

There are several ways to model the long-range interactions, depending on how the electrostatics is defined. One possibility is to use the electronegativity to determine the charge, thus the electronegativity becomes the parameter describing the interactions. Another alternative is to define a charge polarization for the bonds, and use orientation vectors between two dipoles[23, p.40]. The simplest and most used way is to assign fixed charges and model them using Coulomb's law. The energy from charge-charge interactions is then given by the Coulomb potential Eq. (4.23).

$$U_{Long-range} = \frac{q_i q_j}{4\pi\epsilon_0 \boldsymbol{r}_{ij}} \tag{4.23}$$

Where q_i and q_j are the elementary charges at point i and point j, ϵ_0 is the permittivity of free space, and $\boldsymbol{r}_{ij}$ is the distance between the charges.

4.4 Calculations of observables

Starting in the canonical ensemble the total partition function Z is given in Eq. (4.24).

$$Z\left(N,V,T\right) = \frac{1}{N!h^{3N}} \int e^{-\beta\mathscr{H}(\boldsymbol{p},\boldsymbol{r})} d^N\boldsymbol{p} d^N\boldsymbol{r} \tag{4.24}$$

Where N! is the Gibb's correction factor for identical particles and h^{3N} is the required volume for a quantum mechanical state transferred to classical phase space[24]. The kinetic term in the Hamiltonian contains information of the ideal system, while the potential energy determines the particular properties of a real system. Thus, integrating Eq. (4.24) over all momentum reveals the advantage of the canonical partition function over the microcanonical. The momentum integral is a Gaussian integral where the 3N dimensions factorizes. The solution to this integral gives Eq. (4.25).

$$Z\left(N,V,T\right) = \frac{1}{N!\lambda_t^{3N}} \underbrace{\int e^{-\beta U(\boldsymbol{r}_1,..,\boldsymbol{r}_N)} d^N\boldsymbol{r}}_{\mathsf{z}} \tag{4.25}$$

λ_t is the thermal wave length, which can be used to check if quantum mechanics can be approximated by classical mechanics. This is the case when $\frac{V}{N} >> \lambda_t = \frac{h^2}{2\pi m k_B T}$. When $U(\boldsymbol{r}) = 0$ the integral over positions simply gives the volume of the container and the ideal gas law is recovered. The integral over position can be denoted as the configurational partition function z. The ensemble average of any coordinate-dependent function will then follow. The probability of finding a particle N at a point $\boldsymbol{r}_N$ in a volume element d$\boldsymbol{r}_N$ is thus given by Eq. (4.26).

$$P^N(\boldsymbol{r}_1, .., \boldsymbol{r}_N)\, d^N\boldsymbol{r} = \frac{e^{-\beta U(\boldsymbol{r}_1, .., \boldsymbol{r}_N)}}{\mathsf{Z}} d^N\boldsymbol{r} \tag{4.26}$$

The free energies or thermodynamic potentials are as mentioned earlier state variables and connected to the partition functions, see Table 4.1. The difference between two states 1 and 2 is $\Delta A_{21} = A_2 - A_1$. This macroscopic difference is microscopically given by the ratio of the partition functions. The momentum integration cancels out, leaving the ratio of the configurational partition function, see Eq. (4.27).

$$\Delta A_{21} = -k_B T ln\left(\frac{Z_2}{Z_1}\right) = -k_B T ln\left(\frac{\mathsf{Z}_2}{\mathsf{Z}_1}\right) \tag{4.27}$$

Chapter 5

Molecular dynamics

This chapter gives a short introduction to molecular dynamics with emphasis on the tools used in the computational part of this thesis.

5.1 Computing molecules

There exist mainly two strategies in order to obtain a numerical solution to a microscopic system, the one used in this thesis and mentioned earlier in Chapter 4 is molecular dynamics, the other is Monte Carlo. Monte Carlo is a stochastic approach which probes phase space for the minimum energy configuration by randomly moving particles around. Molecular dynamics is a deterministic way of probing phase space.

In order to get the ensemble average from Eq. (4.11), the system needs to be evolved towards infinity. This is of course not possible and fortunately not needed either. It is sufficient to sample the most probable microstates, although fascinating information can be found in the less probable states. Molecular dynamics replaces the integral in Eq. (4.11) with the sum over the discrete steps taken in the numerical solution. This gives the time average in Eq. (5.1), with t=nΔt, n is the number of discrete steps and Δt is the step size .

$$\langle A \rangle_{time} = \frac{1}{t} \sum^{t} A\left(\boldsymbol{p}(\,t\,), \boldsymbol{r}(\,t\,)\right) \tag{5.1}$$

The total needed runtime will depend on the system in question, but it must be long enough to ensure that the dynamic changes have damped out. This means that the system average should not contain any memory of startup and adjustment into stability. The average of a given number of steps is then equal to the average of the next set of steps. Molecular dynamics is thus performed with an equilibration run into stability, followed by a production run giving the averages.

5.1.1 Time algorithms

In order to obtain the numerical solution a time integrator is needed. There exist several ways to solve the second order ODE's following from Newton's second law, among others the Runge-Kutta method or a predictor-corrector method. These methods can be used to solve ODE's, but are not well suited for molecular dynamics. Among several desirable qualities of the integration scheme, the energy conservation and the time reversibility are needed to obtain a physical solution[36, p.76]. The simplest way to acquire an algorithm with these properties is through a Taylor expansion [37], if this is done by the means of two third order Taylor expansions around the starting position at t=0. One expansion is moving forward in time to step n+1, see Eq. (5.2), and the second is moving back in time to step n-1, see Eq. (5.3). The final result after summing the two expansions is the Verlet algorithm, which is a fast time-reversible scheme for integrating Newton's second law where the errors cancels.

$$\boldsymbol{r}_{n+1} = \boldsymbol{r}_n + \underbrace{\frac{\partial \boldsymbol{r}_n}{\partial t}}_{\dot{\boldsymbol{r}}=\boldsymbol{v}_n} \Delta t + \frac{1}{2!} \underbrace{\frac{\partial^2 \boldsymbol{r}_n}{\partial t^2}}_{\ddot{\boldsymbol{r}}=\boldsymbol{a}_n} \Delta t^2 + \frac{1}{3!} \frac{\partial^3 \boldsymbol{r}_n}{\partial t^3} \Delta t^3 + \underbrace{O\left(\Delta t^4\right)}_{error} \tag{5.2}$$

$$\boldsymbol{r}_{n-1} = \boldsymbol{r}_n - \frac{\partial \boldsymbol{r}_n}{\partial t} \Delta t + \frac{1}{2!} \frac{\partial^2 \boldsymbol{r}_n}{\partial t^2} \Delta t^2 - \frac{1}{3!} \frac{\partial^3 \boldsymbol{r}_n}{\partial t^3} \Delta t^3 + O\left(\Delta t^4\right) \tag{5.3}$$

Summing and rearranging.

$$\boldsymbol{r}_{n+1} = 2\boldsymbol{r}_n - \boldsymbol{r}_{n-1} + \ddot{\boldsymbol{r}}_n \Delta t^2 + O\left(\Delta t^4\right) \tag{5.4}$$

One disadvantage with the Verlet scheme is that the velocity is not given straight forward, it needs to be collected from the positions at n+1 and n-1. This is done by taking the difference of Eq. (5.2) and Eq. (5.3) and rearranging with regards to velocity, see Eq. (5.5).

$$\dot{\boldsymbol{r}}_n = \frac{\boldsymbol{r}_{n+1} + \boldsymbol{r}_{n-1}}{2\Delta t} + \frac{O\left(\Delta t^3\right)}{\Delta t} \tag{5.5}$$

This gives an error of Δt^2 in the velocity for one iteration. On a large time-scale of n iterations this error will grow, demanding even smaller time-steps. The error in the velocity calculation will be squared in the kinetic energy leading to poor energy conservation.

$$O(t) = O(n\Delta t^2) = O(\frac{t}{\Delta t}\Delta t^2) = O(t\Delta t)$$

One way to improve the velocity calculation is to reduce Newton second law into two first order ODE's, respectively velocity and acceleration. Then do a Taylor expansion of velocity at t=0 and combine with Eq. (5.2). This will increase the truncation error in the position by one order of magnitude, but at the same time decrease the error in the velocity by the same amount. This is done by approximating the third derivative of position by doing a Taylor expansion of the acceleration Eq. (5.7), and leads to the familiar velocity-Verlet algorithm[23, p.452], following below.

$$\dot{\boldsymbol{r}}_{n+1} = \dot{\boldsymbol{r}}_n + \ddot{\boldsymbol{r}}_n \Delta t + \frac{\dddot{\boldsymbol{r}}_n}{2}_n \Delta t^2 + O\left(\Delta t^3\right) \tag{5.6}$$

$$\ddot{\boldsymbol{r}}_{n+1} = \ddot{\boldsymbol{r}}_n + \dddot{\boldsymbol{r}}_n \Delta t + O\left(\Delta t^2\right) \tag{5.7}$$

Rearranging Eq. (5.7) with respect to the third order derivative of position gives.

$$\frac{\dddot{\boldsymbol{r}}_n}{2} = \frac{\ddot{\boldsymbol{r}}_{n+1} - \ddot{\boldsymbol{r}}_n}{2\Delta t} + O\left(\Delta t\right) \tag{5.8}$$

By truncating Eq. (5.2) after the second term and inserting Eq. (5.8) into Eq. (5.6) the velocity verlet algorithm Eq. (5.9) is obtained.

$$\dot{\boldsymbol{r}}_{n+1} = \dot{\boldsymbol{r}}_n + \frac{\ddot{\boldsymbol{r}}_{n+1} + \ddot{\boldsymbol{r}}_n}{2} \Delta t + O\left(\Delta t^3\right)$$

$$\boldsymbol{r}_{n+1} = \boldsymbol{r}_n + \dot{\boldsymbol{r}}_n \Delta t + \frac{\ddot{\boldsymbol{r}}_n}{2} \Delta t + O\left(\Delta t^3\right) \tag{5.9}$$

The velocity Verlet conserves the kinetic energy better than the verlet algorithm by using the average force, of step n and n+1, to compute the velocity.

The above integration schemes uses a single time step for all forces in the system. If the system consists of forces from a light atom oscillating in a bond to long-range electrostatics, a large time-step will cover the slow long-range forces, but will not cover the fast forces in the bond. A short time step will be computational expensive as the change in the slow forces are small. This is a disadvantage for the single time step, but an advantage that can be exploited if the velocity Verlet is derived in a more powerful way. Utilizing the Liouville operator to propagate the system through time makes it possible to separate the fast forces from the slow forces. The forces are then factorized using the Trotter theorem[25, Appendix C]. This procedure is known as the RESPA-algorithm and makes it possible to do multiple time-scale integration while preserving the reversibility of the system. Leading to one time scale δt for the fast forces and a time scale Δt for the slow forces. With an integer number of small time steps, δt, in one long time step, Δt. The multiple time scales obtained with RESPA-algorithm leads to the velocity verlet algorithm given in Eq. (5.9). More information on multiple time-scale integration is given in [25, Chapter 3.11].

5.1.2 Ensembles in molecular dynamics

As discussed in Chapter 4, one often want to perform the calculation in other ensembles than the microcanonical, because the observed values are easier to measure. This represents a challenge for molecular dynamics, which by probing the constant energy surface is naturally connected the microcanonical ensemble. There exists several ways to solve this, if the goal is to perform a NVT simulation. The easiest way to keep the temperature constant would be to scale the velocities at each time step to achieve the desired temperature. This procedure is known as velocity scaling and is beneficial when starting a simulation, as one can obtain better velocities and positions for the particles. This procedure does not follow an ergodic trajectory through phase space and will thus not reproduce a canonical ensemble. Although several procedures have been developed to keep the temperature constant, for example the Anderson thermostat and the Berendsen thermostat, it is the Nosé-Hoover thermostat that has ended up as the main temperature controlling tool in molecular dynamics. To produce a canonical ensemble the system Hamiltonian must be allowed to change, as long as the temperature of the system corresponds to the given temperature and the total energy of system and surroundings are constant. The Nosé-Hoover thermostat has been shown to have this capability and can reproduce the canonical ensemble, the equation of motion is given in Eq. (5.10).

$$\begin{aligned}
\dot{\boldsymbol{r}}_i &= \frac{\boldsymbol{p_i}}{m_i} \\
\dot{\boldsymbol{p}}_i &= \boldsymbol{F}_i\left(\boldsymbol{r}\right) - \frac{p_\eta^2}{Q}\boldsymbol{p_i} \\
\dot{p}_\eta &= \sum_{i=1}^{N} \frac{\boldsymbol{p}_i^2}{m_i} - dNk_BT
\end{aligned} \tag{5.10}$$

Where p_η is a "friction" or coupling term which exchange energy with the reservoir to keep the temperature in the system constant, second line Eq. (5.10). The dNk$_b$T term is the canonical average temperature over d dimensions. From the third line in Eq. (5.10) one can see that the driving force for the "friction" term is the difference between the instantaneous kinetic energy of the system and the canonical average. The η term, which is equal to $\dot{\eta} = \frac{p_\eta}{Q}$ was included by Martyna et al. [38] for analysis. This leads to a conserved energy of the form given in Eq. (5.11) [25, p.184]. The prime indicates that this is a non-Hamiltonian equation, because the equation of motion cannot be derived directly from it.

$$\mathscr{H}`_{NH}\left(\boldsymbol{p},\eta,\boldsymbol{r},p_\eta\right) = \underbrace{\mathscr{H}\left(\boldsymbol{p},\boldsymbol{r}\right)}_{system} + \underbrace{\frac{p_\eta^2}{2Q} + dNk_bT_\eta}_{Heat\ \ reservoir} \tag{5.11}$$

The Nosé-Hoover Hamiltonian is a sum of two parts, the system Hamiltonian, equal to the Hamiltonian in Eq. (4.8) giving the complete microscopic description of the system, and a non-Hamiltonian part constituting the heat-bath. The variables describing the heat-bath are fictional variables, because the microscopic description of the surroundings are of no importance as long as the Nosé-Hoover Hamiltonian generates the canonical distribution. The analyses done by Tuckerman [25] shows that the Nosé-Hoover dynamics is able to produce the canonical distribution, when Eq. (5.11) is the only conserved quantity. If the system also has to follow Newton's third law then the Nosé-Hoover dynamics fails. In this case the canonical distribution can be achieved by including a Nosé-Hoover chain of thermostats. The crucial variable to tune in the Nosé-Hoover formalism is the 'mass' Q of the thermostat, which can be given in terms of the relaxation time, τ, see Eq. (5.12) [39]. A proper choice of the relaxation time is needed for the systems to have an ergodic trajectory through phase space, see Kuznetsova and Kvamme [40].

$$Q = dNk_b\tau^2 \tag{5.12}$$

The isobaric-isothermal ensemble can be created in a way similar to the canonical ensemble. By introducing fictional variables responsible for changing the system volume so the system pressure remains constant i.e. the system is connected to a work reservoir alongside with the heat reservoir. The grand-canonical ensemble is created by connecting the system to a particle reservoir alongside with the heat reservoir.

5.1.3 Periodic boundary conditions

Molecular dynamics usually employs the periodic boundary conditions, in order to avoid the problem of how the system interacts at the boundaries. The system is surrounded by an infinite number of identical copies. When one molecule leaves one image it enters a new identical simulation box, in which an identical molecule has moved over to the next periodic image, this is illustrated in Figure 5.1. Consequently a molecule leaving the simulation box at one side will just reenter the box on the other side when visualized. The total box will mathematically be given by $\boldsymbol{n} = \{\boldsymbol{n}_x L_x, \boldsymbol{n}_y L_y, \boldsymbol{n}_z L_z\}$, with L giving the initial box size in Cartesian space, and the integer vectors $\boldsymbol{n_x}, \boldsymbol{n_y}, \boldsymbol{n_z} = \mathbb{Z}$ giving the simulation box when $\boldsymbol{n_x}, \boldsymbol{n_y}, \boldsymbol{n_z} = 0$ and the copies when $\boldsymbol{n_x}, \boldsymbol{n_y}, \boldsymbol{n_z} \neq 0$. It would also be computational expensive to evaluate the pair-interactions over all distances, so a cut-off distance is employed and only the interactions within cut-off distance is evaluated. This is shown in figure 5.1, alongside with the nearest image convention. Nearest image convention means that a particle in the simulation box interacts with the particles in the next periodic image if the particle in this image is within cut-off distance. The cut-off distance alone will significantly improve the computational speed, because of the need to evaluate if the particles are within cut-off or not, so one more tool is needed. This tool is the neighbor list also called Verlet list, all neighbors of a particle i within a distance $R_{cut} + \delta$ is then determined and saved at the start of the simulation. The displacement of the particles from the initial position is determined at each time step and if this displacement for one particle is larger than $\frac{\delta}{2}$ the list needs to be updated. Using a cut-off distance represents

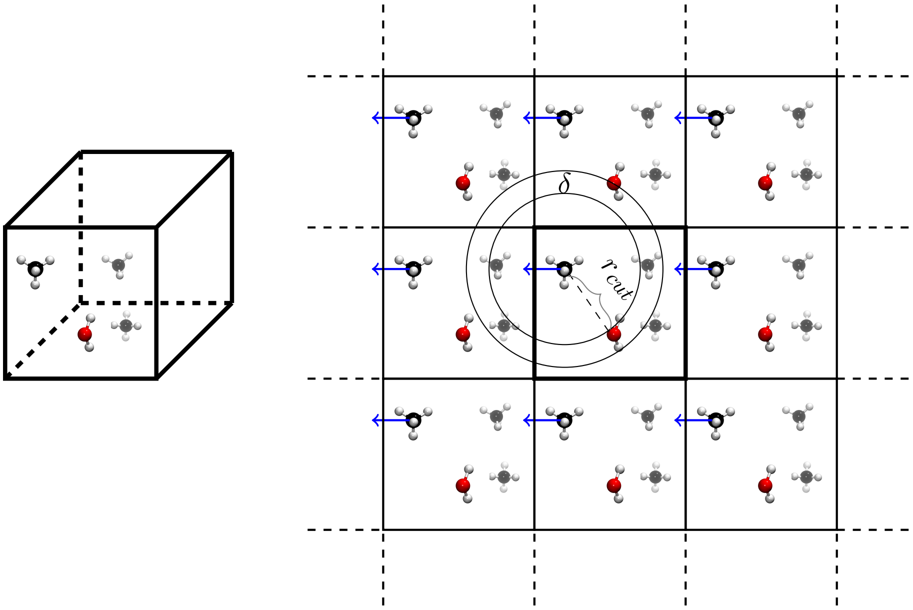

Figure 5.1: Figure showing the use of periodic boundary conditions, the simulation box is shown to the left. This box is surrounded by identical boxes shown in two dimensions to the right. The cut off distance for evaluating the short-range forces are indicated by the circle, alongside with the nearest image convention. δ is the distance between the two circles and determines how often the neighbor list should be updated.

no problem for the short-range interactions, if the cut-off is long enough. These interactions tend towards zero with $(1/\boldsymbol{r}^6)$, and will thus disappear, see Figure 4.6. For the long-range interactions a cut off distance will represents a problem. If the distribution of particles are assumed to be homogeneous, the number of particles will grow as $N = \frac{4}{3}\pi r^3 \rho_N$. The electrostatic energy falling off with $(1/\boldsymbol{r})$ will thus diverge with r^2. The truncating at a cut-off distance will in this case invoke a large error in the calculations and introduce a discontinuity in the forces.

5.1.3.1 Ewald summation

The problem mention above is in this thesis handled with the Ewald summation method. The total long-range electrostatic energy is given by summing Eq. (4.23) over all images and all particles, see Eq. (5.13)

$$U_{Long-range} = \frac{q_i}{4\pi\epsilon_0} \sum_{n=-\infty}^{n=\infty} \sum_{j=1}^{N} \frac{q_j}{|\boldsymbol{r}_{ij} + n|} \tag{5.13}$$

As the sum in Eq. (5.13) is periodic and runs to ∞ it would take a large computational effort to evaluate it. This is eased out by evaluating the electrostatics up to cut-off and then Fourier transform the interactions beyond cut-off into k-space or reciprocal space. To do this, the distance dependency is written using the error function.

$$\frac{1}{r} = \frac{erfc\,(\alpha r)}{r} + \frac{erf\,(\alpha r)}{r} \tag{5.14}$$

The α has units Å^{-1} and is in this case a parameter which tunes the range the error function is non-negligible. erfc(αr) is the complementary function to erf(αr) and the sum erf(αr)+erfc(αr)=1. The complementary function will decay rapidly with increasing distance, this term can be incorporated into the short-range interactions evaluated within cut-off distance. The second term in Eq. (5.14) represents the interactions beyond cut-off distance, and is thus the term that is left in the long-range interaction. It still takes a large computational effort to evaluate this expression, but the advantage is that the error function can be expanded in a Fourier series. The long-range interactions in real space will be short-range in reciprocal space, thus saving computational resources.

$$\sum_{n=-\infty}^{n=\infty} \frac{erf\,(\alpha|\boldsymbol{r} + \boldsymbol{n}|)}{\boldsymbol{r} + \boldsymbol{n}} = \frac{1}{V} \sum_{\boldsymbol{g}} C_{\boldsymbol{g}} e^{-i\boldsymbol{g}\cdot\boldsymbol{r}}$$

with the expansion coefficients C_g

$$C_{\boldsymbol{g}} = \frac{4\pi}{|\boldsymbol{g}|^2} e^{\frac{-|\boldsymbol{g}|^2}{4\alpha^2}} \tag{5.15}$$

$\boldsymbol{g} = \dfrac{2\pi\boldsymbol{n}}{L}$ is the reciprocal space vectors. It would be impossible to evaluate the infinite sum of all $\boldsymbol{g}$ but as the exponential factor in the expansion coefficients tends quickly towards zero with increasing numbers of $\boldsymbol{g}$. The sum can be truncated with a finite number of $|\boldsymbol{g}| \leq g_{max}$ such that the exponential factor is negligible. The total formula for the Ewald summation would take an extensive derivation to arrive at, so the reader is redirected to [25, Appendix B] or Kuznetsova and rn Kvamme [41]. The discussion in this thesis is ended by the fact that one can write the total $U_{electrostatic} = U_{real} + U_{reciprocal} - U_{self}$. Where U_{real} is the evaluated in real space alongside with the Lennard-Jones or Buckingham contribution and the remaining long-range electrostatic is evaluated in Fourier space, U_{self} is the correction for self-interactions.

5.2 Calculations in molecular dynamics

This is a short overview of the calculation possible from the molecular dynamic simulations.

5.2.1 Free energy

The free energy difference was given in Eq. (4.27) as the ratio of the partition functions. This is reduced to the ratio of the configurational partition functions when the momentum integration cancels. Since molecular dynamics calculates averages of phase space, but does not give direct access to the full partition function one need another approach. One approach suited for molecular dynamics is the free energy perturbation formula[25, p.316], but this is only possible if the energy difference of state 2 and state 1 is small. Another solution is to introduce a switching variable, λ, changing between 0 and 1, thus creating intermediate states. In this case a new potential energy function is defined as the sum of the potential energy function of state 1 and for state 2, each multiplied by a switching function. Since the parts of the potential energy decays differently the switching variable can be extended with an exponential factor, a procedure known as known as polynomial path[42]. In this way the slow decaying parts of the potential is faster switched towards the second state avoiding that the repulsive part of the potential is switched off to fast, compared to the attractive part. If this was not the case one would risk the particles clumping together. For potentials with an exponential repulsive part as in Eq. (4.19) Kuznetsova and Kvamme [43] found that including an exponential coupling function improved the calculations. The total Helmholtz free energy difference is then written as in Eq. (5.16)[43].

Eq. (5.16)

$$A_1 - A_0 = \int_0^1 \sum_{k_i} k_i \lambda^{k_i - 1} \langle U_i \rangle_\lambda + \frac{k_{exp}}{\lambda} \left\langle \frac{\rho}{\lambda^{k_{exp}}} r U_{exp} \right\rangle_\lambda d\lambda \tag{5.16}$$

Where k_i is the lambda exponents on potentials decaying with $\frac{1}{\boldsymbol{r}^i}$ where i runs over the different parts of the potentials i.e. 12, 6 and 1. k_{exp} is the lambda exponent on the lambda used in the $U_{exp} = e^{-\frac{\rho r}{\lambda^{k_{exp}}}}$. The lambda subscript on the average bracket indicates the specific lambda value used in the simulations which the average is taken on. Each term in the integral is equal to the ensemble average of the partial derivative of the potential energy with respect to λ. Which again is equal the partial derivative of Helmholtz energy with respect to lambda, this connection comes from the connection in Table 4.1, and the derivation is shown in [25, Chapter 8.2]. Integrating from $\lambda = 0$ to $\lambda = 1$ gives the free energy difference. Where A_0 in this case is an ideal system, meaning that the potential energy $U_0 = 0$, while A_1 is a real system. So the ideal system is slowly transformed to a real system when $\lambda \to 1$. The difference in the free energy then gives the excess or residual free energy, respectively depending on if the reference state is liquid or gas. The polynomial path integration has an advantage over temperature integration because fewer simulations are needed. Temperature integration takes typically ten simulations from the target temperature up to a temperature where molecule interactions are negligible. At high temperature one can get into trouble with a Buckingham type potential, as the high kinetic energy can overcome the maximum value of the repulsive part of the potential. The particles will then experience an unphysical infinite attraction when $\boldsymbol{r}_{ij} < \lambda r$, see Figure 4.6, not the same lambda as the one used in the polynomial path integration. The polynomial path integration typically need 3 or 5 simulations at different lambda values, it is thus faster to perform and computational less expensive.

5.2.2 Radial Distribution Function

From Eq. (4.26) it is possible to derive a n-particle correlation function, the special case when n=2 is called a pair-correlation function. From the pair-correlation function the radial distribution function follows by considering the relative center-of-mass coordinates of particle 1 and particle 2, and change to polar-coordinates before integrating over all angles. The radial distribution function can be connected to scattering intensities from neutron or x-ray measurements yielding a way to compare the observed structure to the calculated one. It can be implemented in a molecular dynamics code as done in [44], or in the visualization and analyzing tools as done in [45]. The functional form of the radial distribution function, $g\left(r\right)$, is given in a simplified form in Eq. (5.17). The more rigorous form derived from statistical mechanics can be found in [25, p.154] and the form implemented in molecular dynamics in Levine et al. [45].

$$g\left(r\right) = \frac{\left\langle N\left(r\right)\right\rangle}{4\pi\frac{N}{V}r^{2}dr} \tag{5.17}$$

Where r denotes the radial distance and dr is the shell, the nominator gives the average number of atoms in a the shell dr. The shells dr are illustrated in Figure 5.2. The denominator is the normalization to an ideal system, so in the case of $g\left(r\right)$=1 there will be no structural ordering. A plot of a radial distribution function is shown in Figure 5.3. The zero probability of finding a particle at short distances is due to the repulsive part of the potential energy, while the first peak is due to the attractive part of the potential which coordinates a first shell of particles around a central particle. This shell repulses some of the particles at longer distances giving the first minima before a second shell forms. As the distance increases the $g\left(r\right)$ settles to one and the potential energy tends towards zero, see Figure 4.6. Integrating the radial distribution

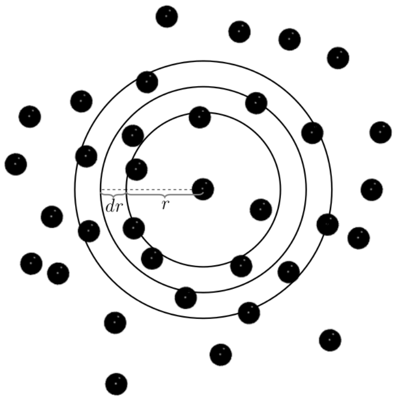

FIGURE 5.2: Illustration of the distribution of particles around a central particle. The number of particles in each shell dr a distance r from the central particle is counted in each time frame from a molecular dynamic simulation and then averaged over the number of frames.

function over all distances gives the number of particles in the system, while integration to the first minima gives the number of particles in the first shell. The radial distribution function can also be used to determine the second virial coefficient in the virial equation of state.

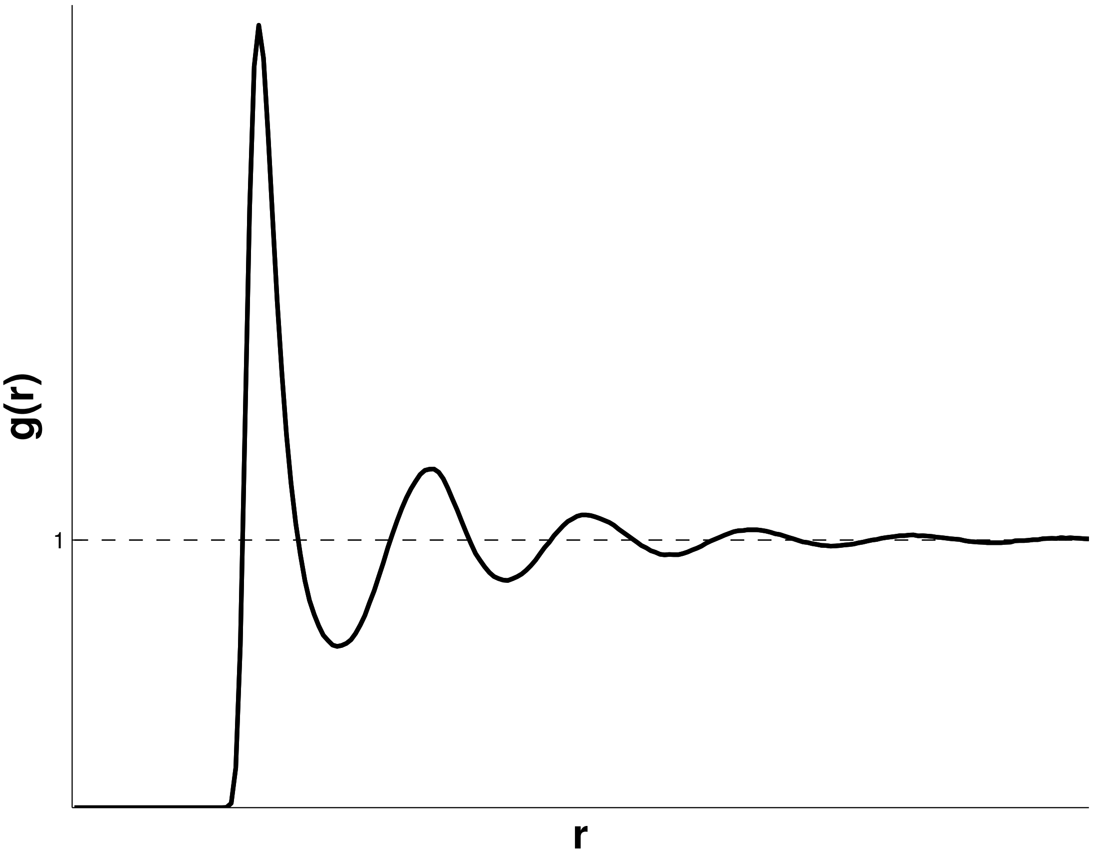

FIGURE 5.3: Radial distribution function from an illustration run of liquid methane using the MDynamix 5.1 package [44] to obtain the trajectories, the radial distribution function was calculated using vmd [45, 46] and plotted in MATLAB [47].

5.2.3 The diffusion coefficient

The diffusion coefficient is a measure of the tendency particles have to drift through a system under the action of a constant external force, Tuckerman [25, Chapter 13.3.2]. The diffusion coefficient can be derived from both experimental studies, and from molecular dynamics. Therefore many molecular dynamic simulations aim on collecting this property, giving a good foundation to validate performed simulation against literature values. From a molecular dynamic simulation there exists two ways to obtain the diffusion coefficient. The first is from the velocity autocorrelation function [25, p.509] and the second is from the Einstein relation between the diffusion coefficient and the average mean square displacement. The latter is used in this thesis and given by Eq. (5.18).

$$D_s = \frac{1}{2d} \lim_{t \to \infty} \frac{d}{dt} \underbrace{\frac{1}{N} \sum_{i=1}^{N} \left\langle \left| \boldsymbol{r}_i\left(t\right) - \boldsymbol{r}_i\left(0\right) \right|^2 \right\rangle}_{MSD} \tag{5.18}$$

Where D_s is the self-diffusion coefficient and d is the number of dimensions equal to 3 in the case of diffusion in x, y and z directions. MSD is the mean square displacement, equal to the squared distance a particle i has travelled between t=0 and t=t averaged over all particles. As the particles starts travelling in the system they travel in one direction until they encounter other particles. This ballistic behavior gives a mean square displacement proportional to t^2. The true random walk starts when the particles are encountering other particles that make them change positions randomly. In this case the MSD plot will be proportional to t. The diffusion coefficient is then given from the derivative of the mean square displace averaged over time and dimensions, see Eq. (5.18).

Chapter 6

Computational details

The following section gives an introduction to the previous work done in the THEMOD group which this work continued from. Furthermore, the development and testing of the new methane-zeolite model is explained, alongside with simulations details and analysis performed in this work.

6.1 Introduction

The work done by Jensen et al. [1, 2] was the starting point for the molecular dynamics simulations performed in this work. Jensen et al. [1, 2] used the potassium model of Jackson and Catlow [48], potassium in faujasite, alongside with the host-structure and water model of Faux et al. [16]. Faux et al. [16] transferred interatomic potentials for related systems, to create a model for hydrated and dehydrated zeolite NaA. Faux et al. [16] based his work on the work done by Jackson and Catlow [48] on the zeolite NaA structure, and the water-zeolite work done by Leherte et al. [49] on water in ferrierite. The water-water interactions are described by the SPC/E model of Berendsen et al. [50]. The hydrated zeolite KA model use the Lennard-Jones potential for all interactions except $K^+ - O_w$, $K^+ - O_{zeo}$ and $O_{zeo} - O_w$ that use the Buckingham potential. This is the model used throughout the investigation of polynomial path integration for water in zeolite KA .

To describe the methane-zeolite and methane-methane interactions, Jensen et al. [1] used the methane model of Jorgensen et al. [51], and the Lorentz-Berthelot mixing rules. Results obtained by Jensen et al. [1] indicated that the OPLS methane sphere, even though it correctly describes bulk methane, was too big to correctly describe the zeolite-methane interactions. This thesis continue the investigation of methane-zeolite interactions.

Several models were investigated to describe the methane-zeolite interaction among others the 5-site methane model used by Catlow et al. [52], the model of Garcia-Sanchez et al. [53], which use the OPLS model for methane but has a different model for the zeolite structure. Because the model by Jackson and Catlow [48] has been frequently used due to the ability to reproduce experimental measurement and also contained parameters for potassium in zeolite, it was not desired to change the zeolite model. Jackson and Catlow [48] used the Buckingham potential, it was thus tempting to use these original parameters and change the pure methane potential. The model of Tsuzuki et al. [54] was chosen for methane because of the ability to reproduce pure methane diffusion. Furthermore, the idea was that a Buckingham potential, in the close confinement of a zeolite structure, would better describe the repulsion between the zeolite structure and the methane guest molecules compared to a LJ-model. To my knowledge a pure Buckingham potential between guest molecules and host zeolite has never been used before, at least not for methane in zeolite A. The main reason for this is the computational expense of a Buckingham potential, usually the Lennard-Jones potential is used by fitting to experimental data of zeolite and guest molecule. This was not a possibility, due to the lack of experimental data, although Statoil plans on starting an experimental plant using the zeolite KA.

The work in this thesis can be divided into two parts, one part that consists of testing the methane potential in zeolite and a short investigation into methane zeolite KA interactions. The other part consists of checking if it is possible to use polynomial path integration to obtain excess energy for water in zeolite. The testing of the Buckingham potential for methane in zeolite was done on a LTA zeolite without counter-ions, denoted as LTA^{-96}, because of the large amount of data published on this type of system. The LTA^{-96} is practical because it reveals the effect the counter-ions have when included in the simulation. Although, it is hypothetical because of the unbalanced charge, there have been reported experimental values for low methane loading in a high silicon zeolite A[55]. The LTA^{-96} should not be confused with the LTA_{Si} zeolite where aluminium has been replaced by silicon.

6.2 The methane zeolite model

The different parameters for the model tried in this thesis follows below, and starts with the parameters for methane from Tsuzuki et al. [54], given in Table 6.1.

TABLE 6.1: Five-site Buckingham parameters for methane, from Tsuzuki et al. [54].

	A $\left(\frac{kJ}{mol}\right)$	ρ (Å)	C $\left(\frac{kJ \cdot \mathring{A}^6}{mol}\right)$
C	7924	0.371	1880.83
H	8807	0.298	216.35

From the reported reduction factor of the C-H bond length in Tsuzuki et al. [54], the positions of the hydrogen atoms was calculated using polar coordinates. The xyz-coordinates used in the simulations are given in Table 6.2.

TABLE 6.2: xyz-coordinates for methane, from Tsuzuki et al. [54].

	x (Å)	y (Å)	z (Å)
C	0.000	0.000	0.000
H1	0.000	0.000	0.942
H2	0.888	0.000	-0.314
H3	-0.444	-0.769	-0.314
H4	0.444	0.769	-0.314

Tsuzuki et al. [54] used a rigid methane molecule which reduces the internal degrees of freedom to translation and rotation. To include vibration, the bonded parameters of Catlow et al. [52] was also implemented, these are given in Table 6.3.

TABLE 6.3: Bonded parameter for methane, from Catlow et al. [52].

Bond			Angle		
	r_e (Å)	K_b $\left(\frac{kJ}{mol \cdot \mathring{A}^2}\right)$		θ (°)	K_a $\left(\frac{kJ}{mol \cdot rad^2}\right)$
C-H	0.942	2991.0	H-C-H	109.47	327.08

Jackson and Catlow [48] reported three different models for the zeolite structure, the model used in this thesis is the fixed framework model from Table 1 in Jackson and Catlow [48]. These parameters are given as the pair-potential against oxygen. To implement the methane model of Tsuzuki et al. [54] the pure potentials were obtained using the mixing rules of Eq. (4.22), see Table 6.4. The pure zeolite parameters could then be mixed with the methane parameters using the same rules. The charges were taken from the work of Faux et al. [16].

TABLE 6.4: Buckingham parameters for LTA3A zeolite, from Jackson and Catlow [48].

	A $\left(\frac{kJ}{mol}\right)$	ρ (Å)	C $\left(\frac{kJ \cdot \mathring{A}^6}{mol}\right)$	Charge (e)
Si	4229.6	0.801	0.00	3.70000
Al	9038.5	0.600	0.00	2.77500
O	2196384.5	0.149	2690.00	-1.86875
K	4241.0	0.879	386.57	1.00000

6.3 Software and Hardware

The molecular dynamics program used in this thesis was a modified version of the open-source code MDynaMix Package version 5.1[44, 56]. The modifications was done by Professor Tatiana Kuznetsova who added support for the Buckingham potential Eq. (4.19), alongside with output in Protein Data Bank (.PDB) format. Bjørnar Jensen, who works as Ph.D student at the Institute for Physics and Technology at University of Bergen, added polynomial path integration according to Eq. (5.16) and the option to define specific pair-interactions through a force field (.ffield) file. The .ffield was needed in the water-zeolite simulations and the OPLS methane-zeolite simulations.

The fortran code from MDynaMix has some features that limit its usefulness when performing simulations of a zeolite system. First of all, it was not possible to use a flexible zeolite model because the current code does not handle bonds over the periodic images. The fixed zeolite structure caused the program to report incorrect translation temperature, the reason for this is the velocity averaging over all particles, even the fixed ones. Furthermore, the program treated each site in the zeolite structure as one molecule, thus the non-bonded interactions between sites in the zeolite structure was calculated. This lead to incorrect values for the total energy, because the zeolite structure should been treated as one molecule. Consequently the program calculated incorrect pressure from the energy. Nonetheless, when specific properties of the guest molecules are considered, these are calculated separately and not affected by problems caused by the fixed zeolite framework. Furthermore, because all simulations have been performed in the canonical ensemble, the pressure has only informative value.

All simulations were performed on the Cray system hexagon[57].

6.4 The simulations

The MD51 package needs several input files containing the computational setup for the simulation. The .mmol files contain the force-field and the structure data of each of the species, while the mixing-rules are given in a separate file. A .start file contains the positions of all the species at the start of the simulation. The last file is the .input file with the setup for molecular dynamics, as discussed in Chapter 6. In the case of water or OPLS methane in zeolite a .ffield file is also used. The path to obtaining results from a molecular dynamics simulation can be divided into three parts, creating the initial start-up files, running the simulations and analyzing the results.

6.4.1 Building the simulations

The coordinates for the atoms in the zeolite structure was kindly shared by Bjørnar Jensen, who collected them from the IZA-SC [58] based on the work by Pluth and Smith [59]. When counter-ions were included in the simulation all the 64 sites in the 6T-windows and 24 sites in the 8T-windows was filled, while 8 of the sites at the 4T-window displaced into the α-cavity was filled, this work was done by Bjørnar Jensen. The parameters for zeolite, according to Faux et al. [16], and OPLS methane was also shared by Bjørnar Jensen, through a .ffield file. The parameters for the counter-ion were removed from this file, to create the simulation of OPLS methane in counter-ion free zeolite.

The zeolite structure was filled with methane using the VMD [46] solvation tool, this tool fills the simulation box with water, which then was replaced with methane. Because methane is too big to enter the β-cages, water molecules at these positions were deleted, this was done using the VMD selection tool. This was a time consuming process that ended up with 66 methane molecules located in the eight α-cavities. Simulations were performed using both the Tsuzuki-model and the OPLS-model. The same center mass positions was used for both models, and the hydrogen atoms in the Tsuzuki-model added using the MOL_COM startup option in MD51. This option reads in the center of mass positions and adds sites according to the positions specified in the .mmol file.

García-Sánchez et al. [60] reported, from molecular dynamics simulations, the diffusion of methane for fifteen different loadings, ranging from 1 methane pr α-cavity to 15 methane pr α-cavity. To compare the Tsuzuki-model to these values, a total of thirteen simulations were created, this could not have been done within reasonable time using the simple selection procedure. Therefore, a tcl script taken from the NAMD tutorial page[61] was slightly modified for the purpose of putting water molecules into an α-cavity. The script's original purpose was to immerse a molecule in a water sphere. This sphere was put into a for-loop, which changed the diameter, while an if-statement was responsible for writing out the positions of the water molecules, when the needed number was achieved. The modified script, was first run on a selection of one α-cavity, and then the water molecules were copied to the other cavities. The obtained initial positions were often in non-favorable places, this meant that the C-H bond in the Tsuzuki-model, could be stretched too far. Therefore, the simulations were first run with the OPLS-methane sphere until better positions were obtained. Typically this took about 100000 steps, with a time step of 0.01 fs using velocity scaling to control the temperature. García-Sánchez et al. [60] stated they had replaced the aluminium atoms with silicon atoms, when they create the LTA$_{Si}$ simulation, as a consequence of this, one simulation with the aluminium site replaced with silicon was also built.

The same modified water sphere script, was used for filling the zeolite structure with water. 224 water molecules was put into the α-cavities, to create a fully hydrated unit-cell. The simulation was then run for 500 ps to equilibrate the system and obtain better starting positions, using velocity scaling, a long time step of 0.1 fs and a short time step of 0.01 fs.

6.4.2 Running the simulations

All simulations were performed using a cubic 24.55 Å PBC box. The electrostatics was treated using Ewald summation, with a Ewald convergence parameter $\alpha = 2.8r_{cut}$, see Eq. (5.14), and 9 terms in the reciprocal part, according to the recommended values in the MD51 user manual [56]. A r_{cut} of 12 Å was used for the short-range forces i.e. the Lennard-Jones, Buckingham and real-space part of electrostatics, when using the long time step. For the short-time step a r_{cut} of 6 Å was used.

Diffusion of methane

The methane simulations used a long time step of 0.5 fs. The Tsuzuki-model used a small time step of 0.005 fs, due to the C-H bond, while the OPLS-model used a small time step of 0.05 fs. All methane simulations were performed in the canonical ensemble using a separate Nosè-Hoover thermostat for each specie, and a relaxation time of 15 fs. The temperature in the simulations was set to 500K, this is the temperature García-Sánchez et al. [60] used, and also close to the temperature, 503 K, used under regeneration at Snøhvit. The trajectory was dumped every 50 fs and an equilibration run of 500 ps was used before any calculations on diffusion was performed. Except for the two smallest systems, the 24 methane and the 32 methane, for which a 1 ns equilibrium run was used. The simulations with 66 methane molecules are summarized in Table 6.5.

Table 6.5: The simulations performed with 66 methane molecules in one unit-cell of zeolite A.

Methane ffield	zeolite structure	Time (ns)	CPU‘s
OPLS	LTA^{-96}	1.5	32
Tsuzuki	LTA^{-96}	1.5	32
Tsuzuki	LTA_{Si}	1.5	32
Tsuzuki	LTA-3A	5	32

The 5 ns simulation of methane in LTA-3A zeolite used a computational time of ~121 hours. The run length of the simulations used in comparison to the data reported by García-Sánchez et al. [60] are given in Table 6.6. The small systems achieved a run time of 5 ns, needed to obtain a good measure of diffusion, in ~ 96 hours. As the loading increased so did the computational time, at the same time the diffusion also increased up to a loading of 72 methane molecules. This meant that less run time was needed for the systems with high diffusion. The largest system with 120 methane molecules took $\sim$ 141 hours to run.

TABLE 6.6: The simulations performed with Tsuzuki methane molecules in one unit-cell of LTA^{-96}

Simulation (*number of methanes*)	Time (*ns*)	CPU's
24	5	32
32	5	32
40	5	32
48	5	32
56	3	32
64	3	32
72	2.5	32
80	2.5	32
88	2.5	32
96	3	32
104	3	48
112	3	48
120	3.5	48

PPTI for water in zeolite

The Polynomial path integration for water in zeolite was performed for λ equal to 0.1125, 0.5 and 0.8875. 224 water molecules were simulated in a constant zeolite unit-cell. The temperature was set to 298 K ±5 K using separate velocity scaling. One control run using the Noseé-Hoover thermostat was also performed. The runtime was set to 50 ps to check the scaling of the electrostatic exponent, K_1. The other exponents was held constant at K_6=3, K_{12}=4 and K_{exp}=0.25. Further runs were performed for 2 ns, with K_1=2, while K_6 and K_{12} was changed. The average in the 50 ps runs was taken after 15 ps, while the 2 ns runs was averaged after 500 ps. The exponents K_1=2, K_6=3, K_{12}=4 and K_{exp}=0.25 was used both for the short runs and the long runs, to check the equilibration of the system. These exponents correspond to the best results obtained for CO_2 by Kuznetsova and Kvamme [43]. The simulations are summarized in Table 6.7, where each set of exponents corresponds to three simulations, one at each λ-value, giving a total of 21 simulations. The exponent K_1=1 was also used for three simulations, but is not included because the simulation at λ=0.1125 crashed after 50 ps.

TABLE 6.7: Simulations performed with polynomial path integration for water. The total simulation time is given in the first column, with the averaging started from the time in the parentheses. The exponents for each part the potential are given in the following order electrostatic, attractive LJ/Buckingham, repulsive LJ and repulsive Buckingham.

Time(ps)	K_1	K_6	K_{12}	K_{exp}
50(15)	2	3	4	0.25
	3	3	4	0.25
	4	3	4	0.25
2000(500)	2	2	3	0.25
	2	2	4	0.25
	2	3	4	0.25
	2	4	4	0.25

6.5 Analysing the results

The resulting trajectories from the simulations were analyzed using VMD [46]. The PBC unwrap tool in VMD was used to remove the periodic boundary conditions, which was needed to obtain the correct mean square displacement. The root mean square displacement(RMSD) tool in VMD was used to obtain a plot of RMSD against frame number. The density profiles were obtained from the VMD Density Profile Tool(beta) [62]. The results were plotted and analyzed with MATLAB [47], see Appendice B for MSD script.

The polynomial path integration was performed by fitting a Piecewise Cubic Hermite Interpolating Polynomial (PCHIP) of stepsize 0.0001 and using the trapezoidal numerical integration MATLAB [47]. There is of course some error connected with this approach, as an example integrating x^2 from 0 to 6 gave an error of 50.0 ppm compared to the analytic solution.

Chapter 7

Results and discussion

This chapter starts with the 66 methane simulations, before it moves on to testing the new model and comparing results to literature values. This ends up with a hypothesis for the reduced lifetime of the zeolites. The last part in this section is the PP-TI simulations of water in zeolites.

7.1 MSD for the 66 methane simulations

Four simulations were performed with 66 methane molecules in zeolite A. One simulation using the OPLS methane model and the [16] zeolite model without counter-ions. While two simulations, without counter-ions, were performed with the Tsuzuki methane model and the zeolite model given in Table 6.4, only differing by the aluminium sites being replaced with silicon. The last simulation included potassium and was performed with the Tsuzuki methane model and the full zeolite model given in Table 6.4.

7.1.1 Comparing OPLS and Tsuzuki methane

The plot of the mean square displacement using the OPLS-model, is shown in Figure 7.1, it tends quickly towards a plateau value of ~23 Å^2. Over time it oscillates around this value with a small positive slope of 0.001 $\frac{\mathring{A}^2}{ps}$, this translates into a diffusion coefficient of $\sim 1.7{\cdot}10^{-12}\frac{m^2}{s}$. The static mean square displacement is an indication of a solid [63], and the methane molecules permanently resided in the α-cavities they started in. The diffusion coefficient can be compared to the reported values of García-Sánchez et al. [60], which for a loading of 9 methane molecules pr α-cavity reported a diffusion in the range of $5\ {\cdot}10^{-9}\frac{m^2}{s}$. This clearly shows that the repulsive interactions between the zeolite structure and the methane molecules are too strong, preventing any inter-cavity motion. In comparison using the, Tsuzuki-model alongside with the parameters in Table 6.4 for the zeolite structure, the mean square displacement is increasing linearly with time, meaning that the methane molecules exhibit a liquid like behavior, see Figure 7.2. The linear fit is quite good in molecular dynamic context, with a R^2=0.9931. The slope of the fitted line gives a diffusion coefficient $\sim 5.6\ {\cdot}10^{-9}\frac{m^2}{s}$, which is close to the reported values of García-Sánchez et al. [60]. This is also the highest calculated diffusion for the Tsuzuki-model, but due to the short runtime, it is not included in the following comparison with literature values.

7.1.2 Comparing LTA^{-96} and LTA$_{Si}$ for the Tsuzuki model

When the aluminium site is replaced with silicon the diffusion coefficient is $\sim 3.6\ {\cdot}10^{-9}\frac{m^2}{s}$, see Figure 7.3. This can be explain by the silicon site having a stronger repulsion at intermediate distance, due to a larger ρ parameter. The larger ρ gives a less step repulsion, compared to the aluminium site. When pure specie interactions are considered, the aluminium site only overtakes the silicon site, at a distance below ~1.8 Å due to the larger A parameter, see Table 6.4.

This simulation was done to check the model for the zeolite structure. García-Sánchez et al. [60] denoted the zeolite as LTA$_{Si}$, which from their explanation is a LTA-4A zeolite without counter-ions and aluminium replaced with silicon. The potential used for the LTA-4A zeolite, is based on the parameters in the work of Dubbeldam et al. [64], with the full potential given in Garcia-Sanchez et al. [65]. Dubbeldam et al. [64] used a Kiselev et al. [66] approach where all interactions are moved towards the oxygen atoms. The argument for such an approach is that the oxygen sites are sticking out into the ring, see Figure 3.1, and thus shields the other sites. The parameters in Garcia-Sanchez et al. [65] use the same Lennard-Jones for O_{Si} and O$_{Al}$, only differing in the charges at the sites. Charges on the structure have no influence on the non-polar OPLS methane sphere. So in reality the simulations have been performed on a zeolite A without counter-ions. This explains why the LTA^{-96} simulation gives a better result than the LTA$_{Si}$.

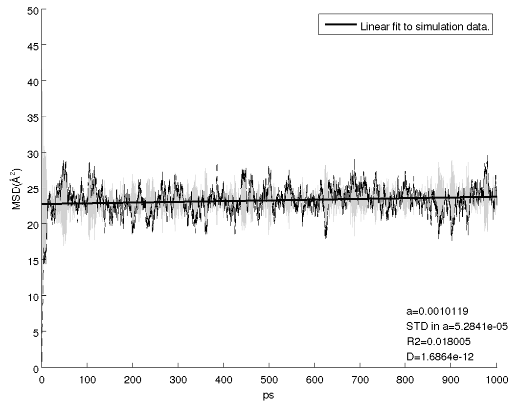

FIGURE 7.1: Mean square displacement using the OPLS model for methane in LTA^{-96}.

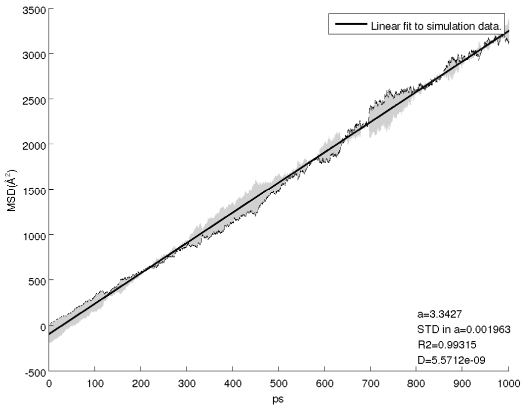

FIGURE 7.2: Mean square displacement using the Tsuzuki model for methane in LTA^{-96}.

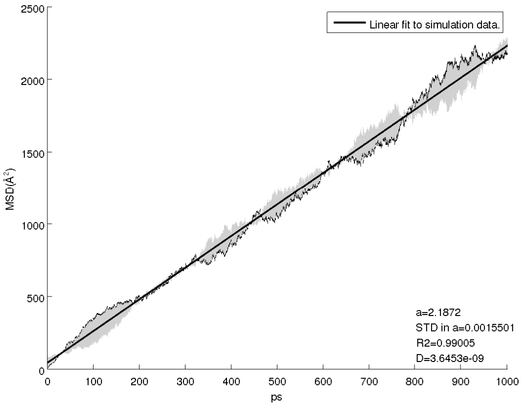

FIGURE 7.3: Mean square displacement using the Tsuzuki model for methane in LTA$_{Si}$.

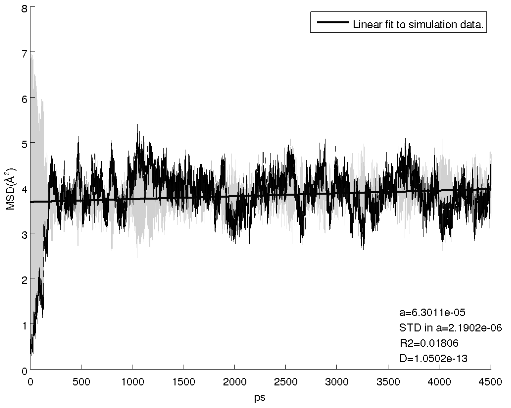

FIGURE 7.4: Mean square displacement using the Tsuzuki model for methane in LTA-3A.

Remarks for Figure 7.1 to 7.4: The shaded area is the residual from the fit of the linear line. The diffusion coefficient is given in all MSD plot in the right corner with units $\frac{m^2}{s}$. The slope and the standard deviation in the slope are given in units of $\frac{\mathring{A}^2}{s}$.

7.1.3 MSD for methane in LTA-3A

The mean square displacement in Figure 7.4, shows that the methane molecules are locked in positions ∼4 Å, from the starting positions, and inter-cavity motion is non-existing. This is in agreement with the steric exclusion of methane being the working method of zeolite KA in natural gas dehydration, and means that methane will move through the zeolite binder. It must be mentioned, that the simulation in itself, is a proof for the simulation setup to be highly unlikely. The simulation showed that the methane molecules are not able to move inside the zeolite crystal, thus they will not be able to enter it when the 8T-window is blocked. The next generation of simulations should thus focus on an interfacial system.

The temperature plot for the simulation of 66 methane molecules inside zeolite KA is shown in Figure 7.8, following after the discussion in Section 7.2. The partition of energy between rotational and vibrational degrees of freedom has clearly improved compared to the LTA^{-96} simulations, see Figure 7.5 to 7.7. This is due to the potassium ions blocking the 8T-window, in doing so, the methane molecules cannot pass through the energy barrier, and the energy is divided more evenly.

7.2 Runtime of the simulations

The calculated MSD plots for a loading ranging from 3 to 15 methane molecules per α-cavity, are given in Appendix C. The MSD from the simulation of 24 methane molecules shows a lot of noise indicating that the molecules are moving around the same position for long periods of time. To obtain a good diffusion measurement it would have been beneficial with a longer runtime. For this reason simulations with fewer molecules were not performed, as the computational time would not fit within the time limit of this thesis. The mean square displacement for the 40 methane system shows the typical ballistic behavior in the start of the simulation, before the random walk starts. With increasing particle numbers, the particles start the collisions earlier, and the ballistic behavior disappears from the plots, see Figure C.4 to C.12. These plots show a good linear fit with $R^2 \approx 0.99$. The exception is the 120 methane simulation, where the MSD, see Figure C.13, is static indicating that the methane molecules have taken a highly ordered arrangement inside the cavities. The loading of 15 methane molecules pr α-cavity occupies all the sites leaving no possibility for inter-cavity motion, this was also pointed out by Beerdsen et al. [67]. Figure 7.5 shows that the methane temperature has settled down within ±5 K of 500 K for the 24 methane simulation. This variation is natural around the observed value in the canonical ensemble. The system rotational and vibrational temperatures are separated with large fluctuations, this is typical for a system containing high energy barriers [25, p 98-99]. When one molecule passes through the energy barrier it will have a large influence on the temperature of the system, because the small number of molecules to average over. For this reason an equilibrium run of 1 ns was used for the two smallest systems, if possible even longer runs would have been performed, especially for the 24 methane system. The result from that simulation is not reliable, and should only be used as an indication to the magnitude of diffusion. The equipartition of energy improved with larger number of molecules, see Figure 7.5 to 7.7, because the energy barrier of the 8T window had less influence on the system. Thus, an equilibrium run of 500 ps was used for the 40 methane simulations and larger, this is the same equilibrium time as Sega et al. [68] used for water in a confined geometry. For all simulations the runtime has been weighted between the need for long production runs to obtain diffusion measurements, and the need for long equilibrium runs for the system to divide the energy evenly.

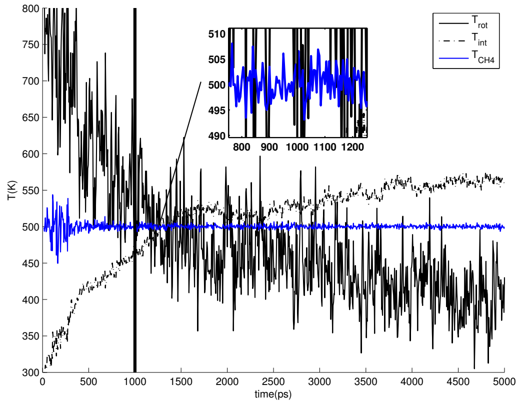

FIGURE 7.5: Temperature variations throughout the 5000 ps run of 24 methane molecules in LTA^{-96}.

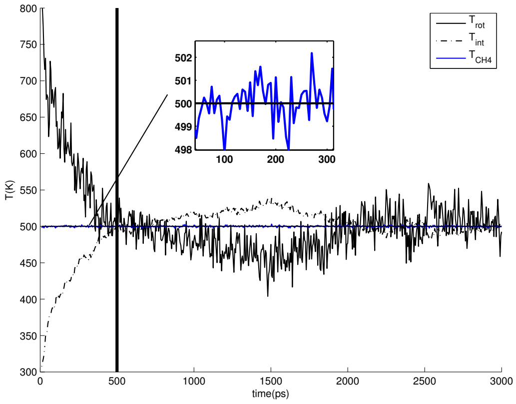

FIGURE 7.6: Temperature variations throughout the 2500 ps run of 64 methane molecules in LTA^{-96}.

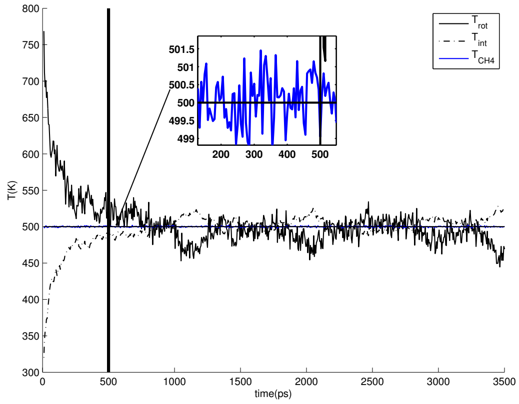

FIGURE 7.7: Temperature variations throughout the 3500 ps run of 120 methane molecules in LTA^{-96}.

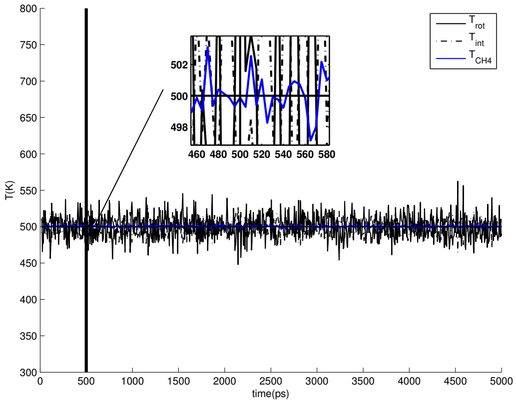

FIGURE 7.8: Temperature variations throughout the 5000 ps run of 66 methane molecules in LTA-3A.

Remarks for Figure 7.5 to 7.8: The vertical line is when production run was started. T_{CH4} is the methane temperature, T_{rot} is the rotational temperature of methane and T_{int} is the internal temperature of methane.

7.3 Comparing the Tsuzuki-model to literature values

Figure 7.9 shows the obtained diffusion for the thirteen simulations performed in zeolite A without counter-ions. The figure also shows the approximated values reported by García-Sánchez et al. [60], using the force field of Dubbeldam et al. [64]. The diffusion in this work, for LTA^{-96}, is highly dependent on loading, differing from the values of García-Sánchez et al. [60] with as much as $\sim 2 \cdot 10^{-9} \frac{m^2}{s}$ at a loading below 8 methane molecules/α-cavity. With a loading of 8 methane molecules/α-cavity or more the difference is small, the reason is the strong Arrhenius dependency in this work. The diffusion increases exponentially faster with loading, than the values reported by García-Sánchez et al. [60]. Both models show the highest diffusion with a loading of 9 methane molecules/α-cavity. With higher loading the diffusion decreases linearly as the sites becomes occupied. The initial increase in diffusion is due to the replacement of methane-zeolite interactions with methane-methane repulsion that pushes the methane molecules through the 8T-window. The decrease in diffusion is caused by the filling of sites in the cavities, leaving fewer sites for molecules moving between cavities.

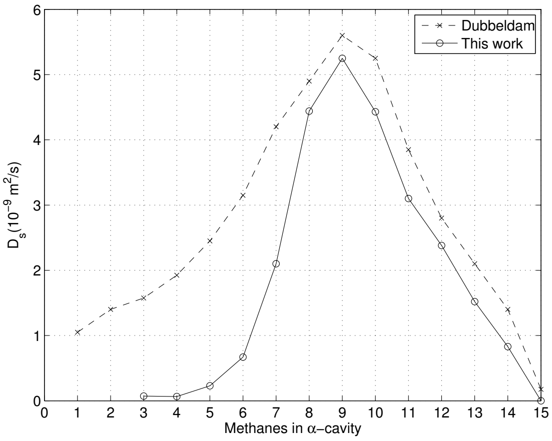

Figure 7.9: Diffusion of methane in LTA^{-96} as a function of loading. Compared to the values of García-Sánchez et al. [60], which used the force field of Dubbeldam et al. [64].

The force field in the original work of Dubbeldam et al. [64] was compared to experimental data for heat of adsorption and Henry coefficient with good agreement for alkanes in zeolite MFI. García-Sánchez et al. [60] also performed simulations with calcium, i.e. LTA-5A, using the same zeolite structure framework as for the counter-ion free simulations. The rigid framework was compared to two different flexible models, which he then compared to experimental data for methane in LTA-5A. García-Sánchez et al. [60] stated that for a single methane in LTA-5A the diffusion for one of the flexible models is in reasonable agreement with experimental data, while the other is underestimating the diffusion. The rigid model underestimated the diffusion at low loading, but with increasing loading the difference between the flexible and the rigid models are small.

The values in Figure 7.9 can also be compared to the reported values of Demontis and Suffritti [69]. This study investigated methane diffusion at a loading of 1, 3 and 6 methane molecules/α-cavity, in flexible zeolite NaA with different number of counter-ions. The reported values are $\sim 2.5 \cdot 10^{-9}\frac{m^2}{s}$,$\sim 3.1 \cdot 10^{-9}\frac{m^2}{s}$ and $\sim 4.6 \cdot 10^{-9}\frac{m^2}{s}$ respectively for the different methane loadings and the temperature in the simulation was close to 360 K. These values are higher than the values obtained in this work. The reason is the flexible framework, which has a larger influence on the diffusion when the loading is low, and the zeolite energy barrier for diffusion high. This energy barrier decreases with increasing loading, as pointed out in Beerdsen et al. [67], this explains why the difference in the obtained values are small at high loading. Demontis and Suffritti [69] compared the performance of the force field to experimental data on methane diffusion in zeolite ZK4 at low loading. The performed simulations underestimated the diffusion with two orders of magnitude. Furthermore, the values in this work can also be compared to the values reported by Dubbeldam et al. [70], which also used the force-field of Dubbeldam et al. [64]. These simulations were performed at 600 K and are just slightly higher than the values reported by García-Sánchez et al. [60]. It would therefore be interesting to see how the model in this work performs at different temperatures.

From the comparison with literature values it is clear that the model in this work underestimates the methane diffusion at low loading compared to published models. These models then again, underestimate the methane diffusion at low loading compared to experimental data. One can thus expect that the model in this work, will underestimate the diffusion at low loading, compared to experimental studies.

7.4 Comparing the structural results

7.4.1 Radial distribution functions

The radial distribution function for the simulations of methane in LTA^{-96}, see Table 6.6, alongside with the two simulations with 66 methane molecules in LTA^{-96} and LTA-3A, see Table 6.5, are given in Figure 7.10. The figure shows for all simulations, except the LTA-3A simulation, that the distance of exclusion is ∼3 Å. With increasing number of methane molecules, the probability of finding another methane at longer distances increases. Compared to the diffusion in Figure 7.9, the diffusion is highest when g(r) approaches the ideal system, beyond ∼6 Å. The diffusion decreases with the formation of a second shell, beyond 6 Å , this shell restricts the inter-cavity motion. The influence of the counter-ions, in the LTA-3A system, is shown by the exclusion distance of ∼2.6 Å. The compression of the methane molecules, are also observed with increasing methane numbers in LTA^{-96}, but not to such an extent. The radial distribution function for methane in LTA-3A shows a highly ordered structure, compared to the systems without counter-ions. The probability of finding a methane within the first shell is over twice that observed without counter-ions. The first peak is then followed by small oscillations, instead of the large exclusion seen in the LTA^{-96} simulations. The reason for this, is the counter-ions pushing the methane molecules together, reducing the free space of motion inside the α-cavity.

The methane-methane RDF can be compared to the work Kumar et al. [71] did on zeolite NaCaA. They found for a loading of one methane per α-cavity, an eminent peak at 4.1 Å. This can be compared to peak of the 24 methane simulation in LTA^{-96}, which is slightly shifted below 4 Å. The peak in this work is much broader and higher reflecting the higher temperature, 500K versus 150K, and the higher loading respectively. Furthermore, one can do a comparison to the work done by Demontis and Suffritti [72]. The simulations was done for methane in LTA$_{Si}$, at loadings of 1, 7 and 15 methane molecules/α-cavity. They found the first prominent peak ranging from 3.84 Å(1 molecule) to 3.70 Å(15 molecules), which is close to 3.65 Å observed for 15 methane molecules pr α-cavity is this work. They also reported that a well-defined second peak, starts to rise at about 6.5 Å, for loadings higher than 6 molecules/cavity. This is also observed in this work, for the 56 methane simulation to the 120 methane simulation. The peak falls approximately at 6.55Åfor the 104 methane simulation, and 6.35Åfor the 120 methane simulation. The peaks in this work is higher and narrower, than in the work of Demontis and Suffritti [72], which reflects the lower temperature of 357 K.

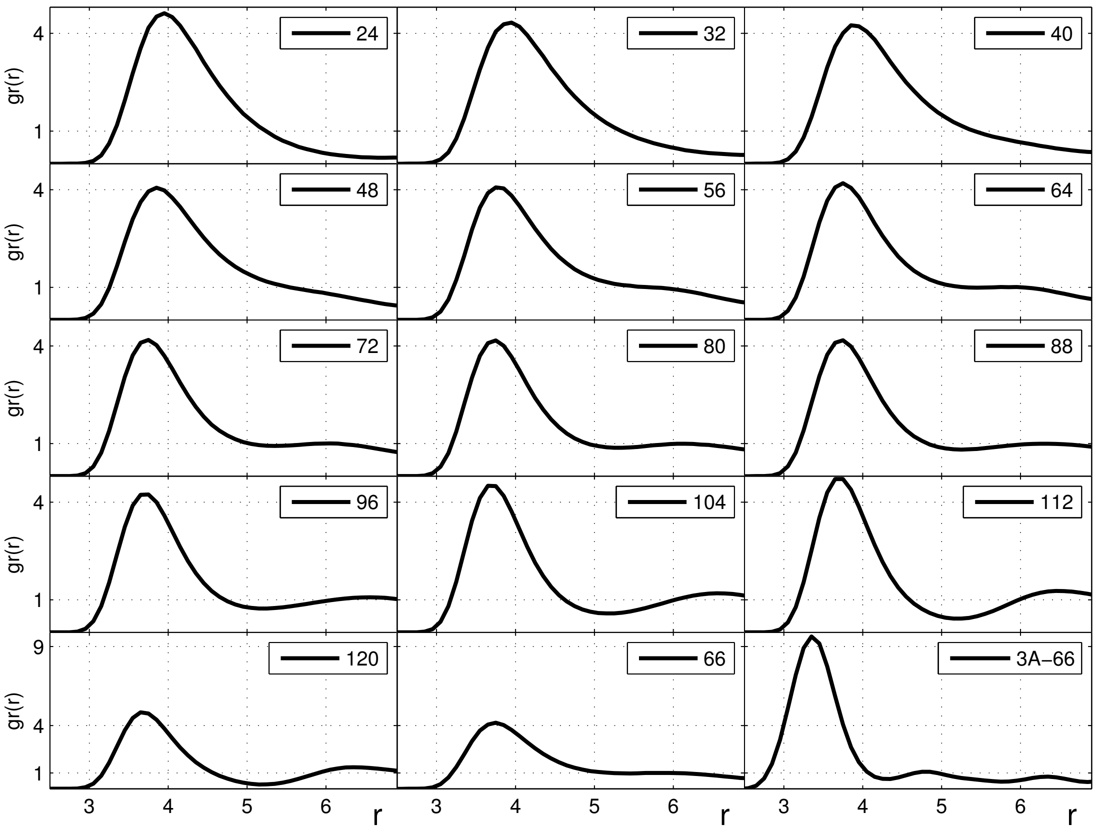

FIGURE 7.10: Radial distribution function for methane, center of mass- center of mass, in LTA-zeolite. The legends indicates the number of methane molecules in the simulation. Just numbers corresponds to LTA-zeolite without counter-ions i.e. LTA^{-96}, while the last graph with 3A-66 is with counter-ions i.e. LTA-3A zeolite. **Notice:** the y-axis in the three last plots goes to 9, instead of 4 in the above plots.

7.5 Density profiles and trajectories

7.5.1 LTA^{-96}

The density profiles, see Figure 7.11, show the pronounced effect increasing loading has on the methane zeolite system. The 24-methane system shows a concentrated density in the α-cavities, with large fluctuations. The fluctuations mean that the methane molecules are free to move inside the cavities, but the lack of density around the 8T-windows, show that they rarely move between the cavities. The peaks are more prominent in the systems with 48 and 72 methane molecules, where the formations of two more peaks at the 6T-windows are shown as well. The density has now stretched through the 8T-windows, with large fluctuations for the 72 methane system, reflecting that the molecules can move quite freely through the windows, compared to the less dense systems. The 96-methane system shows a small density peak on both sides of the 8T-window, while the other peaks are more prominent. This reflects that the methane molecules are starting to find a highly ordered structure inside the cavities.

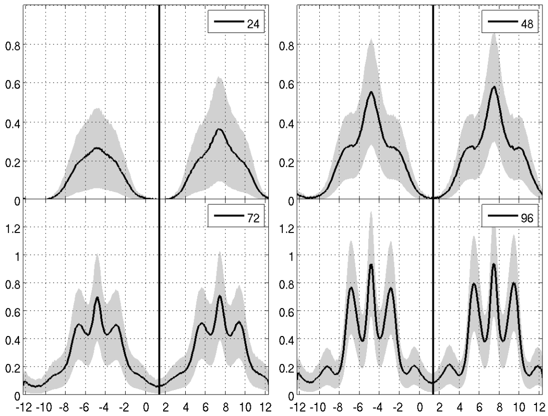

FIGURE 7.11: Density profiles in LTA^{-96} projected on to the z-axis, the shaded area shows the standard deviation. The legends show the number of methane molecules in the simulation, while the vertical solid line shows the position of the 8-window in the middle of the unit-cell. The second 8T-window is not marked but is at $\sim$ -11 Å, due to the periodic boundary conditions. The density-profiles have a resolution of 0.1 Å, and is averaged from t=1 ns to t=1.5 ns with a stepsize of 50 fs.

The density profile for the 120-methane system is shown in Figure 7.13, alongside with the trajectories for the methane molecules in Figure 7.14. Furthermore, the occupancy plot in Figure 7.12 display that there are six preferred sites for the methane molecules behind each of the 8T-windows, alongside with eight positions at the center of the 6T-windows displaced into the cavity. One more site is found in the middle of the cavity, so in total there are fifteen preferred positions in one α-cavity. The density profile is identical for all axes, indicating that the distribution is equal in all cavities. The static mean square displacement in Figure C.13 indicates that there are no available sites in the system. These results are in agreement with the results of Loriso et al. [73], Demontis and Suffritti [72] and Beerdsen et al. [67]. Loriso et al. [73] work was on rare gases, but they expected small molecules at high loading to exhibit an ordered structure, solid like, in zeolite A. Forming a distorted face-centered cube with a central atom, this was confirmed by the work Demontis and Suffritti [72] did on methane in zeolite ZK4, the all-silica analog to zeolite A.

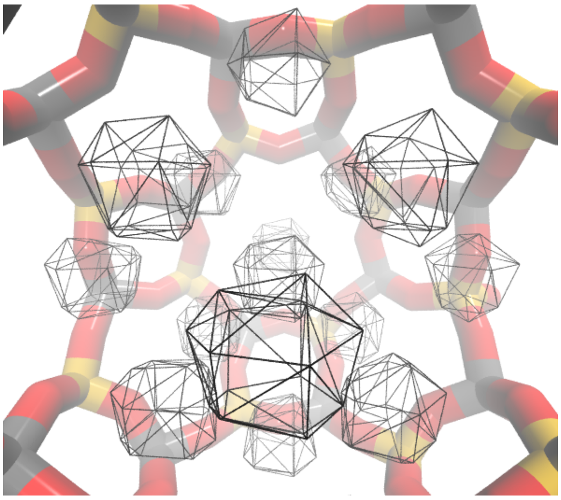

FIGURE 7.12: The figure looks through a 8T-window and shows with lines the space occupied by methane inside a α-cavity, averaged from t=1 ns to 1.3 ns step size 50 ps, and loading 15 methane molecules/cavity. The 8T-windows are only partially shown on each side.

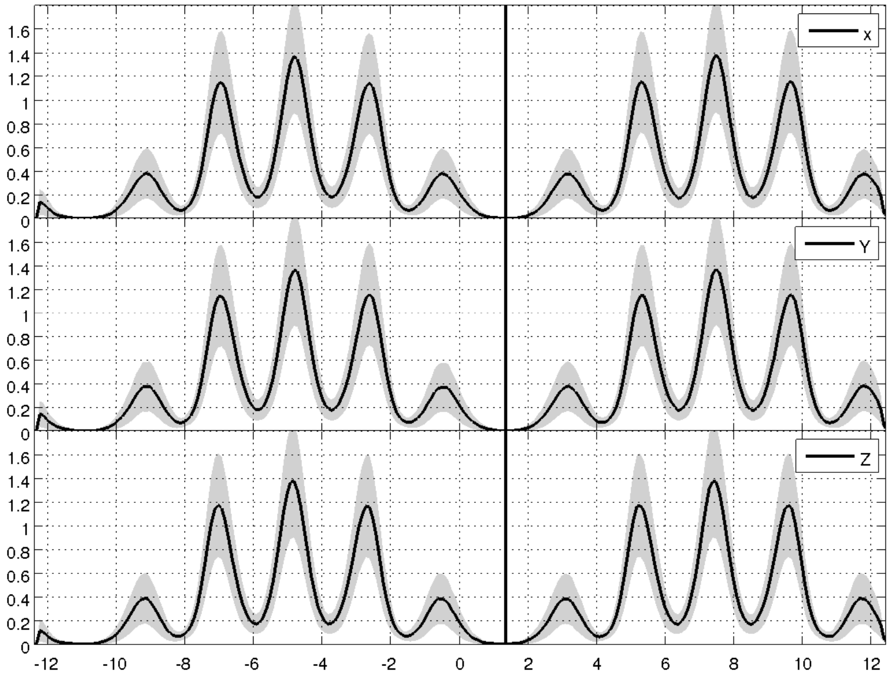

FIGURE 7.13: Density profiles for the 120 methane system in LTA^{-96}, the legends show the axis which the density is projected on to. The density-profile has a resolution of 0.1 Å, and is averaged from t=1 ns to t=1.5 ns with a stepsize of 50 fs.

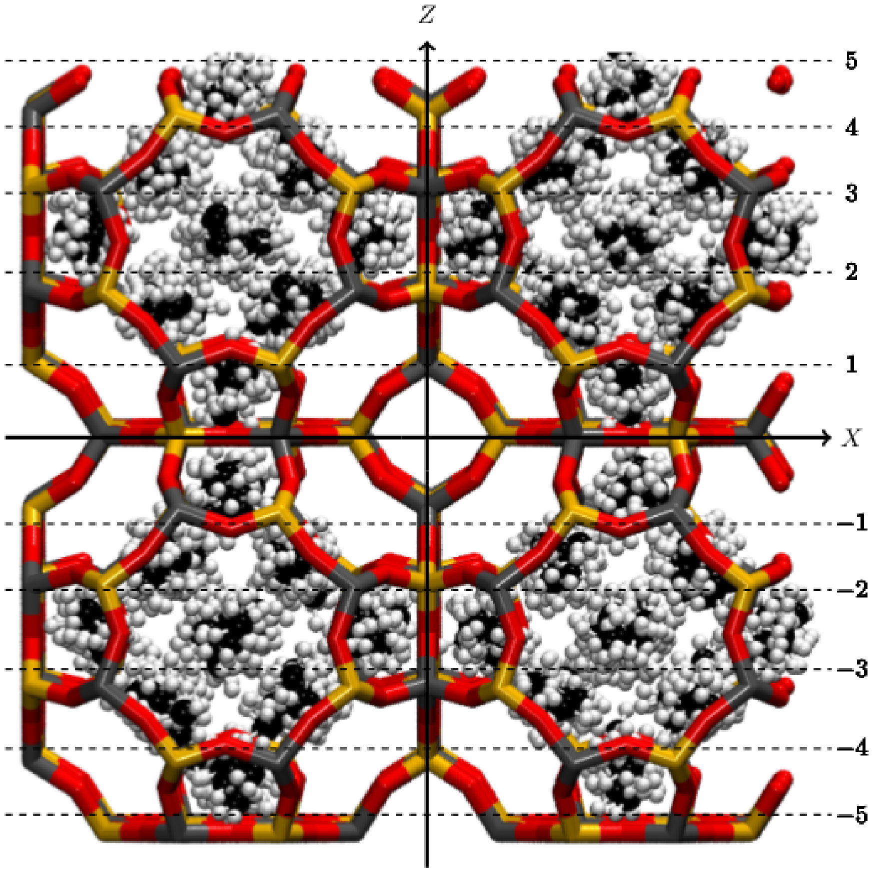

FIGURE 7.14: The figure shows the positions of 120 methane molecules from t=0.5 ns to t=1 ns with a step size of 50 ps. The dashed lines works as a guide to the eye in order to identify the density peaks in Figure 7.13.

7.5.2 LTA-3A

In one α-cavity there are fourteen preferred potassium sites, see Figure 3.2, these partially coincides with the fifteen methane sites. Consequently it was observed that at a most, two potassium ions were pushed into the β-cage, this is shown in Figure 7.15. The long trajectory, shown on the right hand side, into the β-cage is from the potassium ion interacting with the 9 methane molecules/α-cavity. While the short trajectory into the β-cage is from a potassium interacting with 8 methane/α-cavity. It was also observed that the other 9 methane cavity, lead to a long potassium trajectory into a β-cage. With two potassium ions located in the β-cage, the four remaining potassium ions are pushed out of 6T-window and slightly into the α-cavities, as shown in Figure 7.15. This lead again to a compression of the methane molecules in the α-cavity, shown in the lower left of the yx-plane, in Figure 7.16. This then drove the methane molecules in this cavity, to push out the potassium ion located in the 8T-window. The density profile, see Figure 7.16, projected onto the y-axis shows the resulting methane density peak in the 8T-window. In all the plane pictures it is clear that methane seeks the positions in front of the 6T-windows when possible, because the easiest option is to push the 6T-potassium ions into the β-cage, compared to a narrower 4T-window and a methane blocked 8T-window. This indicates how a defect in the zeolite KA can form. If sufficient numbers of 8T-windows are unblocked, the methane molecules will be able to move into the zeolite structure. In this case the residence time of methane in the zeolite pellet will be drastically changed, due to the revealed volume of the zeolite crystal. Furthermore, if methane has the possibility to move into the zeolite crystal, this will also change the residence time of water in the crystal. Altogether, this can lead to insufficient dehydration of the natural gas.

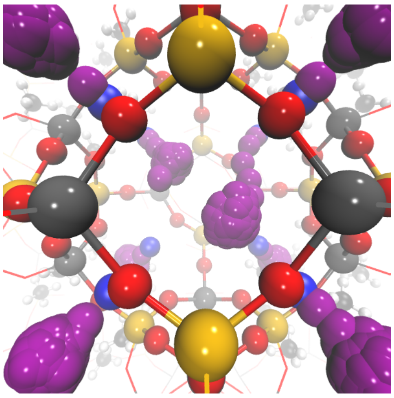

FIGURE 7.15: Trajectory for potassium, colored purple, in zeolite A. Plotted from T=0 to T=50 ps and step size 50 fs, the initial position is shown in blue.

Despite of the chicken and egg dilemma the simulation setup poses, see Section 7.1.3, the importance of the unblocking means this needs to be further investigated.

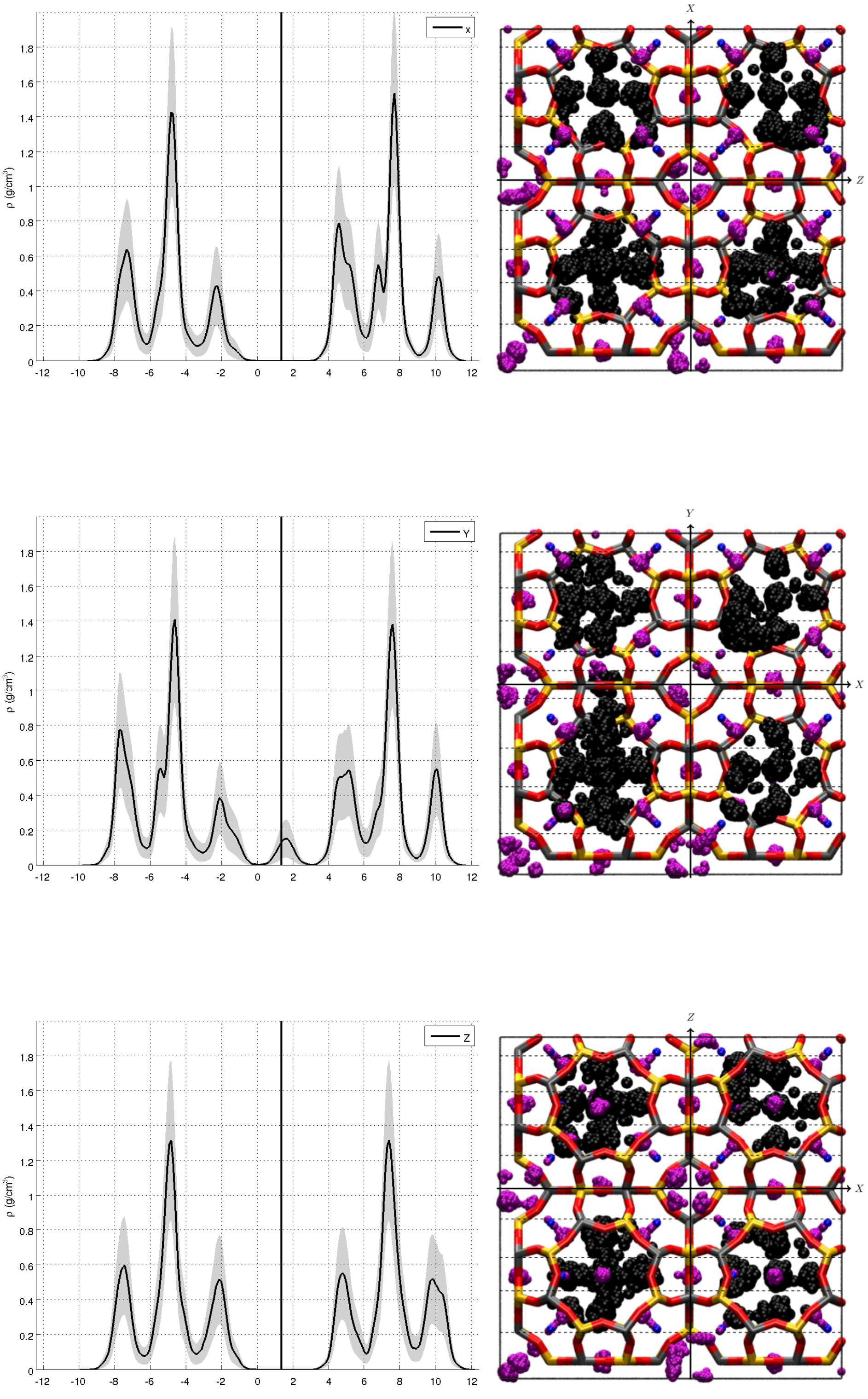

FIGURE 7.16: The density profiles for methane in LTA-3A are shown on the left side, while the figures on the right side show the trajectories from t=0 ps to t=1000 ps with a step size of 10 ps. The methane molecules are colored black, and potassium ions purple. The initial positions of the potassium ions are shown in blue. Only the general behavior is shown in the right hand side figures, some details are missing due to overlapping trajectories from the dimension not shown.

7.6 Potassium motion

7.6.1 Simulation observations

The 6T-rings are in the first 500 fs of the simulation unblocked, due to potassium ions moving into the β-cage under the influence of methane. With these sites open, and as the simulation progressed, the methane molecules gradually pushed a potassium ion in the 8T-ring out of its position. This potassium then moved to the position at the 6T-ring, leaving the 8T-ring open. This happened 530 ps out in the simulation, and is shown in Figure 7.17. This was the only episode of potassium leaving the 8T-window in the 5 ns simulation. The methane molecule that moved into the 8T-ring was kept from moving into the next α-cavity, by the methane molecules residing to this cavity due to the potassium ions still blocking the five surrounding windows. Furthermore, it was observed that a potassium ion initially located behind the 4T-window moved to a vacant spot at the 6T-window, this is shown in Figure 7.18 and happened 50 ps out in the simulation.

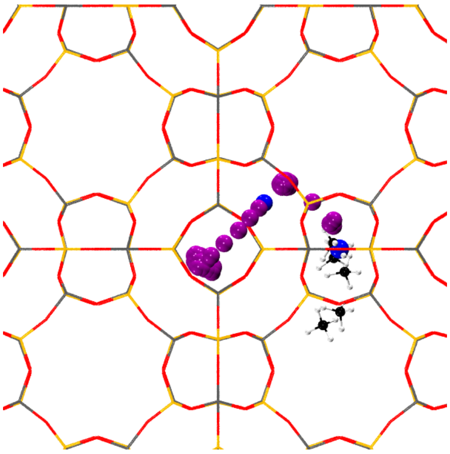

FIGURE 7.17: Correlated motion between 8T and 6T potassium ions

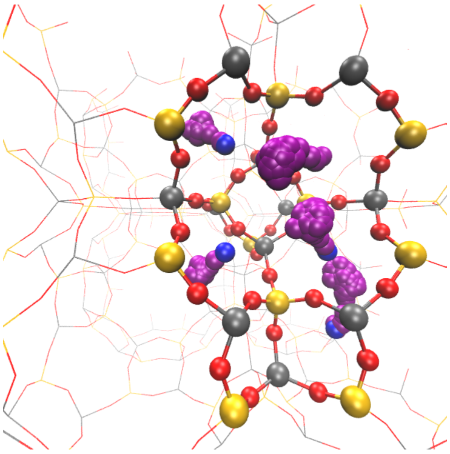

FIGURE 7.18: Correlated motion between 4T and 6T potassium ions

Remarks for Figure 7.17 and Figure 7.18: The initial positions for the potassium ions are colored blue, while the trajectories are purple. The other molecules are left out for easier visualization. Different step sizes have been used for Figure 7.17 to avoid overlapping trajectories, while Figure 7.18 is plotted every 50 fs.

7.6.2 Validating the observations

The high cationic motion observed in the simulation seems physical, when compared to experiments and molecular dynamics simulations. Lim and Grey [74] found experimentally considerable counter-ion motion in zeolite NaY and zeolite NaX, especially for dehydrated samples. Consequently, it was discovered four sites for the hydrated sample and five sites for the dehydrated sample, Lim and Grey [74] explained this by water stabilizing the sites. The water stabilization of zeolites was also pointed out in the book of Dyer [9]. The jump of a potassium ion into the β-cage and the correlated motion of a potassium located at the 4T window towards the empty 6T-window has been experimentally proven by Schoonheydt, R. A. [75], who investigated zeolite X and zeolite Y. Schoonheydt, R. A. [75] stated that for these zeolites, this trend could only be shown to exist at temperatures above 400 K. The same trend has been observed by researchers who used molecular dynamics Gren et al. [76]; with the authors investigating water-zeolite NaA interface at 300 K. Pluth and Smith [77] found experimentally low occupancy of potassium in the β-cage of the dehydrated zeolite KA. Zeolite simulations performed in this work have thus, pinpointed yet another fascinating phenomenon, the correlation between a potassium located at the 6T-ring moving into the β-cage, and potassium ion located at the 8T-ring taking the vacated spot. Both the existence of potassium in the β-cages, and the correlated motion between the 4T potassium ions and the 6T potassium ions have been proven experimentally at high temperatures. Furthermore, water stabilization of the sites has been shown experimentally to have an important role in determining the number of available counter-ion sites in the zeolite crystal. This leads us to formulate the following conjectures:

Hypothesis. *A critical dehydration of the zeolite crystals, caused by an excessively high regeneration temperature during desorption, can be an important reason behind the drastically reduced lifetime of the zeolites, due to the changes caused by the unblocking of the 8T-windows.*

7.7 Polynomial path integration for water

The polynomial path integration was performed for water in zeolite, to investigate the possibility of obtaining a measurement for excess Helmholtz free energy. All the simulations are summarized in table 6.7. The work was started from trying the K_1 exponents 2, 3 and 4, for a simulation time of 50 ps. The resulting integrands, $\left\langle \frac{\partial U}{\partial \lambda} \right\rangle_\lambda$, are plotted in Figure 7.20 with the excess Helmholtz free energy given in Table 7.1. Velocity scaling was used to control the temperature. This did not give any large difference in the calculated values compared to the use of a Nosé-Hoover thermostat for a short runtime of 50 ps, see Figure 7.20. The obtained excess energy of velocity scaling was only 13.25 ppm smaller than the value obtained with the Nosé-Hoover thermostat.

This can be explained by velocity scaling being able to approximate the canonical distribution in configurational space. Although the lack of canonical distribution in momentum space, can yield different values for the potential energy, as pointed out by Kuznetsova and Kvamme [43]. Hence, large deviation in the excess energy is possible for longer runs. Nonetheless, for comparative purposes, with the limited time in this thesis, the 50 ps runs can cast light on the use of different exponents. From Figure 7.20 one can see an increase in the integrand curvature, when the K_1 exponent is changed from 2 to 4. This means that the creation of real particles is confined to specific intervals of the coupling parameter, instead of spreading out over the whole interval when the curvature is reduced. This indicates that the exponent, $K_1=1$, could perform better. This was investigated, but the simulation ran into the classical problem of reducing the repulsion too fast, leading to too high electrostatic interaction at $\lambda=0.1125$. This consequently crashed the simulation after 6.3 ps. The reason was an abnormal stretch of the O-H bonds in the water molecules, see Figure 7.19, it was thus not an option to use the exponent K_1. The exponent $K_1=2$, in spite of the large error ±18.27 kJ/mol at $\lambda=0.1125$, gave the best distribution of real particle creation over the set of λ-values. Furthermore, the exponents $K_1=2$,

FIGURE 7.19: Abnormal bond stretching in water caused by scaling the repulsive part of the potential faster then the electrostatic part. The length of the stretched bond is ~6 Å, while the equilibrium O-H bond length in SPC water is 1 Å.

K_6=3, K_{12}=4 and K_{exp}=0.25 was the set that gave the best results in the work of Kuznetsova and Kvamme [43]. Mezei [42] obtained good results with K_1=2, K_6=2 and K_{12}=4 for SPC water, the exponential coupling function was later introduced by Kuznetsova and Kvamme [43].

Thus, the investigation continued into varying the K_6 and K_{12} exponents using the long runtime of 2 ns. At the same time the short runtime of 50 ps was checked against the long runtime. The longer runtime reduced the error in the calculation, showing that the 50 ps run was not long enough to properly equilibrate the system. Nonetheless, the 50 ps runs give an indication to how the water zeolite system will behave when the electrostatic is scaled, as it was intended to. In the 50 ps simulations there were large variation in the excess Helmholtz free energy, see in Table 7.1 and the curves of Figure 7.20. These variations are even more prominent for the scaling of the repulsive and attractive parts of the Lennard-Jones potential. The set of exponents that Mezei [42] used for pure SPC water, gave a convex curve for SPC water in zeolite resulting in an excess Helmholtz free energy of -66.70 kJ/mol, almost twice the value obtained from the next set of exponents, which was the one used by Kuznetsova and Kvamme [43]. The set of exponents K_1=2, K_6=2, K_{12}=3 and K_{exp}=0.25 gave an even creation of real particles over the λ-range, in spite of this, one has to consider the inconsistency in the obtained values from different sets of exponents. Both Kuznetsova and Kvamme [43] and Mezei [42], disregardless of the exponents used, obtained consistent results for the excess Helmholtz free energy. This can be explained by the Helmholtz free energy being a state variable, and thus independent for the path towards real particles. This was not observed over the different exponents tried in this work.

Table 7.1: The obtained values from integrating over λ in Figure 7.20. The exponents not given are constant, K_6=3, K_{12}=4 and $K_{exp} = 0.25$.

K_1	A_{excess} $(\frac{kJ}{mol})$	Error $(\frac{kJ}{mol})$
2	-37.48	±7.28
3	-15.10	±2.34
4	-5.10	±2.98

Table 7.2: The obtained values from integrating over λ in Figure 7.21. The exponents not given are constant, K_1=2, and $K_{exp} = 0.25$.

K_6	K_{12}	A_{excess} $(\frac{kJ}{mol})$	Error $(\frac{kJ}{mol})$
2	3	-20.53	±0.93
2	4	-66.70	±1.43
3	4	-38.76	±1.21
4	4	-33.25	±1.31

The reason for this failure can be too short simulation time leading to improper equilibration or the lack of ergodicity in momentum space due to the use of velocity scaling. Velocity scaling does not seem to be the influencing factor, as the Nosé-Hoover simulation is almost identical to the same velocity scaled simulation, see Figure 7.20, with just 13.55 ppm smaller excess energy. The effect of improper equilibration gives at the most 9.77 kJ/mol difference, between the 50 ps run and the 2 ns run, and as such can be a contributing factor. But the average energy of the simulations, have settled close to each other differing only 1.28 kJ/mol.

The large variation of interactions in the multi-specie system seems to be the influencing factor. Kuznetsova and Kvamme [43] and Mezei [42] did their work on pure bulk systems, thus the number of unique configurations is smaller than for a water-zeolite system. From the simulations performed, it is clear that the configuration space mapped in a water-zeolite system is dependent on the scaling of λ, due to the different forces and also the zeolite structure itself. Different scaling, will thus give different configurations of water, depending on what part of the structure is reachable with a given scaling of λ. In the long time limit one should expect all configurations to be mapped, but this looks to be computational difficult within reasonable time.

That said, longer simulations using the Nosé -Hoover thermostat would have been beneficial for a proper conclusion on polynomial path integration for water in zeolite. This would take a large amount of time, and there are many aspects to consider before running the λ-scaling in a Nosè-Hoover thermostated system. The Nosè-Hoover algorithm is more sensitive to non-physical changes, the system must thus be tuned with more care than a velocity scaled system. Taking into account that even a velocity scaled system broke down in this work, it could be beneficial to look into other methods to obtain excess energy. For example the particle insertion method, although this probably will lead to a low acceptance rate due to the restriction posed by the zeolite.

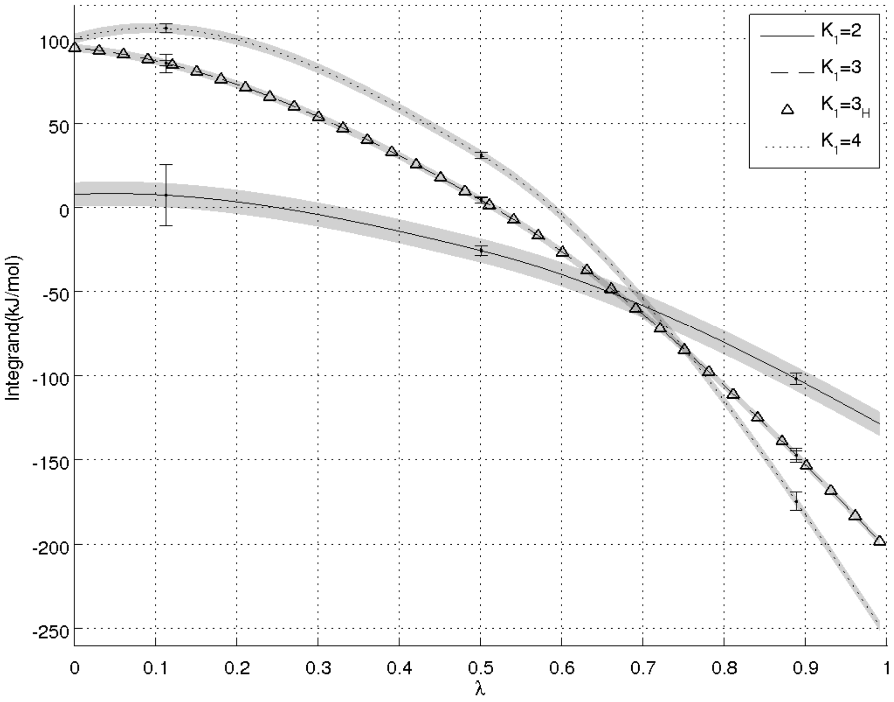

FIGURE 7.20: Polynomial path integration for 50 ps simulation of water in zeolite KA water, the errorbars show the error at each lambda value, while the shaded area is the resulting error in the overall integration. The legends show the different exponents while K_6=3, K_{12}=4 and $K_{exp} = 0.25$. The simulation using the Nosé-Hoover thermostat is, $K_1 = 3_H$.

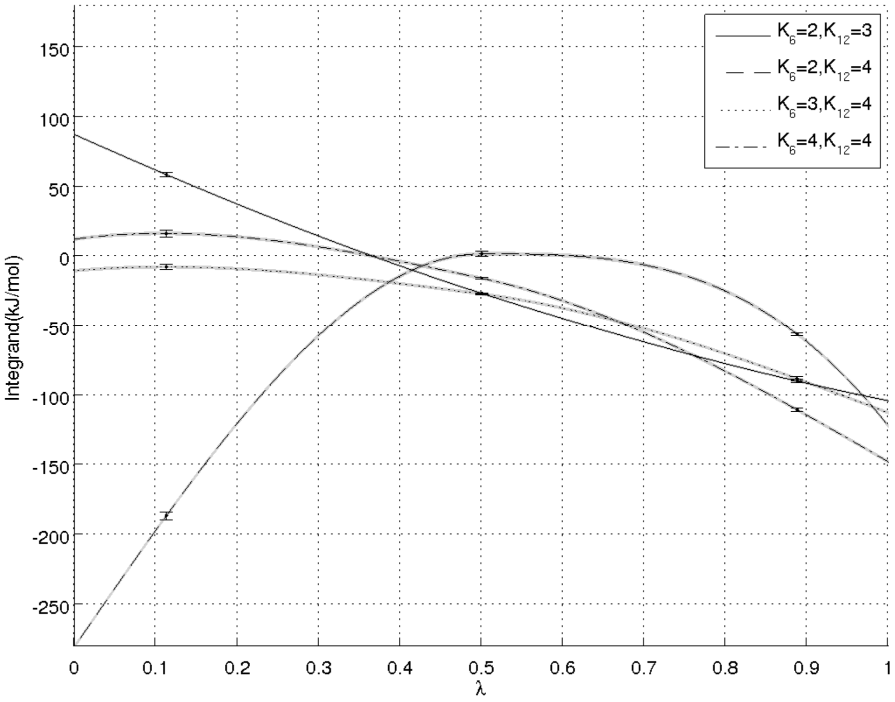

FIGURE 7.21: Polynomial path integration for 2 ns simulation of water in zeolite KA, the errorbars show the error at each lambda value, while the shaded area is the resulting error in the overall integration. The legends show the different exponents, while K_1=2, and $K_{exp} = 0.25$.

Chapter 8

Conclusions

8.1 Models for methane-zeolite interactions

The OPLS methane model[51] combined with the zeolite structure model of Faux et al. [16] using the Lorentz-Berthelot mixing-rules has been used to model 66 methane molecule in zeolite A without counter-ions. This system is based on the Lennard-Jones potential and simulations results have been compared to a new developed model. The new model is based on the Buckingham potential, where the zeolite structure is described by the 2-body model of Jackson and Catlow [48], the methane molecules are described by the model II of Tsuzuki et al. [54], and the two models are combined using the mixing-rules of Good and Hope [35]. Results from the simulations show that methane diffusion using the Buckingham based model is over three orders of magnitude higher than for the Lennard-Jones based model.

The performance of the new model has been further investigated by comparing the calculated methane diffusion coefficients to literature values for methane in counter-ion free zeolite A. These values show excellent agreement at loadings of 8 molecules per α-cavity or more. The diffusion coefficient at lower loading shows that the interactions towards the zeolite framework are still too strong. It is thus expected, that the model will underestimate the diffusion of methane at low loading, compared to experimental studies, although not as much as the earlier used model. The structural features using the new model have been compared to results from published molecular dynamics simulations. These show good agreement for the calculated methane radial distribution function, although the higher temperature broadens the peaks this work. The calculated density profiles and mean square displacement for the highest loading of 15 methane/α-cavity shows that methane exhibits a highly ordered, solid-like, structure inside the α-cavities. This is also in agreement with published molecular dynamics simulations on similar systems. The conclusion is that the new Buckingham based model performs well against other models frequently used in molecular dynamics simulations of methane in zeolites. Furthermore, it represents a better alternative than the earlier used Lennard-Jones based model, which has to strong methane-zeolite interactions.

8.2 Simulation of LTA3-A zeolite

The performed simulations of methane in LTA-3A zeolite, using the Buckingham potential at a temperature of 500 K, show that the presence of potassium ions prevents methane from moving inside the zeolite crystal. Methane is thus only allowed to move through the zeolite binder. This is in agreement with steric exclusion of methane being the working method of zeolite KA in natural gas dehydration.

8.2.1 Potassium motion

The simulation gave some interesting observations with regards to the potassium motion in zeolite A. Though, it must be pointed out that the results of the simulation were influenced by the nonphysical high concentrations of methane in the zeolite. Nonetheless, many of the same observations have been done experimentally by Lim and Grey [74], Pluth and Smith [77] and Schoonheydt, R. A. [75] and through molecular dynamic simulations of water and zeolite NaA, as reported by Gren et al. [76]. Zeolite simulations performed in this work have thus, pinpointed yet another fascinating phenomenon, the correlation between a potassium located at the 6T-ring moving into the β-cage, and the potassium ion located at the 8T-ring taking the vacated spot. Both the existence of potassium in the β-cages, and the correlated motion between the 4T potassium ions and the 6T potassium ions have been proven experimentally at high temperatures. Furthermore, water stabilization of the sites have been shown experimentally to have an important role in determining the number of available counter-ion sites in the zeolite crystal. This leads us to formulate the following conjectures:

Hypothesis. *A critical dehydration of the zeolite crystals, caused by an excessively high regeneration temperature during desorption, can be an important reason behind the drastically reduced lifetime of the zeolites, due to the changes caused by the unblocking of the 8T-windows.*

8.3 Investigation of polynomial path integration for water in zeolite

The work done on the polynomial path integration for water revealed that different paths from ideal gas towards real gas gave large differences in the estimated excess Helmholtz free energy. The main reason is configuration space mapped in a water-zeolite system being dependent on the scaling of λ. The polynomial path integration for water, was computational difficult to perform, due to the different forces in the multi-specie system and the zeolite confinements. Taking into account that even a velocity scaled system broke down in this work, it could be beneficial to look into other methods to obtain excess energy, for example insertion-based schemes, or other reference states which are more similar to the water in zeolite system.

Chapter 9

Suggestions for further work

9.1 Simulations

The simulations of methane in LTA^{-96} should be performed over a larger range of temperatures, in order to investigate the influence temperature has on the system. This will also give a better foundation for comparison to published work on the same system. Further tuning of simulation parameters and setup can reduce the computational time and improve the results, one could start with looking at the time steps and the relaxation time. The smaller LTA^{-96} systems need a longer runtime, probably in the order of 8 to 10 ns for the temperature fluctuations to settle down.

Further investigation on methane and LTA-3A zeolite is suggested to examine a methane-zeolite interface system. This should provide more reliable information to confirm or dismiss the proposed hypothesis. Although, it would take some work to set-up the zeolite structure as an interface system. Some information on this could be extracted from the interface work done by Combariza and Sastre [78] and Gren et al. [76]. The zeolite structure itself should preferentially be modelled with different levels of hydration to cover the water stabilization effect on the counter-ions. The observed potassium motion can also be investigated in a bulk water-zeolite system, with different levels of hydration and increasing temperature, to see if the same opening of the 8T-window can be observed.

The particle insertion method could be tried in instead of the polynomial path integration, although long simulation runs would be needed due to the restriction posed by the zeolite leading to a low acceptance rate for insertion of a particle.

The investigation could also continue into the use of a different reference state for water in zeolite, for example an Einstein crystal.

9.2 Improving the models

A further investigation of the methane model could look at how model III from Tsuzuki et al. [54] performs in a zeolite system. This model uses partial charges on methane, which accounts for polarization. This could then be compared to the model II used in this work, furthermore, different mixing-rules could also be applied. Implementation of the flexible zeolite model of [48] can also improve the calculations, although this would mean adding support for bond over periodic images. The use of a flexible model can improve the diffusion at low loading. Although, it should be mentioned that the use of flexible models is one of the large topics in molecular dynamics simulations of zeolites. On one hand some research groups argue that a flexible model is inaccurate, and that it is thus better to use the fixed equilibrium positions, on the other hand research groups argue that the flexible models are accurate enough and crucial for diffusion studies. The reader is referred to García-Sánchez et al. [60] and Demontis and Suffritti [79] for an introduction to the different points of view.

9.3 Changes to software

The problems with the calculation of translation temperature and pressure in the current MD51 code can be solved by implementing a flexible model. The program will then treat the zeolite structure as one molecule. This will remove the averaging over fixed molecules in the temperature calculation and the removal of non-bonded interactions between sites in the zeolite structure will produce correct pressure calculations. For continued use of a rigid framework the implementation of separate translation averaging and separate pressure calculation for each of the species would remove the current deficiencies in the code. Another option would be to try the DLPOLY code by Todorov et al. [80], this code has a better support for molecular dynamics simulations of zeolites. Although this would mean losing some of the features included in MD51 code.

Appendix A

The script for Figure 4.6

```
%script for visualizing difference between LJ12-6 and Buckingham potentials
r=1:0.001:10;
r0=0:0.0001:10;
rB=1:0.001:10;
%buck
eps=8;      % increased well depth for visualization
rm=2;
C=8.8;      %decreased value for visualization, of max UBuck
            % 12 gives same attractive part as LJ
Buck=eps*((6/(C-6))*exp(C*(1-rB./rm))...
-(C/(C-6))*((rm./rB).^6)); %Buckingham potential

LJ=eps*((rm./r).^12-2.*(rm./r).^6);  %Lennard Jones potential



%Make the plot look nice
TB=transpose(Buck);
[maxvalue,idx]=max(TB,[],1); % find top of Buckingham
LJ0=0./r0;
L=transpose(LJ);
[minlj,lj]=min(L,[],1);
hold on
plot(rB(1,1:2950),Buck(1,1:2950),r(1,1:2950),LJ(1,1:2950),'LineWidth',2);
legend('Buckingham','Lennard-Jones')
```

```
axis([0 4 -9 maxvalue+1])

h2=arrow([rB(1,102) Buck(1,102)],[rB(1,101) Buck(1,101)],'Length',6,...
'BaseAngle',60)
set(h2,'FaceColor',[0 0 0]);
h3=arrow([r(1,621) LJ(1,621)],[r(1,620) LJ(1,620)],'Length',6,...
'BaseAngle',60)
set(h3,'FaceColor',[0 0 0]);
h4=arrow([r(1,3000) LJ(1,3000)],[r(1,3002) LJ(1,3001)],'Length',24,...
'BaseAngle',60)
idL=crossing(LJ);
idF=crossing(TB(idx:8000));
set(h4,'FaceColor',[0 0 0]);
grid on
set(gca,'YTickLabel',[],'XTickLabel',[])
grid on   %put on ticks
[hx,hy]=ticks(gca,{'$0$','$\lambda r$','$_{\sigma_{B}}$',...
            '$\phantom{aa}_{\sigma_{LJ}}$','$_{r_{m}}$'},...
   {'$-\epsilon$','$0$','$U_{Buck}$'},...
           [0,rB(1,idx),rB(1,idx+idF),rB(1,idL),rm],...
           [-eps,0,maxvalue],[],[0],[],...
'FontSize',16,'FontWeight','Bold');
%labels
hy=ylabel('Energy','fontsize',18,'fontweight','b');
h=xlabel('r_{ij}','fontsize',18,'fontweight','b');

pos = get(h,'pos'); % Read position [x y z]
set(h,'pos',pos+[2 0 0]) % Move label to right
pos2 = get(hy,'pos'); % Read position [x y z]
set(hy,'pos',pos2+[0 0.2 0]) % Move label to right
hold off
```

Appendix B

The script for analysing MSD

```
file=’3A.dat’; %Set file name
U=load(file);
t=50*10^-15; %time step
x=U(:,1);    %load frames
y=(U(:,2)).^2; %msd from rmsd
scale=10^(12); % use ps
n=length(x);
xt=x.*t*scale; %x-axis in ps
P=polyfitn(xt,y,1); %Fit a linear line
yfit=polyvaln(P,xt); %creat the fittet line
b=y-yfit; %get the residual
D=(P.Coefficients(1,1)/(6))*10^-20*scale %calc diffusion from the slope(m^2/s)


xlabel(’ps’);
ylabel(’MSD(\AA^2)’);
hold on
xlim([0 xt(n,1)]);
plot(xt,yfit,’k’,’LineWidth’,2)
[hl, hp] = boundedline(xt,yfit,b,’alpha’);
plot(xt,yfit,’-k’,xt,y,’--k’,’MarkerSize’,0.001)
legend(’Linear fit to simulation data.’ );

txstr(1)={[’a=’,num2str(P.Coefficients(1,1))]};  %print slope (angstrom ^2/ps)
```

```
txstr(2)={['STD in a=',num2str(P.ParameterStd(1,1))]};%std (angstrom ^2/ps)
txstr(3)={['R2=',num2str(P.R2(1,1))]};        %print r squared
txstr(4)={['D=',num2str(D(1,1))]}; % print diffusion  (m^2/s)
text('units','normalized','pos',[0.80 0.10],'string'...
,txstr,'HorizontalAlignment','left');
hold off
```

Appendix C

MSD for methane in LTA^{-96}

Mean square displacement plots for methane in LTA^{-96}, ranging from a loading of 24 methane molecules to 120 methane molecules pr unit-cell follows below. The shaded area in the Figures are the residual from the fit of the linear line. The diffusion coefficient is given in all MSD for plots in the right corner with units $\frac{m^2}{s}$. The slope and the standard deviation in the slope are given in units of $\frac{\mathring{A}^2}{ps}$.

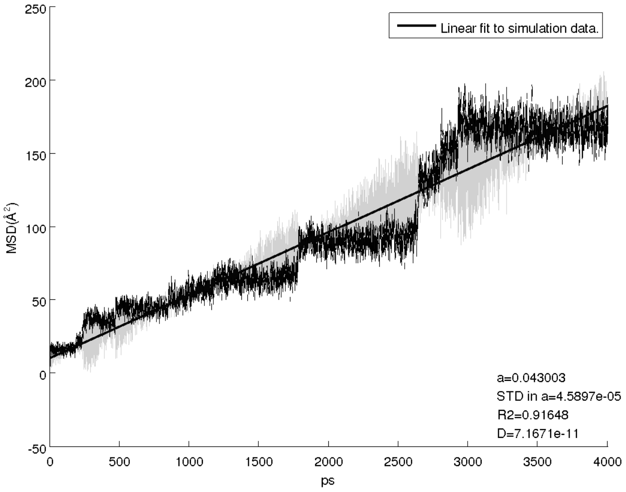

Figure C.1: MSD for 24 methane molecules.

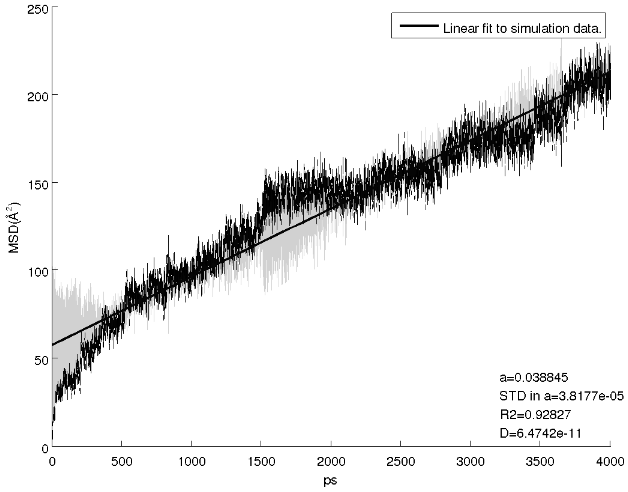

FIGURE C.2: MSD for 32 methane molecules.

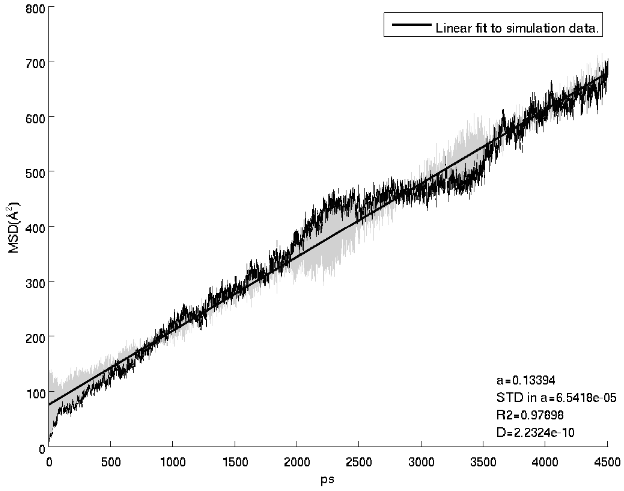

FIGURE C.3: MSD for 40 methane molecules.

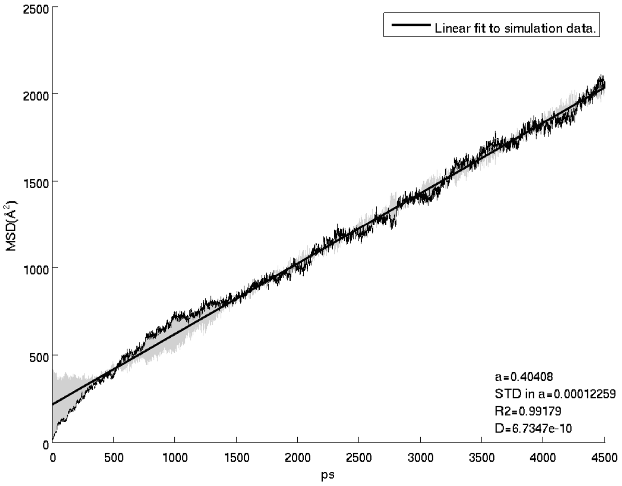

FIGURE C.4: MSD for 48 methane molecules.

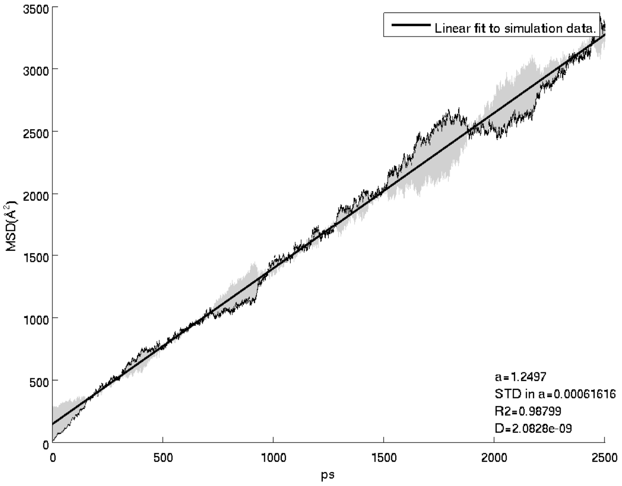

FIGURE C.5: MSD for 56 methane molecules.

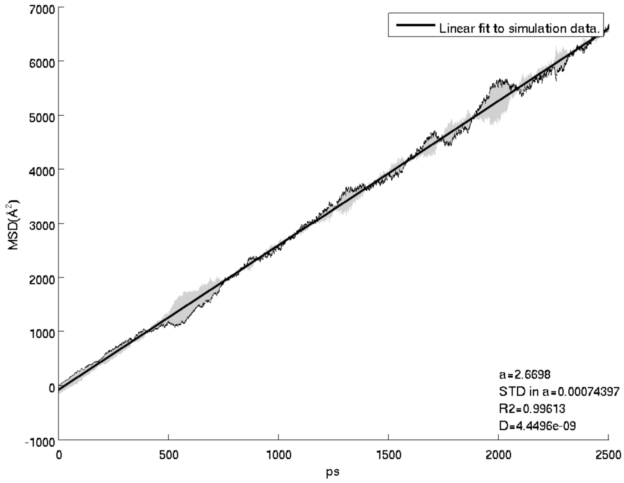

Figure C.6: MSD for 64 methane molecules.

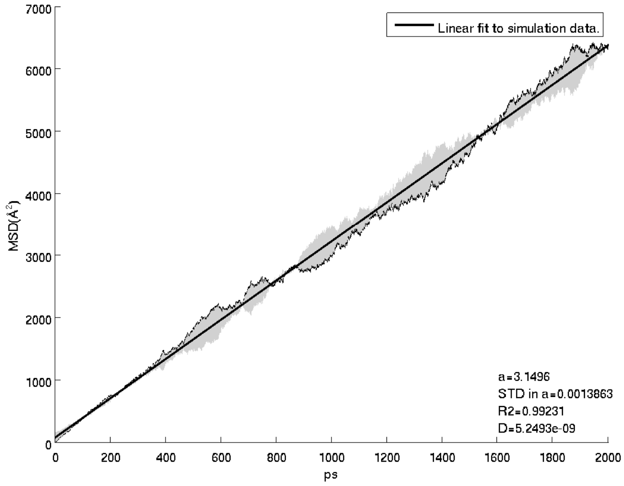

Figure C.7: MSD for 72 methane molecules.

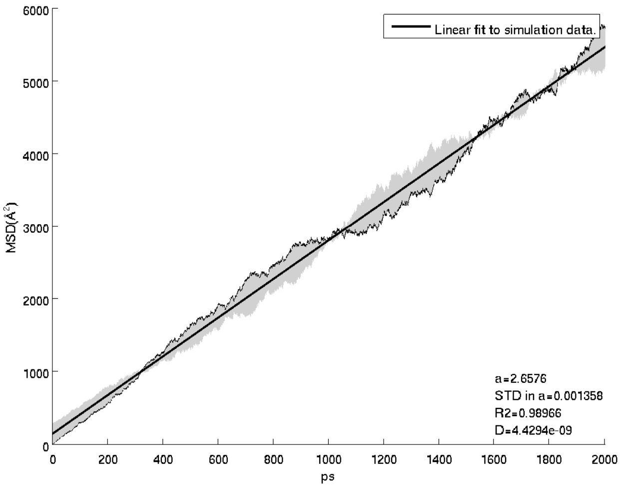

Figure C.8: MSD for 80 methane molecules.

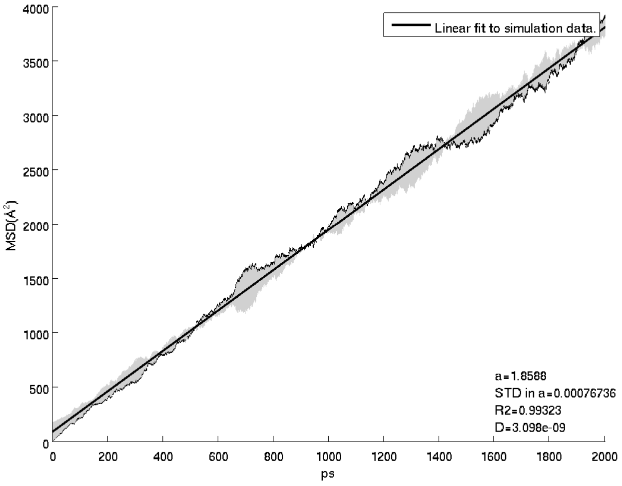

Figure C.9: MSD for 88 methane molecules.

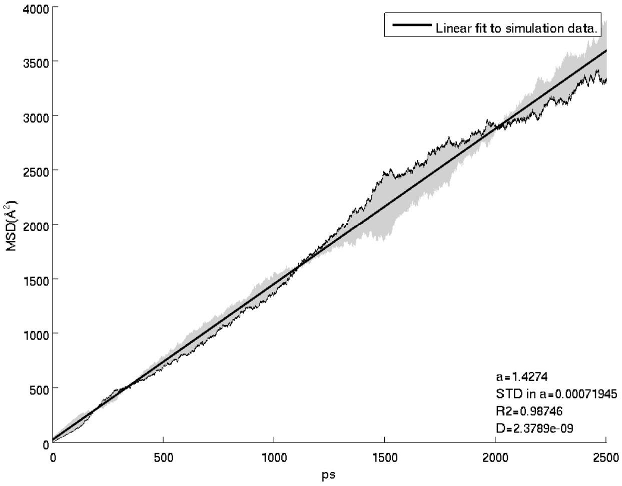

FIGURE C.10: MSD for 96 methane molecules.

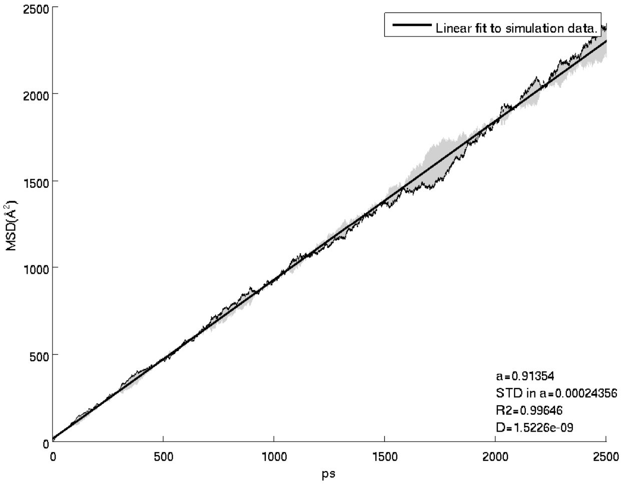

FIGURE C.11: MSD for 104 methane molecules.

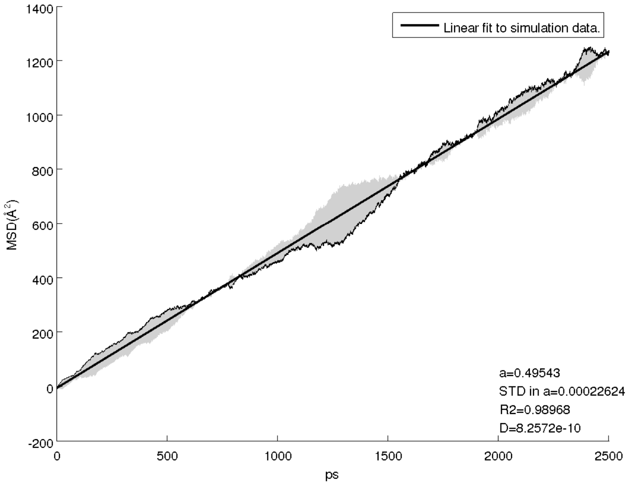

Figure C.12: MSD for 112 methane molecules.

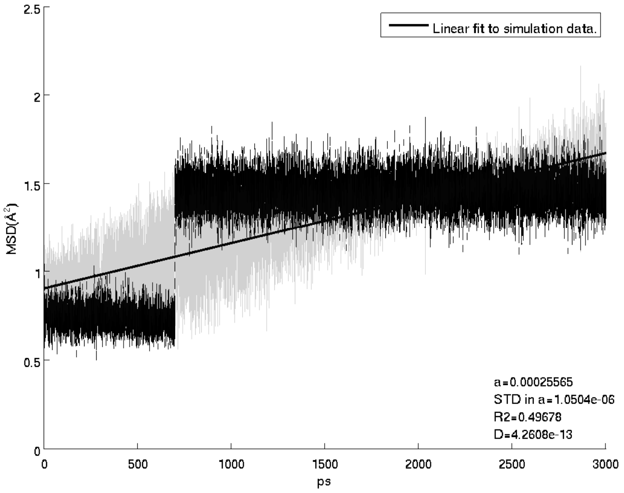

Figure C.13: MSD for 120 methane molecules.

Bibliography

[1] B. Jensen, B. Kvamme, T. Kuznetsova, K. O. Christensen, A.C.M Miguens, and E. Solbraa. Evaluation of zeolite lta force fields for molecular dynamics purposes. 2012. URL `http://thermosymposium.nist.gov/pdf/Abstract_1097.pdf`.

[2] B. Jensen, B. Kvamme, T. Kuznetsova, A.C.M Miguens, and E. Solbraa. Molecular dynamics investigation of triethylene glycol in hydrated lta zeolite. 2012. URL `http://www.sfgp.asso.fr/userfiles/Th%C3%A8ses19%20-%2015h10%20-%20044%20-%20JENSEN.pdf`.

[3] Eginhard Berger, Wolfgang Förg, Roy Scott Heiersted, and Pentti Paurola. The snøhvit project. *Linde Technology*, 1, 2003.

[4] Jórgen Bauck Jensen and Sigurd Skogestad. Optimal operation of a mixed fluid cascade lng plant. *Computer Aided Chemical Engineering*, 21:1569–1574, 2006.

[5] Alexandre Rojey. *Natural gas: production, processing, transport.* Editions Technip, 1997.

[6] JM Klinkenbijl, ML Dillon, and EC Heyman. Gas pre-treatment and their impact on liquefaction processes. In *PROCEEDINGS OF THE ANNUAL CONVENTION-GAS PROCESSORS ASSOCIATION*, pages 299–307. GAS PROCESSORS ASSOCIATION, 1999. URL `http://www.ipt.ntnu.no/~jsg/undervisning/naturgass/dokumenter/GasPreTreatment.pdf`.

[7] John A Dean et al. *Lange's Handbook of Chemistry . 1999.* McGraw-Hill.

[8] Shivaji Sircar and Alan L Myers. Gas separation by zeolites. *Handbook of Zeolite Science and Technology*, pages 1063–1105, 2003.

[9] Alan Dyer. An introduction to zeolite molecular sieves. 1988.

[10] P. Payra and P.K. Dutta. Zeolites: A primer. *Handbook of zeolite science and technology*, pages 1–19, 2003.

[11] IZA Structure Commission (IUPAC). Secondary building units, 2013. URL `http://izasc.ethz.ch/fmi/xsl/IZA-SC/SBUList.htm`.

[12] IZA Structure Commission(IUPAC). Composite building units and chains, 2013. URL `http://izasc.ethz.ch/fmi/xsl/IZA-SC/CBUList.htm`.

[13] Loewenstein W. The distribution of aluminum in the tetrahedra of silicates and aluminates. *American Mineralogist*, 39, 1954. URL `http://www.minsocam.org/ammin/AM39/AM39_92.pdf`.

[14] Joseph J. Pluth and Joseph V. Smith. Accurate redetermination of crystal structure of dehydrated zeolite a. absence of near zero coordination of sodium. refinement of silicon,aluminum-ordered superstructure. *Journal of the American Chemical Society*, 102(14):4704–4708, 1980. doi: 10.1021/ja00534a024. URL `http://pubs.acs.org/doi/abs/10.1021/ja00534a024`.

[15] Garcia-Sanchez, Almudena, Garcia-Perez, Elena, Dubbeldam, David, Krishna, Rajamani, Calero, and Sofia. A simulation study of alkanes in linde type a zeolites. *Adsorption Science and Technology*, 25(6):417–427, July 2007. ISSN 0263-6174. doi: 10.1260/026361707783908274. URL `http://dx.doi.org/10.1260/026361707783908274`.

[16] D. A. Faux, W. Smith, and T. R. Forester. Molecular dynamics studies of hydrated and dehydrated na+-zeolite-4a. *The Journal of Physical Chemistry B*, 101(10):1762–1768, 1997. doi: 10.1021/jp962998j. URL `http://pubs.acs.org/doi/abs/10.1021/jp962998j`.

[17] L.B. McCusker, F. Liebau, and G. Engelhardt. Nomenclature of structural and compositional characteristics of ordered microporous and mesoporous materials with inorganic hosts: (iupac recommendations 2001). *Microporous and Mesoporous Materials*, 58(1):3 – 13, 2003. ISSN 1387-1811. doi: 10.1016/S1387-1811(02)00545-0. URL `http://www.sciencedirect.com/science/article/pii/S1387181102005450`.

[18] Edith M Flanigen, Herman van Bekkum, and JC Jansen. *Introduction to Zeolite Science and Practice*, volume 58. Elsevier Science, 1991.

[19] Santi Kulprathipanja. *Zeolites in industrial separation and catalysis.* Wiley Online Library, 2010.

[20] Ramin Ekhteiari Salmas, Bar Demir, Erol Yldrm, Ahmet Sirkeciolu, Mine Yurtsever, and M. Gktu Ahunbay. Silversodium ion exchange dynamics in lta zeolite membranes. *The Journal of Physical Chemistry C*, 117(4):1663–1671, 2013. doi: 10.1021/jp311534e. URL `http://pubs.acs.org/doi/abs/10.1021/jp311534e`.

[21] Kiyoshi Ogawa, Masahiro Nitta, and Kazuo Aomura. A theoretical study of the site selectivity of the zeolite cation. 1. site selectivities of alkali and alkaline earth metal cations in zeolite a. *The Journal of Physical Chemistry*, 82(14):1655–1660, 1978. doi: 10.1021/j100503a017. URL `http://pubs.acs.org/doi/abs/10.1021/j100503a017`.

[22] A. Gualtieri, P. Norby, G. Artioli, and J. Hanson. Kinetics of formation of zeolite na-a [lta] from natural kaolinites. *Physics and Chemistry of Minerals*, 24(3):191–199, 1997. ISSN 0342-1791. doi: 10.1007/s002690050032. URL `http://dx.doi.org/10.1007/s002690050032`.

[23] Frank Jensen. *Introduction to Computational Chemistry.* Wiley, 2 edition, November 2006. ISBN 0470011874. URL `http://www.amazon.com/exec/obidos/redirect?tag=citeulike07-20&path=ASIN/0470011874`.

[24] Walter Greiner, Ludwig Neise, and Horst Stöcker. *Thermodynamics and Statistical Mechanics (Classical Theoretical Physics).* Springer, May 1995. ISBN 0387942998. URL `http://www.amazon.com/exec/obidos/redirect?tag=citeulike07-20&path=ASIN/0387942998`.

[25] Mark Tuckerman. *Statistical Mechanics: Theory and Molecular Simulation.* OUP Oxford, 2010.

[26] Anthony Michael Glazer and Justin S Wark. *Statistical mechanics: a survival guide.* Oxford University Press Oxford, 2001.

[27] Morten Helbæk, Signe Kjelstrup, and Morten Helb. *Fysikalsk kjemi.* Fagbokforl., 2006.

[28] Christopher J Cramer. *Essentials of computational chemistry: theories and models.* Wiley, 2005.

[29] Andrew R. Leach. *Molecular modelling : principles and applications.* Pearson Prentice Hall, 2 edition, April 2001. ISBN 0582382106. URL `http://www.amazon.com/exec/obidos/redirect?tag=citeulike07-20&path=ASIN/0582382106`.

[30] J. E. Jones. On the determination of molecular fields. II. from the equation of state of a gas. *Proceedings of the Royal Society of London. Series A*, 106(738):463–477, October 1924. doi: 10.1098/rspa.1924.0082. URL `http://dx.doi.org/10.1098/rspa.1924.0082`.

[31] Terrell L. Hill. Steric effects. i. van der waals potential energy curves. *The Journal of Chemical Physics*, 16(4):399–404, 1948. doi: 10.1063/1.1746902. URL `http://link.aip.org/link/?JCP/16/399/1`.

[32] R. A. Buckingham. The classical equation of state of gaseous helium, neon and argon. *Proceedings of the Royal Society of London. Series A, Mathematical and Physical Sciences*, 168(933):264–283, 1938. ISSN 00804630. doi: 10.2307/97239. URL `http://dx.doi.org/10.2307/97239`.

[33] J. R. Hart and A. K. Rappe. van der waals functional forms for molecular simulations. *The Journal of Chemical Physics*, 97(2):1109–1115, 1992. doi: 10.1063/1.463290. URL `http://link.aip.org/link/?JCP/97/1109/1`.

[34] Ali Khalaf Al-Matar and David A. Rockstraw. A generating equation for mixing rules and two new mixing rules for interatomic potential energy parameters. *Journal of Computational Chemistry*, 25(5):660–668, 2004. ISSN 1096-987X. doi: 10.1002/jcc.10418. URL `http://dx.doi.org/10.1002/jcc.10418`.

[35] Robert J. Good and Christopher J. Hope. New combining rule for intermolecular distances in intermolecular potential functions. *The Journal of Chemical Physics*, 53(2):540–543, 1970. doi: 10.1063/1.1674022. URL `http://link.aip.org/link/?JCP/53/540/1`.

[36] Mike P Allen and Dominic J Tildesley. *Computer simulation of liquids.* Oxford university press, 1989.

[37] John Anderson. *Computational Fluid Dynamics.* McGraw-Hill Science/Engineering/Math, 1 edition, February 1995. ISBN 0070016852. URL `http://www.amazon.com/exec/obidos/redirect?tag=citeulike07-20&path=ASIN/0070016852`.

[38] Glenn J. Martyna, Michael L. Klein, and Mark Tuckerman. Nos[e-acute]–Hoover chains: The canonical ensemble via continuous dynamics. *The Journal of Chemical Physics*, 97(4):2635–2643, 1992. doi: 10.1063/1.463940. URL `http://dx.doi.org/10.1063/1.463940`.

[39] Mark E. Tuckerman and Glenn J. Martyna. Understanding modern molecular dynamics: techniques and applications. *The Journal of Physical Chemistry B*, 104(2):159–178, 2000. doi: 10.1021/jp992433y. URL `http://pubs.acs.org/doi/abs/10.1021/jp992433y`.

[40] T. Kuznetsova and B. Kvamme. Ergodicity range of nos-hoover thermostat parameters and entropy-related properties of model water systems. *Molecular Simulation*, 21(4):205–225, 1999. doi: 10.1080/08927029908022062. URL `http://www.tandfonline.com/doi/abs/10.1080/08927029908022062`.

[41] Tatyana Kuznetsova and Bjørn Kvamme. Atomistic computer simulations for thermodynamic properties of carbon dioxide at low temperatures. *Energy Conversion and Management*, 43(18):2601 – 2623, 2002. ISSN 0196-8904. doi: 10.1016/S0196-8904(01)00195-9. URL `http://www.sciencedirect.com/science/article/pii/S0196890401001959`.

[42] Mihaly Mezei. Polynomial path for the calculation of liquid state free energies from computer simulations tested on liquid water. *J. Comput. Chem.*, 13(5):651–656, June 1992. ISSN 0192-8651. doi: 10.1002/jcc.540130515. URL `http://dx.doi.org/10.1002/jcc.540130515`.

[43] T. Kuznetsova and B. Kvamme. Viabilty of atomistic potentials for thermodynamic properties of carbon dioxide at low temperatures. *J Comput Chem*, 22(15):1772–1781, 2001.

[44] Alexander P Lyubartsev and Aatto Laaksonen. M. dynamix-a scalable portable parallel md simulation package for arbitrary molecular mixtures. *Computer physics communications*, 128(3):565–589, 2000.

[45] Benjamin G. Levine, John E. Stone, and Axel Kohlmeyer. Fast analysis of molecular dynamics trajectories with graphics processing unitsradial distribution function histogramming. *Journal of Computational Physics*, 230(9):3556 – 3569, 2011. ISSN 0021-9991. doi: 10.1016/j.jcp.2011.01.048. URL `http://www.sciencedirect.com/science/article/pii/S0021999111000829`.

[46] William Humphrey, Andrew Dalke, and Klaus Schulten. VMD – Visual Molecular Dynamics. *Journal of Molecular Graphics*, 14:33–38, 1996. URL `http://www.ks.uiuc.edu/Research/vmd/`.

[47] MATLAB. *version 7.10.0 (R2010a)*. The MathWorks Inc., Natick, Massachusetts, 2010.

[48] R. A. Jackson and C. R. A. Catlow. Computer simulation studies of zeolite structure. *Molecular Simulation*, 1(4):207–224, 1988. doi: 10.1080/08927028808080944. URL `http://www.tandfonline.com/doi/abs/10.1080/08927028808080944`.

[49] Laurence Leherte, Jean-Marie Andre, Eric G Derouane, and Daniel P Vercauteren. Study of the water behavior into a ferrierite zeolite by molecular dynamics simulations. *Computers & Chemistry*, 15(3):273–285, 1991.

[50] H. J. C. Berendsen, J. R. Grigera, and T. P. Straatsma. The missing term in effective pair potentials. *The Journal of Physical Chemistry*, 91(24):6269–6271, 1987. doi: 10.1021/j100308a038. URL `http://pubs.acs.org/doi/abs/10.1021/j100308a038`.

[51] William L. Jorgensen, Jeffry D. Madura, and Carol J. Swenson. Optimized intermolecular potential functions for liquid hydrocarbons. *J. Am. Chem. Soc.*, 106(22):6638–6646, October 1984. doi: 10.1021/ja00334a030. URL `http://dx.doi.org/10.1021/ja00334a030`.

[52] C. R. A. Catlow, C. M. Freeman, B. Vessal, S. M. Tomlinson, and M. Leslie. Molecular dynamics studies of hydrocarbon diffusion in zeolites. *Faraday Trans.*, 87(13):1947–1950, 1991. doi: 10.1039/ft9918701947. URL `http://dx.doi.org/10.1039/ft9918701947`.

[53] Garcia-Sanchez, Almudena, Garcia-Perez, Elena, Dubbeldam, David, Krishna, Rajamani, Calero, and Sofia. A simulation study of alkanes in linde type a zeolites. *Adsorption Science and Technology*, 25(6):417–427, July 2007. ISSN 0263-6174. doi: 10.1260/026361707783908274. URL `http://dx.doi.org/10.1260/026361707783908274`.

[54] Seiji Tsuzuki, Tadafumi Uchimaru, Kazutoshi Tanabe, and Satoru Kuwajima. Refinement of nonbonding interaction potential parameters for methane on the basis of the pair potential obtained by mp3/6-311g(3d,3p)-level ab initio

molecular orbital calculations: The anisotropy of h/h interaction. *The Journal of Physical Chemistry*, 98(7):1830–1833, 1994. doi: 10.1021/j100058a018. URL `http://pubs.acs.org/doi/abs/10.1021/j100058a018`.

[55] Niklas Hedin, Gregory J. DeMartin, Wieslaw J. Roth, Karl G. Strohmaier, and Sebastin C. Reyes. {PFG} {NMR} self-diffusion of small hydrocarbons in high silica ddr, {CHA} and {LTA} structures. *Microporous and Mesoporous Materials*, 109(13):327 – 334, 2008. ISSN 1387-1811. doi: 10.1016/j.micromeso.2007.05.007. URL `http://www.sciencedirect.com/science/article/pii/S1387181107002831`.

[56] Alexander P Lyubartsev and Aatto Laaksonen. Mdynamix source code. URL `http://www.fos.su.se/~sasha/md_prog.html/`.

[57] Notur - the norwegian metacenter for computational science. URL `http://www.notur.no/`.

[58] Database of Zeolite Structures IZA-SC. Lta zeolite, 2013. URL `http://izasc.ethz.ch/fmi/xsl/IZA-SC/mat_cif.xsl?-db=crystal_data&-lay=web&ID=LTA_1&-find`.

[59] Joseph J. Pluth and Joseph V. Smith. Accurate redetermination of crystal structure of dehydrated zeolite a. absence of near zero coordination of sodium. refinement of silicon,aluminum-ordered superstructure. *Journal of the American Chemical Society*, 102(14):4704–4708, 1980. doi: 10.1021/ja00534a024. URL `http://pubs.acs.org/doi/abs/10.1021/ja00534a024`.

[60] A. García-Sánchez, D. Dubbeldam, and S. Calero. Modeling adsorption and Self-Diffusion of methane in LTA zeolites: The influence of framework flexibility. *J. Phys. Chem. C*, 114(35):15068–15074, August 2010. doi: 10.1021/jp1059215. URL `http://dx.doi.org/10.1021/jp1059215`.

[61] NAMD tutorial page. Water sphere tcl script. URL `http://www.ks.uiuc.edu/Training/Tutorials/namd/namd-tutorial-unix-html-old/node26.html`.

[62] Toni Giorgino. Computing 1-d atomic densities in macromolecular simulations: the density profile tool for vmd. URL `http://multiscalelab.org/utilities/DensityProfileTool`.

[63] Brian G. Moore and Afraa A. Al-Quraishi. The structure of liquid clusters of lennard-jones atoms. *Chemical Physics*, 252(3):337 – 347, 2000. ISSN 0301-0104. doi: 10.1016/S0301-0104(99)00334-1. URL `http://www.sciencedirect.com/science/article/pii/S0301010499003341`.

[64] D. Dubbeldam, S. Calero, T. J. H. Vlugt, R. Krishna, T. L. M. Maesen, and B. Smit. United atom force field for alkanes in nanoporous materials. *The Journal of Physical Chemistry B*, 108(33):12301–12313, 2004. doi: 10.1021/jp0376727. URL `http://pubs.acs.org/doi/abs/10.1021/jp0376727`.

[65] Garcia-Sanchez, Almudena, Garcia-Perez, Elena, Dubbeldam, David, Krishna, Rajamani, Calero, and Sofia. A simulation study of alkanes in linde type a zeolites. *Adsorption Science and Technology*, 25(6):417–427, July 2007. ISSN 0263-6174. doi: 10.1260/026361707783908274. URL `http://dx.doi.org/10.1260/026361707783908274`.

[66] A.V. Kiselev, A.A. Lopatkin, and A.A. Shulga. Molecular statistical calculation of gas adsorption by silicalite. *Zeolites*, 5(4):261 – 267, 1985. ISSN 0144-2449. doi: 10.1016/0144-2449(85)90098-3. URL `http://www.sciencedirect.com/science/article/pii/0144244985900983`.

[67] E Beerdsen, D Dubbeldam, and B Smit. Loading dependence of the diffusion coefficient of methane in nanoporous materials. *The Journal of Physical Chemistry B*, 110(45):22754–22772, 2006.

[68] Marcello Sega, Renzo Vallauri, and Simone Melchionna. Diffusion of water in confined geometry: The case of a multilamellar bilayer. *Phys. Rev. E*, 72: 041201, Oct 2005. doi: 10.1103/PhysRevE.72.041201. URL `http://link.aps.org/doi/10.1103/PhysRevE.72.041201`.

[69] Pierfranco Demontis and Giuseppe Baldovino Suffritti. A molecular dynamics study of diffusion of methane in partially dealuminated zeolite na a. *Molecular Physics*, 91(4):669–680, 1997.

[70] D Dubbeldam, E Beerdsen, TJH Vlugt, and B Smit. Molecular simulation of loading-dependent diffusion in nanoporous materials using extended dynamically corrected transition state theory. *The Journal of chemical physics*, 122: 224712, 2005.

[71] AV Anil Kumar, S Yashonath, Marcel Sluiter, and Yoshiyuki Kawazoe. Rotational motion of methane within the confines of zeolite naca a: Molecular dynamics and ab initio calculations. *Physical Review E*, 65(1):011203, 2001.

[72] P. Demontis and G. B. Suffritti. Sorbate-loading dependence of diffusion mechanism in a cubic symmetry zeolite of type zk4. a molecular dynamics study. *The Journal of Physical Chemistry B*, 101(30):5789–5793, 1997. doi: 10.1021/jp970358q. URL `http://pubs.acs.org/doi/abs/10.1021/jp970358q`.

[73] Anthony Loriso, Mary J. Bojan, Alexei Vernov, and W. A. Steele. Computer simulation studies of ordered structures formed by rare gases sorbed in zeolite rho. *The Journal of Physical Chemistry*, 97(29):7665–7671, 1993. doi: 10.1021/j100131a041. URL `http://pubs.acs.org/doi/abs/10.1021/j100131a041`.

[74] Kwang Hun Lim and Clare P. Grey. Characterization of extra-framework cation positions in zeolites nax and nay with very fast 23na mas and multiple quantum mas nmr spectroscopy. *Journal of the American Chemical Society*, 122(40):9768–9780, 2000. doi: 10.1021/ja001281d. URL `http://pubs.acs.org/doi/abs/10.1021/ja001281d`.

[75] Schoonheydt, R. A. Cationic motion in dehydrated zeolites. *J. Phys. Colloques*, 41:C6–261–C6–264, 1980. doi: 10.1051/jphyscol:1980666. URL `http://dx.doi.org/10.1051/jphyscol:1980666`.

[76] Wojciech Gren, Stephen C. Parker, Ben Slater, and Dewi W. Lewis. Structure of zeolite a (lta) surfaces and the zeolite a/water interface. *The Journal of Physical Chemistry C*, 114(21):9739–9747, 2010. doi: 10.1021/jp909355e. URL `http://pubs.acs.org/doi/abs/10.1021/jp909355e`.

[77] Joseph J. Pluth and Joseph V. Smith. Crystal structure of dehydrated potassium-exchanged zeolite a. absence of supposed zero-coordinated potassium. refinement of silicon, aluminum-ordered superstructure. *The Journal of Physical Chemistry*, 83(6):741–749, 1979. doi: 10.1021/j100469a021. URL `http://pubs.acs.org/doi/abs/10.1021/j100469a021`.

[78] Aldo F. Combariza and German Sastre. Influence of zeolite surface in the sorption of methane from molecular dynamics. *The Journal of Physical*

Chemistry C, 115(28):13751–13758, 2011. doi: 10.1021/jp202043t. URL `http://pubs.acs.org/doi/abs/10.1021/jp202043t`.

[79] Pierfranco Demontis and Giuseppe B. Suffritti. A comment on the flexibility of framework in molecular dynamics simulations of zeolites. *Microporous and Mesoporous Materials*, 125(12):160 – 168, 2009. ISSN 1387-1811. doi: 10.1016/j.micromeso.2009.03.032. URL `http://www.sciencedirect.com/science/article/pii/S1387181109001693`.

[80] IT Todorov, W Smith, and UK Cheshire. The dl poly 4 user manual. *STFC, STFC Daresbury Laboratory, Daresbury, Warrington, Cheshire, WA4 4AD, United Kingdom, version*, 4(0), 2011. URL `http://www.stfc.ac.uk/CSE/CSE/randd/25526.aspx`.